ASSESSMENT OF ULTRASOUND ELASTOGRAPHY FOR ORTHOPEDIC APPLICATIONS

A Dissertation

by

BIREN JAGDISH PARMAR

Submitted to the Office of Graduate and Professional Studies of
Texas A&M University
in partial fulfillment of the requirements for the degree of

DOCTOR OF PHILOSOPHY

Chair of Committee,	Raffaella Righetti
Committee Members,	Steven M. Wright
	Jun Zou
	Harry Hogan
Head of Department,	Miroslav M. Begovic

August 2015

Major Subject: Electrical Engineering

ABSTRACT

Ultrasound imaging is emerging as an attractive alternative modality to standard x-ray and CT methods for bone assessment applications. The high reflectivity at the bone/soft tissue interface that occurs due to high acoustic impedance mismatch presents an important diagnostic opportunity affording the detection of abnormalities at bone surfaces with high accuracy and contrast-to-noise ratios. Furthermore, the mechanical properties of the soft tissue surrounding the bones undergo changes depending on the integrity of the underlying bone, viz. intact, fractured or healing. Unlike other imaging modalities, ultrasound elastography techniques, with their sensitivity to variations in soft tissue stiffness, are able to assist with monitoring bone regrowth. However, there is presently a lack of systematic studies that investigate the performance of diagnostic ultrasound techniques in bone imaging applications. This dissertation aims at understanding the performance limitations of new ultrasound techniques for assessing intact and fractured bones *in vitro* as well as *in vivo*.

Ultrasound based 2D, 3D and elastography imaging experiments were performed on *in vitro* and *in vivo* samples of mammalian as well as non-mammalian bones. Ultrasound measurements of controlled defects were statistically compared with those obtained from the same samples using alternate imaging modalities. The performance of axial strain elastograms and axial shear strain elastograms at the soft tissue/bone interface was also studied in intact and fractured bones, and statistical analysis was carried out using elastographic image quality tools. The results of this study demonstrate

that it is feasible to use diagnostic ultrasound imaging techniques to assess bone defects in real time and with high accuracy and precision. The relative strength of the axial strains and the axial shear strains at the bone/soft tissue interface with respect to the background soft tissue reduce in the presence of a fracture. Consequently, the study concluded that a combination of these imaging modalities might provide information regarding the integrity of the underlying bone and also an insight into the severity of the fractures, alignment of bone fragments and the progress of bone healing. In the future, ultrasound imaging techniques might provide a cost-effective, real-time, safe and portable diagnostic tool for bone imaging applications.

DEDICATION

To my parents, who supported me unconditionally through the years as I worked on completing this dissertation.

To Manisha, my wife, who joined me some way along the journey and unflinchingly decided to be a part of the joyride through all the ups and downs.

To Hersh, my kid brother, who stepped into my shoes and made up for my absence while I worked on this dissertation.

To Nithin, Vivek, Ram, Reetu and Biruda, my friends, who have helped me along the way in more ways than they can imagine.

ACKNOWLEDGEMENTS

I would like to thank my committee chair, Dr. Righetti for her unwavering support and guidance throughout the execution of this research. Thanks are also due to my committee members, Dr. Wright, Dr. Zou and Dr. Hogan, for their valuable inputs and feedback on the progress of this work. Special thanks are due to Dr. Goenezen for stepping in during a critical time to help see this work through completion.

A number of collaborators contributed during various stages of this research, and it would be unfair to not acknowledge them. I'm grateful to Dr. Krouskop, Ennio and Dr. Weiner for sharing their expertise and insight at various stages during this research. Thanks to Dr. Han and his student, Whitney, Dr. Sabonghy, Dr. Ferrari and Dr. Fossum for providing access to resources that enabled me to carry forward the experimental aspects of this research. I would also like to thank Dr. Jay Humphrey and the TAMU CMP tissue sharing program for providing tissue samples that were used for experiments in this research. Numerous entities on the Texas A&M University campus helped with various aspects of pursuing this research, and I'd like to acknowledge them: Department of Electrical and Computer Engineering, Office of Graduate and Professional Studies, International Student Services and University Writing Center. The tireless efforts by members of the staff at these offices go a long way in supporting students and helped me focus in my research endeavors.

Thanks also go to my friends and colleagues at the Ultrasound Imaging group: Raghu, Sthiti, Anuj, Sanjay, Xu, Mohan, Srinath and Shafeeq. Formal and informal

discussions with these smart students contributed in drastically improving the quality of research.

I am also grateful to the numerous members of faculty and staff at Texas A&M University for giving me the perfect Aggie experience. Dr. Ji and Dr. Pfister gave me valuable advice that I was able to use at various stages while pursuing my research. Organizations like the India Association, Indian Graduate Students Association and the Graduate and Professional Student Council, among many others, went a long way in enhancing my ability to perform as a human being, beyond academics. Tammy and Katy, along with their supporting staff, do wonderful behind-the-scenes jobs at making it convenient to achieve the various milestones of such long-term work as this dissertation. I have learned a lot from everyone along the way, and will remain indebted to them forever.

TABLE OF CONTENTS

Page

LIST OF FIGURES

Page

LIST OF TABLES

Page

1. INTRODUCTION

Background

The study of bones and bone defects is an active area of research. In particular, long bones occupy a significant proportion of cases studied in a clinical scenario as well as in a laboratory environment. This is evidenced by the fact that statistically, the most commonly fractured bones as reported for children are the distal radius, humerus, forearm shaft and tibial shaft (not necessarily in this order) - all long bones (Cheng and Shen 1993). Furthermore, long bone injuries constitute a significant proportion of non-fatal injuries reported on a global scale (Mock and Cherian 2008).

Currently, clinical diagnosis of bone fractures or defects is generally achieved through the use of imaging modalities and surface characterization techniques (Greenfield 1990, DeLee et al 2003). Bone imaging methods are used for the localization of the bone fracture or defect, the assessment of diagnostically relevant fracture details and the monitoring of bone healing or regrowth. In addition to bone fracture assessment, bone imaging methods are also used to detect bone tumors and assess treatment outcomes or evaluate soft tissue/bone trauma (Abdel-Dayem 1997). Traditionally, this information is obtained using x-rays and in some cases computed tomography (CT) as well as magnetic resonance imaging (MRI) imaging modalities, which allow detection of skeletal pathologies and associated responses with superior sensitivity and specificity (Feldkamp et al 1989, Genant et al 2008, Lang et al 1998). The weaknesses of these modalities, however, rest primarily in their reliance upon radiation for image generation

(x-ray and CT), limited portability, lack of real-time feedback and high costs. These weaknesses are important limiting factors in a number of applications, which may include assessment of bone defects in children, intra-operative image guidance and assessment of bone fractures in the field.

Standard ultrasound imaging for orthopedics

In the recent past, ultrasound imaging of long bones and their fractures in a clinical scenario has been generating a lot of interest (Anonymous2012, Chaar-Alvarez et al 2011, Barata et al 2011) by virtue of its ability to assist with rapid diagnosis in a portable, interactive, real time, safe and repeatable fashion. The majority of the work retrievable in the literature for ultrasonic bone assessment relates to the use of quantitative ultrasound (QUS). QUS methods typically use low frequency techniques to estimate ultrasound parameters that are related to the bone density and composition in order to detect bone abnormalities or predict fracture risks (Cheng et al 1997, Marín et al 2006, Muller et al 2005, Njeh et al 1997, Laugier 2004, Roux et al 1996, Laugier et al 1997, Longo et al 2010, Hakulinen et al 2005). More recently, a number of studies have been reported that concentrate on the use of diagnostic ultrasound techniques to image human bone fractures (Arni et al 2009, Wang et al 1999, Lewis and Logan 2006). In several of these cases, ultrasound images helped in the visualization of fractures that the radiographs missed (Cho et al 2004). In patients undergoing the Ilizarov procedure for limb lengthening, ultrasound imaging proved a more sensitive tool than x-rays to assess bone growth (Young et al 1990). These studies are based on harnessing the presence of a large mismatch of acoustic impedance between bone and the surrounding soft tissue

(Christensen 1998, Nyland and Mattoon 2002) as a contrasting mechanism. Based on this property, a significant portion of the incident ultrasound energy impinging at a soft tissue–bone interface is reflected back to the receiver, leading to a high reflection coefficient and backscattering signal at the location of the interface. This ultrasonic behavior of bones is a consequence of their chemical and structural compositions, namely bone cells embedded in a web of inorganic salts, and this is characteristic of endoskeletal bones in general, irrespective of the species of vertebrates (Hickman et al 2005). While on the one hand the high reflectivity at the soft tissue–bone interface may limit assessment of internal bone properties (as opposed to QUS), on the other hand it presents an important diagnostic opportunity affording the detection of abnormalities at bone surfaces with high accuracy and contrast-to-noise ratios.

A study on the applicability of standard 2D and 3D ultrasound imaging to assess different types of bone defects forms sections 2 and 3 of this dissertation. The main questions being addressed in these sections are:

1. Is it feasible to assess controlled bone defects using standard 2D and 3D ultrasound imaging techniques?
2. How do the ultrasound measurements compare to those from other standard imaging modalities?
3. How do the 3D imaging techniques perform when used to image intact as well as fractured long bones with the surrounding soft tissue left intact?

Ultrasound elastography imaging for orthopedics

Another technique based on the ultrasound imaging modality is elastography, whereby images that aid the assessment of tissue abnormalities based on the presence of an underlying mechanical contrast between normal and abnormal tissues are generated. This technique involves applying an external quasi-static strain (2-5%) over the region of interest (ROI) and acquiring raw RF frames before and after the compression has been applied. Cross-correlation based algorithms are applied to compute tissue motion from the acquired frames, which is then presented in the form of elastograms that display the distribution of strains in the ROI. One such elastogram, called the axial strain elastogram, is computed as the gradient of axial displacements in the axial direction. This type of elastogram images the distribution of the local axial strains in the tissue as a result of the external compression and could provide functional information about the ROI. For instance, visualizing the extent of liver fibrosis on the basis of degree of elastic stiffness of the liver may help monitoring the progress of chronic viral hepatitis as well as its treatment (Feldcamp et al 1989, Genant et al 2008). Malignancy of breast lesions and lymph nodes may be diagnosed based on the stiffness contrast between the lesions/lymph nodes and the background tissue (Konofagou et al 2000, Thitaikumar et al 2007a, Thitaikumar et al 2007b, Chakraborty et al 2012, Newton and Nunamaker 1985). Elastography may also help in visualizing the inflammation in tendons and diseased muscles (Drakonaki et al 2012, Konofagou et al 2002). The advantages of using elastography in these scenarios include obviating the need to perform invasive biopsies to assess disease progression, eliminating potential inter-operator and inter-sample

variability during biopsy analysis (Friedrich-Rust et al 2007), real time access to new tissue information (Drakonaki et al 2012) and, generation of diagnostic images with high SNR and contrast-to-noise ratio as well as high spatial and temporal resolutions (Konofagou et al 2002), among others.

Recent developments in the field of elastography have focused on the possibility of assessing the degree of connectedness between various tissues using axial shear strain elastography (ASSE) (Konofagou and Ophir 1998, Konofagou et al 2000, Thitaikumar et al 2007a). These studies suggest that axial component of the shear strain (computed as the gradient of the axial displacement in the lateral direction) at the boundary between tissues with different mechanical properties may be indicative of the tissue mobility. For instance, a breast lesion that is loosely bonded to the surrounding soft tissue is likely benign in nature, and may be identified as a localized region (i.e., covering a smaller area) of high intensity at the lesion boundary on the corresponding axial shear strain elastogram (Thitaikumar et al 2007a). Conversely, fuller bonding between the lesion and the surrounding soft tissue may be associated with lesion malignancy, and could manifest as an axial shear strain signal distributed over a relatively larger area on the elastogram, as compared to that in the benign cases. It has been shown that the conditions under which axial strain elastograms generated are optimal (with respect to CNR_e and SNR_e) are also well suited for obtaining axial shear strain elastograms of the lesion boundary with high resolution, SNR_{asse} and CNR_{asse} (Thitaikumar et al 2007b). Variations of this technique have been applied to classify benign and malignant lesions

in the breast, and have potential application in the diagnosis of brain tumors as well (Chakraborty et al 2012).

The above characteristics make ultrasound elastography techniques potentially well suited for bone imaging applications because aside from the variation in the acoustic properties (speed of sound, density, acoustic impedance and ultrasonic attenuation), bone tissue is also characterized by significantly different mechanical properties with respect to the surrounding soft tissue. Specifically, the elastic modulus of bones is known to be up to 5-6 orders of magnitude higher than that of the surrounding soft tissue (Spatz et al 1996). As a result, when a compressive strain is applied to a region comprising soft tissue and bone, the soft tissue undergoes much higher strains than the bone. Also, depending on the degree and orientation of the applied compressive force with respect to the bone surface and the physiology of the underlying musculoskeletal anatomy, some sliding motion at the bone-soft tissue interface may also be observed. The fact that the periosteum is only weakly connected to the bone shaft, and may undergo sliding over the bone surface under appropriate conditions would tend to support this hypothesis (Wilson-MacDonald 2002). There is also experimental evidence to suggest that high shear strains are generated in the muscle adjacent to the bone when the body is exposed to localized direct compressive stress (Oomens et al 2003). Furthermore, when long bones undergo a fracture, the periosteum could experience tearing and there is callus formation due to the inflammation that results by accumulation of dead tissue at the fracture site (Newton and Nunamaker 1985). The process of regrowth of the bone at the fracture location is characterized by a continuous

hardening of the callus formed at the fracture site, until the bone is fully regrown and it re-attains the mechanical properties as they were before the fracture.

In summary, the soft tissues in proximity to the bone undergo changes in mechanical properties in a manner that is correlated with the changes in the structural stability of the bone. These changes may also be indicative of the severity of a fracture and may be used to monitor tissue healing. A suitable imaging modality that may be able to image these changes in the mechanical contrast between bone and soft tissue might be able to provide diagnostically and prognostically relevant information regarding the pathological or physiological state of a bone. As B-mode and 3D ultrasound modalities are not sensitive to mechanical contrasts, elastography-based techniques may provide a fast, safe and accurate tool to obtain complimentary information about the interaction between bone and the soft tissue in both intact as well as fractured bones. The axial strain elastograms and axial shear strain elastograms might be able to provide information regarding the presence of fractures, and also provide an insight into the severity of the fracture as well as help monitor the progress of the subsequent healing process. In the future, it may also be possible to combine structural information as obtained from the B-mode and 3D ultrasound modalities with information regarding mechanical properties using elastography, hence creating a new multi-modal imaging modality.

Consequently, sections 4 and 5 of this dissertation are dedicated to assessing ultrasound elastography techniques for their ability to assess intact and fractured tibias using canine and ovine samples. The broad topics of these sections are:

1. How do ultrasound elastography techniques perform in providing functional information regarding intact, fractured and healing bones?
2. Is it feasible to use ultrasound elastography techniques to image intact and fractured bones *in vitro* as well as *in vivo*?

Applications

Aside from monitoring of healing of bones, numerous other applications of ultrasound imaging for assessing bones can be envisioned. One of these is in the area of regenerative medicine applied to musculoskeletal disorders. A number of these studies have focused on the generation of biomaterials for bone tissue engineering. Imaging and monitoring materials engineered for tissue regeneration must be accomplished without compromising the biological processes that occur inside the scaffolds. Exposure to radiation should be kept at a minimum during bone regeneration. Radiation damages newly formed blood vessels and this is accompanied by death of differentiating bone cells leading to osteonecrosis and porosis. The use of safe and non-invasive ultrasound imaging techniques in orthopedic regenerative medicine applications could be of great clinical significance.

The safety and portability of the ultrasound imaging modality allows for the use of elastography techniques with rapid diagnoses and applicability of appropriate corrective measures right on the field, hence revolutionizing military and sports medicine. Pediatric orthopedics also stands to benefit substantially from the use of radiation-free imaging modalities to assist with clinical care of young children. The

ability to perform repeated examinations with relatively low risks makes it highly suitable for monitoring bone defects over an extended period of time.

Another area of importance is the 3D ultrasound reconstruction of bones under study. The 3D rendering process typically involves acquiring a number of parallel B-mode frames using an ultrasound transducer and then reconstructing the frames using various algorithms. Segmentation of the bone from each of these frames prior to the 3D reconstruction would enhance the quality of structural information derived from the renderings. One way of accomplishing this would be to apply elastography to differentiate bone from the soft tissue, and use this information to eliminate the unwanted tissue features on the B-modes. The segmented frames can then be used to perform the 3D renderings. In all these applications, the high sensitivity of ultrasound elastography to variations in mechanical properties of the soft tissue makes it better suited to bone imaging than other imaging modalities such as x-rays. The axial shear strain elastograms, in particular, may provide information regarding connectivity at the bone-soft tissue interface – information that no other modality, including x-rays, CT and MRI are capable of showing directly. Thus, ultrasound elastography may provide a significant contribution to field of orthopedics.

In the final section, some preliminary results of elastography techniques applied to monitor bone healing and human tissue samples *in vivo* are presented. Along with these results, some suggestions are made with regards to the possible directions for future studies.

2. CHARACTERIZATION OF CONTROLLED BONE DEFECTS USING 2D AND 3D ULTRASOUND IMAGING TECHNIQUES[*]

Introduction

Clinical diagnosis of bone fractures or defects is generally achieved through the use of imaging modalities and surface characterization techniques (Greenfield 2008, DeLee and Miller 2002). Bone imaging methods are used for the localization of the bone fracture or defect, the assessment of diagnostically relevant fracture details and the monitoring of bone healing or regrowth. In addition to bone fracture assessment, bone imaging methods are also used to detect bone tumors and assess treatment outcomes or evaluate soft tissue/bone trauma (Abdel-Dayem 1997). Traditionally, this information is obtained using x-ray and computed tomography (CT) imaging modalities, which allow detection of skeletal pathologies and associated responses with superior sensitivity and specificity (Feldkamp et al 1989, Genant et al 2008, Lang et al 1998). The weaknesses of these modalities, however, rest primarily in their reliance upon radiation for image generation, limited portability, lack of real-time feedback and high costs. These weaknesses are important limiting factors in a number of applications, which may include assessment of bone defects in children, intra-operative image guidance and assessment of bone fractures in the field.

---

[*] Reprinted with permission from Parmar B J, Longsine W, Sabonghy E P, Han A, Tasciotti E, Weiner B K, Ferrari M and Righetti R 2010 Characterization of controlled bone defects using 2D and 3D ultrasound imaging techniques Phys. Med. Biol. 55(16) 4839-60 Copyright [2010] by IOP Publishing

In recent years, ultrasound has emerged as a promising alternative modality to x-ray and CT methods for assessing bone growth and defects such as fractures and thinning due to osteoporosis (Blake et al 1997, Han and Kim 2005, Hans and Krieg 2008, Rathfelder and Paar 1995). The majority of the work retrievable in the literature for ultrasonic bone assessment relates to the use of quantitative ultrasound (QUS). QUS methods typically use low frequency techniques to estimate ultrasound parameters that are related to the bone density and composition in order to detect bone abnormalities or predict fracture risks (Cheng et al 1997, Hakulinen et al 2005, Marin et al 2006,Muller et al 2005, Njeh et al 1997, Laugier et al 1997, Roux et al 1996, Laugier 2004, Longo et al 2010). More recently, a number of studies have been reported that concentrate on the use of diagnostic ultrasound techniques to image human bone fractures (Arni et al 2009, Enns et al 2004, Lewis and Logan 2006, Wang et al 1999). In several of these cases, ultrasound images helped in the visualization of fractures that the radiographs missed (Cho et al 2004). In patients undergoing the Ilizarov procedure for limb lengthening, ultrasound imaging proved a more sensitive tool than x-rays to assess bone growth (Young et al 1990). Furthermore, ultrasound imaging techniques have also been employed to assess trauma in the soft tissue surrounding the bone fracture (Cho et al 2004).

The physical principle that makes ultrasound techniques at the diagnostic frequencies clinically useful in bone imaging applications is the presence of a large mismatch of acoustic impedance between bone and the surrounding soft tissue (Christensen 1998, Nyland and Mattoon 2002). Thus, a significant portion of the

incident ultrasound energy impinging at a soft tissue–bone interface is reflected back to the receiver, leading to a high reflection coefficient and backscattering signal at the location of the interface. This ultrasonic behavior of bones is a consequence of their chemical and structural compositions, namely bone cells embedded in a web of inorganic salts, and it is characteristic of endoskeletal bones in general, irrespective of the species of vertebrates (Hickman et al 2005). While on the one hand the high reflectivity at the soft tissue–bone interface may limit assessment of internal bone properties (as opposed to QUS), on the other hand it presents an important diagnostic opportunity affording the detection of abnormalities at bone surfaces with high accuracy and contrast-to-noise ratios.

Several factors have brought clinicians and researchers to investigate the possibility of using diagnostic ultrasound imaging modalities as a new and promising means for bone assessment. First, ultrasound imaging techniques are non-invasive and do not require the use of radiation or contrast agents. Thus, ultrasound imaging techniques may be a much desired diagnostic tool for the visualization of bones in the proximities of tissues that should not be exposed to radiation. Thesemay include maxillofacial applications (Hughes et al 2003,Mukai-Higashihori et al 2008), bone assessment in children or imaging of bioactive scaffolds for bone regeneration (Rus and Garcia-Martinez 2007). Second, ultrasound imaging techniques can provide clinical feedback in real time, making them suitable for intra-operative use and for assessment of bone fractures in the ER (Chan 2009, Durston and Swartzentruber 2000). Third, ultrasound imaging techniques are cost-effective imaging modalities (particularly when

compared to CT and MRI methods) and can be used for frequent follow-ups. Finally, ultrasound imaging techniques can be implemented in small, portable devices that can be used for bone assessment 'in the field' where other techniques cannot be readily available, such as space-related, sports and military medicine applications (Diaz et al 2008, Kaufman et al 2007, Kirkpatrick et al 2003, McNeil et al 2009). Additionally, in recent years, the deployment of new technologies, efficient transducer materials, and advanced signal and image processing techniques have lead to diagnostic systems capable of producing ultrasound images of significantly improved image quality, high resolution 3D and 4D visualization of tissue structures (Turan et al 2009, Wang 2008) and accurate estimation of new tissue properties related to the tissue mechanical behavior (Insana et al 2004, Liu and Ebbini 2008, Righetti et al 2005, Zhai et al 2008).

While a limited number of studies suggests the feasibility of using standard ultrasound imaging techniques to detect bone defects (Cho et al 2004, Kramer et al 1997, H¨ubner et al 2000, Hacihaliloglu et al 2008, Ross et al 2009, Parmar et al 2009), there is a lack of systematic studies that investigate the performance limitations of these techniques in assessing controlled bone defects. We report a controlled study that aims at understanding the performance limitations of diagnostic ultrasound techniques in imaging a wide range of controlled bone defects both in mammalian and non-mammalian bones *in vitro*. The ultrasound imaging findings are then benchmarked against co-registered findings obtained from standard x-ray imaging and optical microscopy modalities.

Methods

Ultrasound experiments were conducted on 20 chicken bone samples and 18 rabbit bone samples *in vitro*, specifically femora and tibiae. Preliminary experiments were performed on intact bones (ten samples) and bones with fractures (ten samples) to assess the characteristic appearance of the chicken and rabbit bones in the ultrasound images. Experiments were then performed on bones with controlled circular defects (18 samples) with size ranging from 400 μm to 5 mm. Ultrasound findings were benchmarked against findings obtained from the same samples using standard x-ray imaging and optical microscopy modalities.

Intact bones

The experiments on intact bones were performed on samples with the soft tissue left intact. These experiments were performed to assess the general appearance of mammalian and non-mammalian intact bones in the ultrasound images and to qualitatively compare these images to those obtained from the bone samples with defects.

Bones with fractures

For the experiments conducted on fractures, a complete fracture was induced in the animal samples with the soft tissue left intact. To produce the fracture, the animal samples were suspended on a cantilever-like arrangement and pressure was applied at the free end, in a direction normal to the bone axis to produce the fracture. These experiments were used merely to assess the ultrasonic appearance of the fractured bones versus the intact bones and the bones with the controlled defects, and were not compared

statistically to x-rays or optical imaging findings due to the difficulty in reproducing the same fractures in a controlled manner.

Bones with controlled laser-induced defects

Generation of the controlled defects

The majority of the experiments were performed on bone samples with controlled defects. For these experiments, the bones were first removed from the animal samples. Then, the bones were subjected to a vector mode cutting by a CO_2 laser engraving and cutting system (PLS6.120D, Universal Laser Systems Inc., AZ, USA) to produce lateral through-holes within the bones. The use of this laser system allowed us to systematically induce bone defects of known size, shape and location inside the bones. The software interface allowed precise control of the parameters used to induce the defects such as output power and speed. Thiswas accomplished by first creating a drawing of the outline of the circular defect (with a given nominal diameter) using CAD software (SolidWorks, Dassault Systèmes SolidWorks Corp., MA, USA). The drawing was then printed to the interfacing software, which converted the CAD dimensions into actual dimensions readable by the laser system. The final bone cutting process involved positioning the bone beneath the laser, focusing the laser beam at the upper/lower walls of the bones, and then executing a run command. A high-pressure nitrogen assist was used in order to protect the laser lens from debris created by the burning on the bone surface. In general, the generation of a single circular defect in each wall required between 2–4 runs of the laser system depending on the wall thickness of the specimen sample and the location of the defects within the sample. The number of runs was

restricted to 2–4 by operating the laser mostly at 100% power (60 W). Usage of lower power levels would increase the number of runs necessary to create each of the holes required for the study, thus resulting in inconsistent refocusing of the laser before each run. Circular defects of diameters ranging from 400 μm to 5 mm were induced in the samples.

Optical microscopy evaluation

The exact sizes of the laser-induced defects obtained with the cutting process were evaluated using an optical microscope system (Nikon Eclipse LV100 microscope) equipped with a Digital Sight DS-2Mv CCD camera (Nikon Instruments Inc., USA) under 50× and 100× magnification. The bone samples with the induced defects were placed on the adjustable stage below the lens and focused upon with the aid of illumination from the top. It should be noted that focusing at the circular defects was feasible only to the extent allowed by the curvature of the bones. Optical images were captured, and the diameters of the boundaries of the defects were measured using appropriate image acquisition and analysis software (NIS-Elements BR 3.0). Results obtained from the optical microscopy images were considered the gold standard for the evaluation of the defect sizes.

X-ray imaging evaluation

In order to compare the results obtained using ultrasound methods to those obtained using standard imaging methods commonly used for bone assessment, bone samples with laser-induced defects were also evaluated using standard x-ray imaging techniques. For the x-ray imaging experiments, the bone samples were directly

positioned on the x-ray cassette, and the x-ray images were acquired using a diagnostic x-ray imaging system (Quantum Medical Imaging Quest HF Series X-ray Generator) set at 53 kV, 150 SMA, 3.0MAS, CM6 at 40 inches. The x-ray images were then scanned using the Kodak Directview CR 825 System and analyzed using theViztekViewer Application. Measurements on the x-ray images were performed using annotations in the Viztek Viewer Software.

Ultrasound imaging evaluation

For the ultrasound imaging experiments, the chicken and rabbit bone samples with induced controlled defects were first scanned under degassed water. This allowed acquisition of the 2D data to be used for the statistical analysis as explained in the next section. Thereafter, the same experiments were repeated with the samples embedded into gelatin cases, which were used as a support to perform controlled 3D scans. The gelatin cases were fabricated by mixing 5% by weight of gelatin and 3% by weight of agar into boiling water and following the procedure described in Kallel et al (2001). Although similar gelatin phantoms have often been used as ultrasonic tissue-mimic phantoms (Madsen et al 2005), their use in this study was purely to support the bone sample during the 3D ultrasound experiments.

All samples were scanned using a Sonix RP diagnostic ultrasound system (Ultrasonix Medical Corp., Richmond, BC, Canada). This system uses a 38 mm real-time linear array transducer with 128 channels, 5–14 MHz bandwidth, 50% fractional bandwidth at −6 dB, 40 MHz sampling frequency, and 1 mm beamwidth at the focus. Acquisitions were performed using a center frequency of 10 MHz to maximize the

resolution of the resulting ultrasound images within the transducer bandwidth. No significant attenuation was observed in the visualization of the bone interfaces in the chicken and rabbit samples when using ultrasonic signals in this frequency band.

For the evaluation of the controlled defects, the transducer was positioned approximately 2 cm above the bone inside the water tank and data were recorded at different scanning planes. The size of the bone defects was then estimated from the B-mode images by estimating the maximum diameter of the defect size along the horizontal and vertical axes and averaging the two measurements.

3D scans were generated from the gelatin samples using the freehand acquisition mode. The 3D results were used to corroborate 2D findings but were not used for statistical analysis. Although there are various known methods for 3D ultrasound imaging (Fenster and Downey 2000), for this study, the 3D volume reconstruction was based on the use of a set of parallel 2D B-mode images acquired from the region of interest (Gee et al 2003). This common type of reconstruction is often used in 3D ultrasound imaging applications and usually available in modern diagnostic ultrasound systems (Sakas 2002). In the present case, 128 frames were acquired by sliding the transducer along a linear path over the region of interest to obtain equidistant parallel scans along the bone surface. The 3D reconstruction was then performed by combining the acquired parallel scans into a regular voxel grid using the scan length information and by displaying a volume rendering of the data (Nelson and Elvins 1993). In the Sonix RP system used for this study, the volume visualization has been implemented using a commercially available 3D graphics toolkit (Open Inventor by Mercury with the

VolumeViz extension, VSG, USA), which offers features such as volume rendering and slicing. Basic parameters such as transparency and threshold were set appropriately to optimize each rendering. No additional post-processing techniques were applied to the resulting images.

Statistical analysis of imaging results

2D ultrasound, x-ray and optical imaging results obtained from the bone samples with induced controlled defects were statistically compared using linear regression analysis (least-squares). In order to test for agreement between measurements obtained using ultrasound techniques and measurements obtained using optical microscopy and x-ray, the results were also analyzed using the graphical technique suggested by Bland and Altman (1986, 1999). Application of this method requires the generation of graphs, whereby the differences between optical/x-ray and ultrasound measurements are evaluated against their algebraic means, along with the 95% confidence interval bounds.

The above statistical tests were performed on the results obtained from the mammalian (rabbit) and non-mammalian (chicken) bone samples separately to evaluate and compare accuracy and precision of the ultrasound imaging methods on the two different types of bones.

Results

Intact bones

Figure 1 shows a typical set of results obtained from an intact chicken drumstick sample. Figure 1(a) shows a B-mode image of the chicken sample taken with the transducer parallel to the bone axis. Figure 1(b) shows a B-mode image of the chicken

sample taken with the transducer perpendicular to the bone axis. For the purpose of illustration, schematics indicating the relative position of the ultrasound transducer with respect to the chicken drumsticks are shown. In figures 1(a) and (b), the bone surface is highlighted with arrows. In figure 1(b), note that both the tibia and the fibula can be visualized (indicated by the arrows). This is not the case in figure 1(a), presumably because the fibula is situated in the acoustic shadow generated by the tibia. In both B-mode images shown in figure 1, the soft tissue–bone interface is visualized as a hyperechoic area with respect to the surrounding tissue. However, the thickness of this hyperechoic area may not necessarily represent the actual thickness of the bone cortex, since the high reflection and scattering at the surface of the bone may lead to rapid attenuation in signal strength with penetration depth.

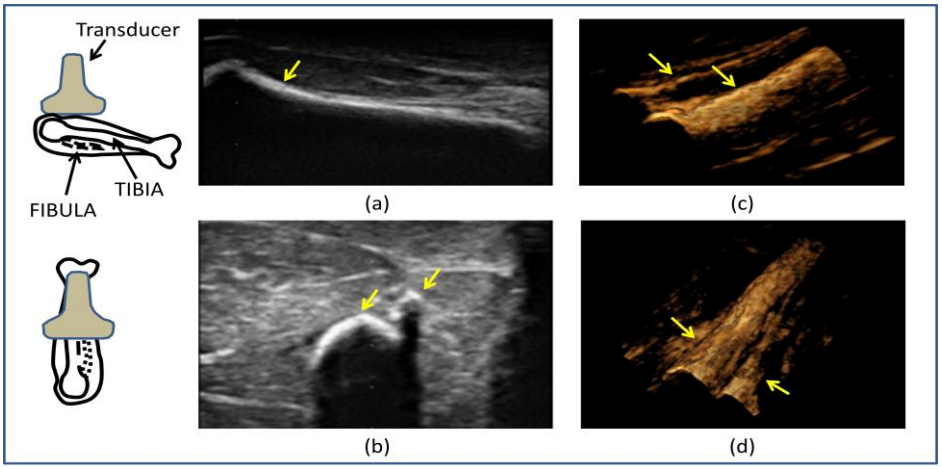

Figure 1. Results obtained from a chicken drumstick containing an intact bone. (a) B-mode image obtained with transducer face parallel to the bone axis (ROI: 2 × 3.8 cm^2); (b) B-mode image obtained with transducer face perpendicular to the bone axis (ROI: 2.5 × 3.8 cm^2); (c) and (d) 3D reconstructions of the chicken tibia. In these images, arrows indicate the soft tissue–bone interfaces. For the 3D reconstruction images, the depth along the main axis of the bone is the transducer's length (3.8 cm).

Figures 1(c) and (d) show typical 3D ultrasound images obtained for the intact chicken bone. In these images, both the tibia and the fibula are visible (indicated by the arrows). In most cases, the 3D renditions allowed easier interpretation and visualization of the bone samples.

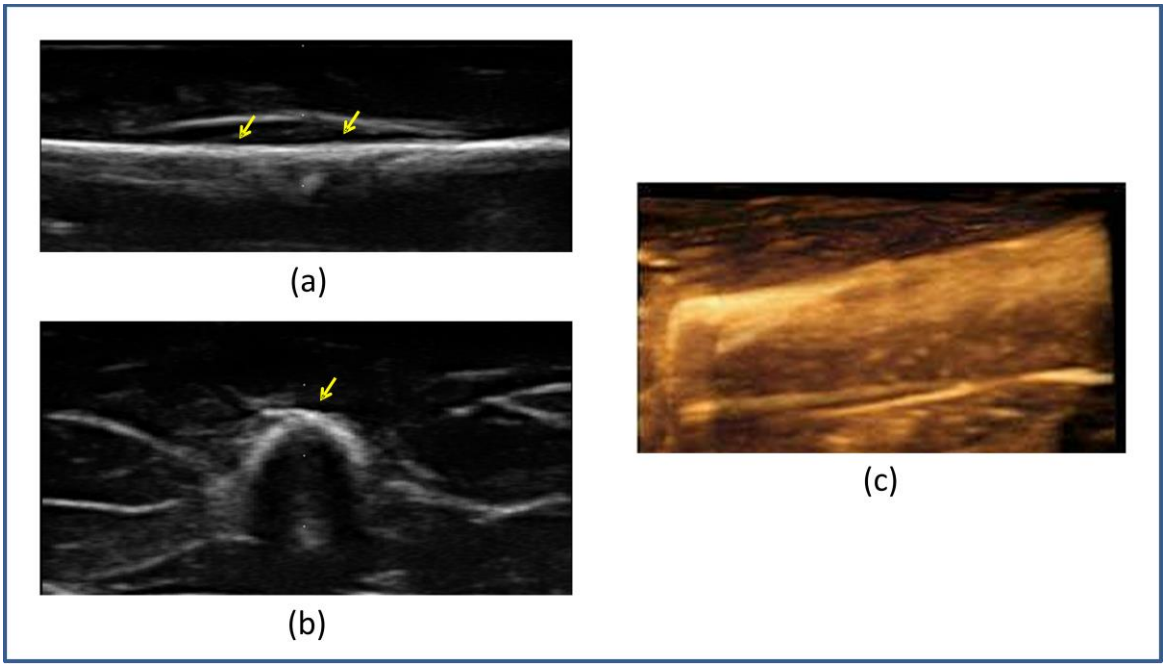

Figure 2. Results obtained from an intact rabbit hindquarter. (a) B-mode image obtained with transducer face parallel to the bone axis (ROI: 2.5 × 3.8 cm^2); (b) B-mode image obtained with transducer face perpendicular to the bone axis (ROI: 2.5 × 3.8 cm^2); and (c) 3D reconstruction of the rabbit bone inside the soft tissue. In the B-mode images, arrows indicate the soft tissue–bone interfaces. For the 3D reconstruction image, the depth along the main axis of the bone is the transducer's length (3.8 cm).

Figure 2 shows a typical set of results obtained from an intact rabbit hindquarter sample. Figure 2(a) shows a B-mode image of the rabbit sample taken with the transducer parallel to the bone axis. Figure 2(b) shows a B-mode image of the sample

taken with the transducer perpendicular to the bone axis. The images show a clear hyperechoic area corresponding to the bone surface (indicated by the arrows) and other hyperechoic regions presumably corresponding to connective tissue or nerve complexes. Figure 2(c) shows a typical 3D reconstruction of the intact rabbit's femur.

Bones with fracture

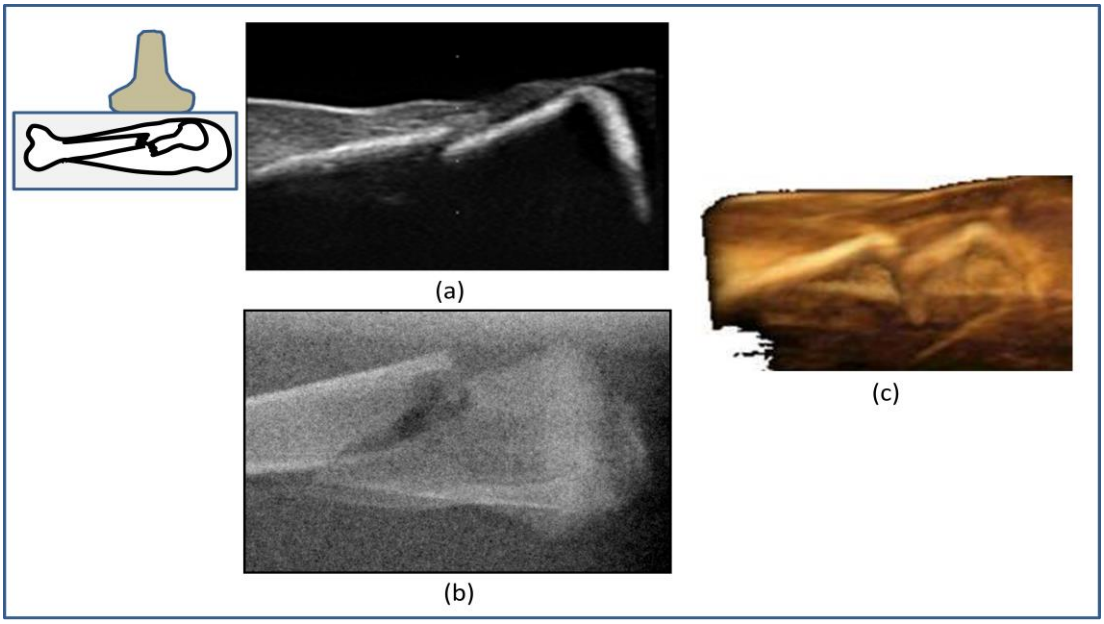

Figure 3. Results obtained from a chicken drumstick containing a fractured tibia (type of fracture: oblique). The chicken drumstick was embedded into a gelatin case for imaging. (a) B-mode image obtained with transducer face parallel to the bone axis (ROI: 2.5 × 3.8 cm^2); (b) x-ray image of same sample (after contrast enhancement). For comparison, the x-ray image was zoomed to approximately match the tissue region visualized in the B-mode image. (c) 3D reconstruction of the fractured specimen. For the 3D reconstruction image, the depth along the main axis of the bone is the transducer's length (3.8 cm).

Figure 3 shows a typical set of results obtained from a chicken drumstick with tibia having a non-union fracture (type oblique). This set of results has to be contrasted

with the set of results shown in figure 1 for the intact bone case. Figure 3(a) shows a B-mode image of the fractured bone taken in the direction parallel to the bone axis. In the B-mode image, the fracture is visible as a step-like discontinuity in the bone surface outline. Similar observations have been reported in the literature for similar types of fractures (Enns et al 2004, Mariacher-Gehler and Michel 1994). Figure 3(b) shows an x-ray image of the same specimen. For comparison, the x-ray image was cropped to show approximately the same tissue region visualized by the B-mode image. Figure 3(c) shows a 3D ultrasound reconstruction of the same specimen. Because of the ability to visualize the scans from different orientations and different cross sections, the 3D rendering allowed a better insight into the fracture by providing information not only about the location of the fracture but also about the maximum point of dislocation within the bone, the type of dislocation and the translation or rotation of the bone due to the fracture. Such information might prove useful for applications that involve fracture alignment or for monitoring and positioning implants and scaffolds (Parmar et al 2009).

Bones with laser-induced controlled defects

Figures 4–8 show selected results obtained from bone samples with controlled laser-induced defects. Figure 4 shows ultrasound imaging results obtained from two chicken bone samples with laser-induced controlled defects with diameter ranging from 0.5 to 4 mm. In figure 4, we show (top to bottom) photographs of the two bones (outside and inside gelatin), B-mode images obtained from scans performed in directions parallel and perpendicular to the axis of the bones and the induced defects, and a collection of 3D ultrasound reconstruction images obtained from different orientation scans (see

figure caption for details). Note that in some of the B-mode images, multiple defects are visible due to the relative spacing between the defects.

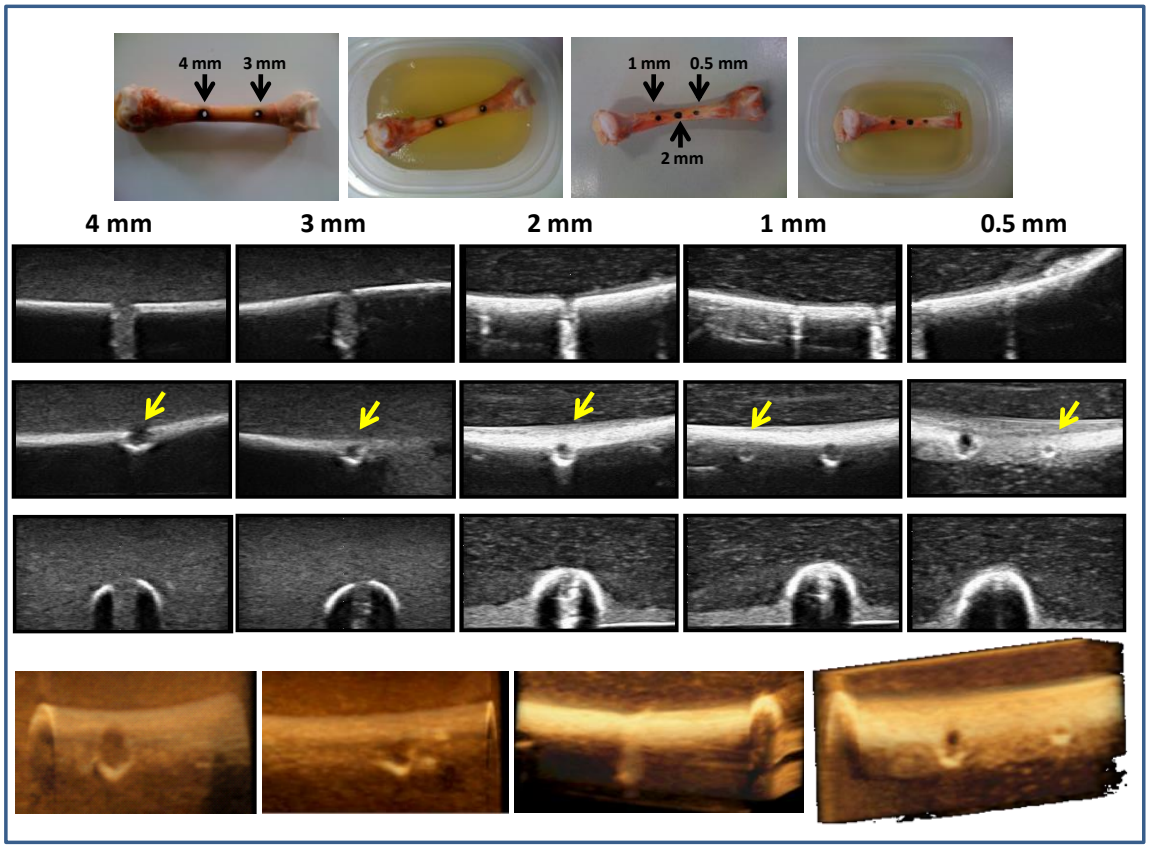

Figure 4. Results obtained from two bone samples with laser-induced controlled defects ranging from 0.5 to 4 mm. From the top, first row: photographs of the two samples (outside and inside gelatin). For the purpose of illustration, the size of the inclusions is indicated in the pictures. Second row: B-mode images of the defects as obtained with the transducer parallel to the bone axis and parallel to the axis of the induced defects. Note that in some of the images, multiple defects are visible due to the relative spacing between the defects. Third row: B-mode images of the defects as obtained with the transducer parallel to the bone axis and perpendicular to the axis of the induced defects. Fourth row: B-mode images of the defects as obtained with the transducer perpendicular to the bone axis and parallel to the axis of the induced defects. Fifth row: sample of 3D reconstruction images of the various defects as obtained by scanning from different orientations. For all 3D reconstruction images, the depth along the main axis of the bone is the transducer's length, i.e. 3.8 cm. Defect sizes (left to right): 4 mm, 3 mm, 2 mm, 1 mm, 0.5 mm.

Figures 5 and 6 show results obtained from four chicken bones having laser-induced defects with diameter ranging from 0.4 to 1.5 mm. In figures 5 and 6 the ultrasound imaging results are benchmarked against corresponding x-ray imaging results. In all cases, the ultrasound images showed strong acoustic contrast between the defects and the surrounding gelatin. In addition, it was feasible to visualize defects located several mmdeep below the bone surface, suggesting that it may be possible for some of the sound energy to penetrate several mm within bone. This observation appeared to be confirmed also by the 3D reconstruction images, showing recesses on both the posterior and anterior surfaces of the bone.

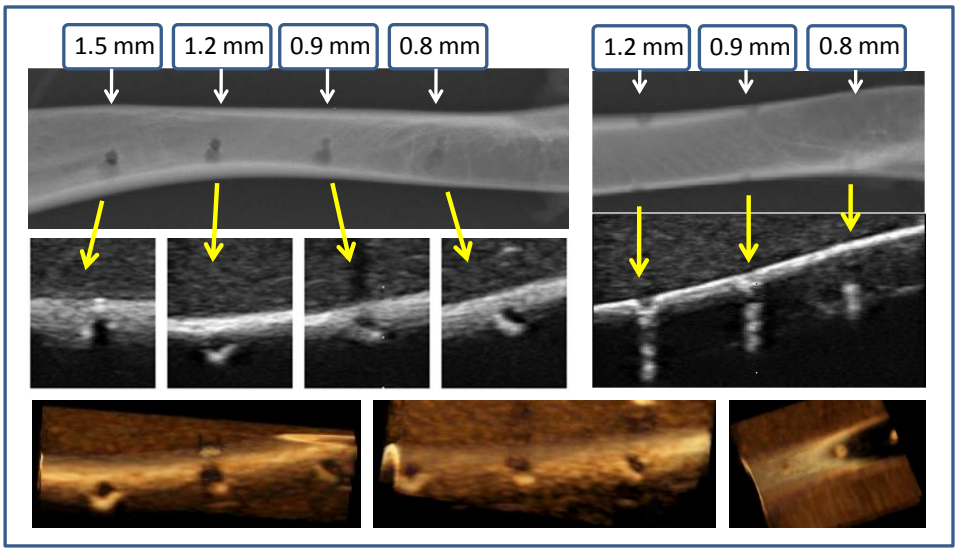

Figure 5. Visualization of laser-induced controlled defects of size 0.8mm-1.5mm in chicken bones using x-ray imaging (top row) and ultrasound imaging techniques (middle and bottom rows). The region of interest for the B-mode images showing the individual defects is approximately 1.5 × 1 cm^2 while the region of interest for the B-mode image showing the defects along the transducer's axis is approximately 1.8 × 3.8 cm^2. For all 3D reconstruction images, the depth along the main axis of the bone is the transducer's length (3.8 cm). Orientation of the imaging plane corresponds to visualization of holes from the side and top (rightmost).

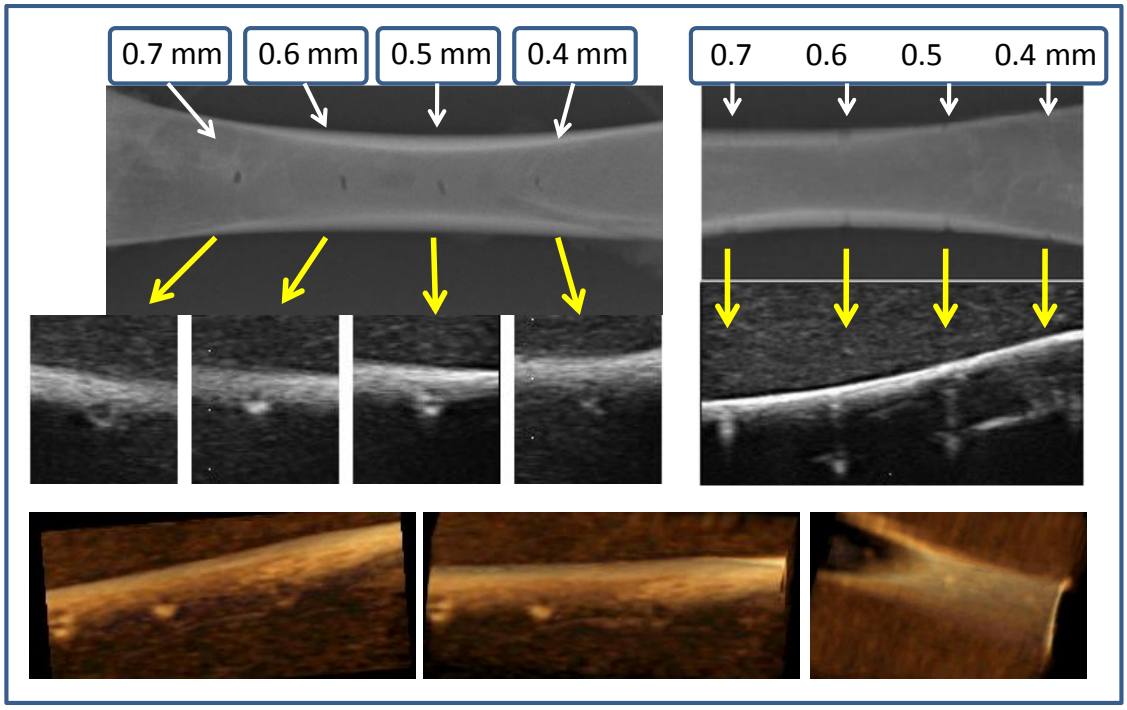

Figure 6. Visualization of laser-induced controlled defects of size 0.4mm-0.7mm in chicken bones using x-ray imaging (top row) and ultrasound imaging techniques (middle and bottom rows). The ROI for the B-mode images showing the individual defects is approximately 1.5 × 1 cm^2, while the ROI for the B-mode image showing the defects along the transducer's axis is approximately 1.8 × 3.8 cm^2. For all 3D reconstruction images, the depth along the main axis is the transducer's length (3.8 cm).

Figure 7 shows selected results obtained from a chicken bone sample with defects ranging from 0.6 to 0.9 mm. In figure 7, we show B-mode image (top row), x-ray image (middle row) and optical microscopy images (bottom row). In the optical images, the laser-induced defects are annotated with circles, which were used to estimate the diameters of the induced defects.

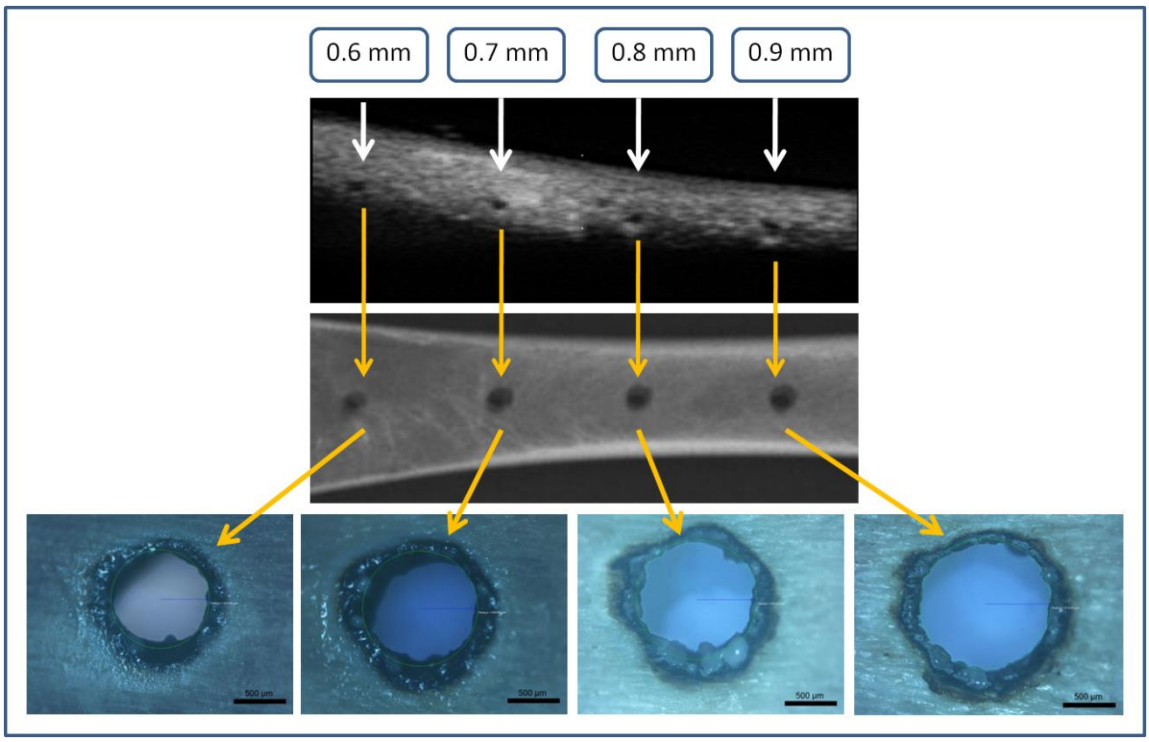

Figure 7. Visualization of laser-induced controlled defects of size 0.9mm-0.6mm in chicken bones using ultrasound (top row), x-ray (second row) and optical microscopy (third row). ROI in the B-mode and x-ray images is 1.5 × 3.8 cm^2.

Similarly, figure 8 shows a comparison of B-mode imaging, x-ray imaging and optical microscopy results obtained from a rabbit bone sample with defects in the range 0.8–1.1 mm. Figure 8 also shows a collection of 3D ultrasound reconstructions obtained for a subset of the experiments performed on the rabbit bone samples with controlled defects.

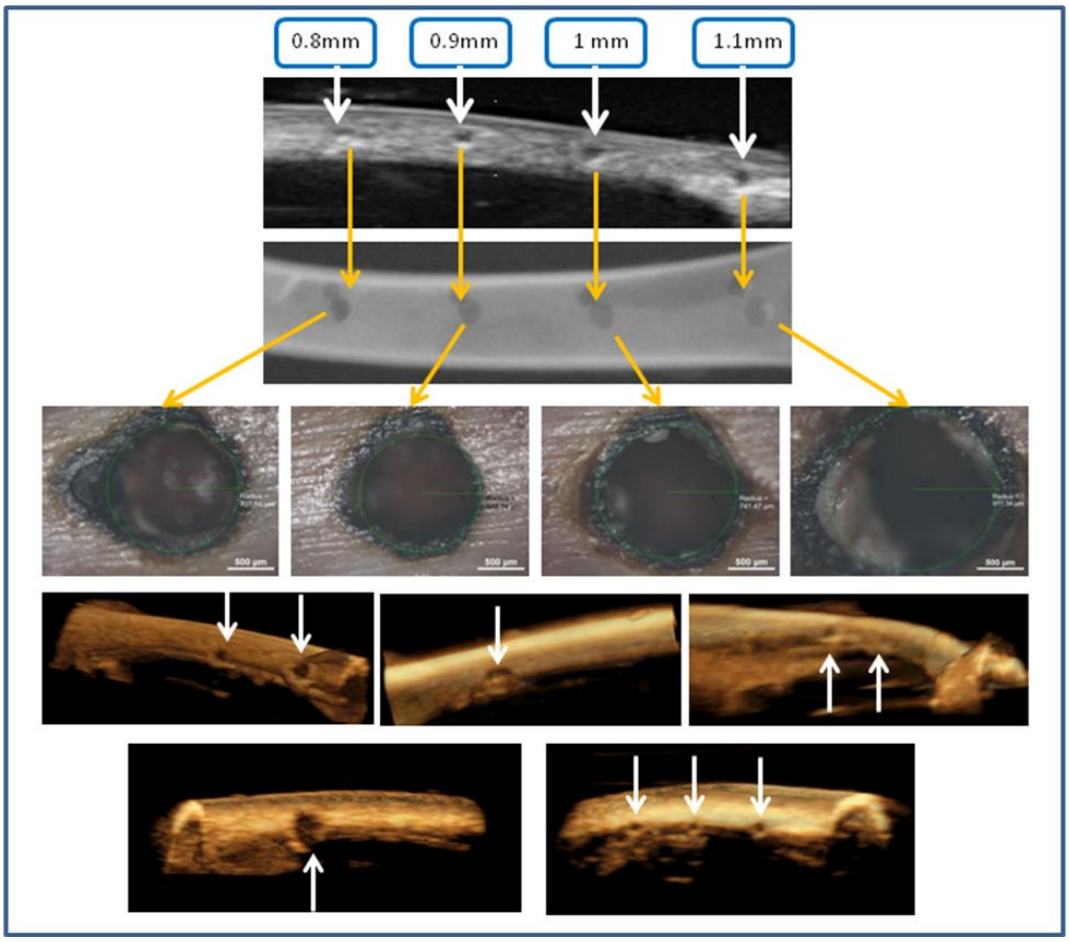

Figure 8. Visualization of laser-induced controlled defects of size 0.8mm-1.1mm in rabbit bones using B-mode ultrasound (top row), x-ray (second row), optical microscopy (third row) and 3D ultrasound (fourth and fifth rows). ROI in the B-mode and x-ray images is 1.5×3.8 cm^2. The 3D images enable visualization of defects with diameters 1.5 mm, 2 mm, 3 mm, 0.6 mm and 0.5 mm.

Statistical analysis

Tables 1 and 2 report measurements of the defect sizes as obtained from the various imaging techniques used for this study. Table 1 refers to data obtained from chicken bone samples and table 2 refers to data obtained from rabbit bone samples.

Table 1. Measurements of controlled defects in chicken bone samples as obtained using optical microscopy (first and fourth columns), B-mode imaging (second and fifth columns) and x-ray imaging (third and sixth columns). All dimensions are in μm. In the optical images, all defects are displayed at 50× magnification. B-mode and x-ray images are displayed on the same scale.

Diameter (Optics)	Diameter (B-mode)	Diameter (X-ray)	Optical image	B-mode image	X-ray image
408	740	684	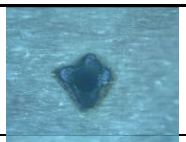	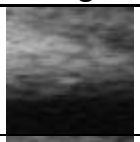	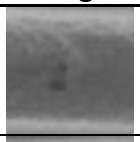
568	839	787	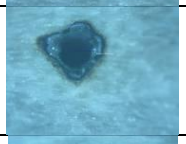	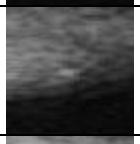	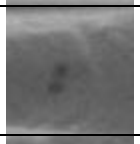
628	986	956	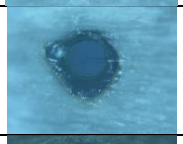	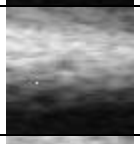	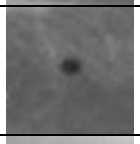
819	1173	1100		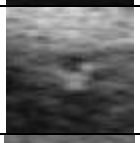	
940	1046	1293	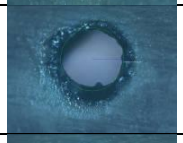	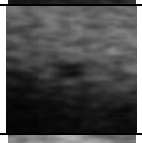	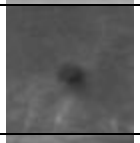
1097	1093	1574		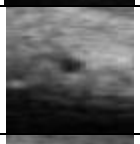	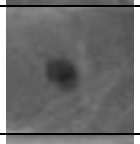
1141	1457	1687	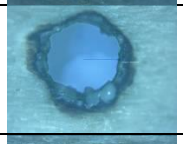	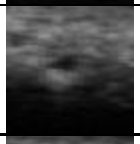	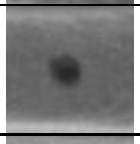
1236	1820	1799	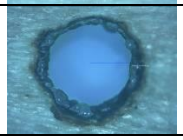	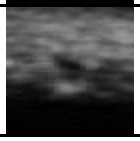	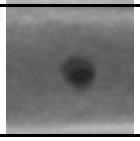

Table 2. Measurements of controlled defects in rabbit bone samples as obtained using optical microscopy (first and fourth columns), B-mode imaging (second and fifth columns) and x-ray imaging (third and sixth columns). All dimensions are in μm. In the optical images, all defects are displayed at 50× magnification. B-mode and x-ray images are displayed on the same scale.

Diameter (Optics)	Diameter (B-mode)	Diameter (X-ray)	Optical image	B-mode image	X-ray image
675	602	460	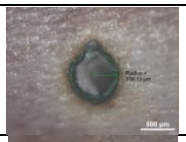	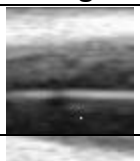	
592	702	870	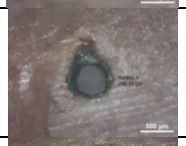		
995	752	915	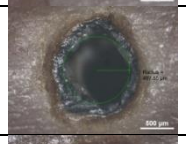	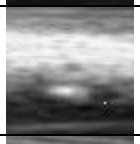	
1022	802	1020	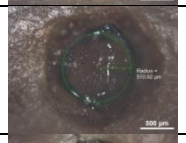	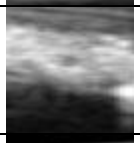	
1236	852	1355	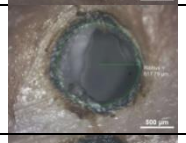	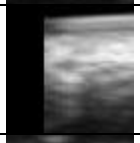	
1414	1102	1270	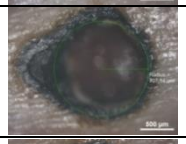	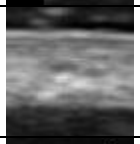	
1298	1153	1540			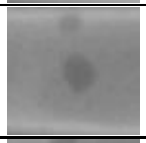
1483	1353	1565	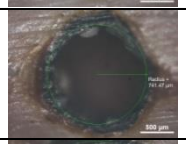	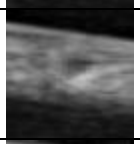	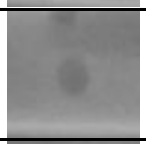
1823	1304	1620	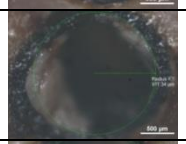	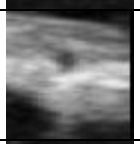	
2070	1605	1985	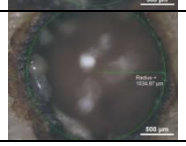	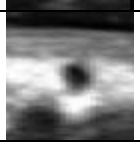	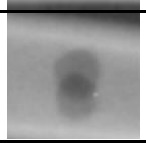

The first column of each table shows the actual defect diameters as estimated using optical microscopy; the second column shows the defect diameters as estimated using B-mode imaging; the third column shows the defect diameters as estimated using x-ray imaging and the last three columns show optical, B-mode and x-ray snapshots of the defects.

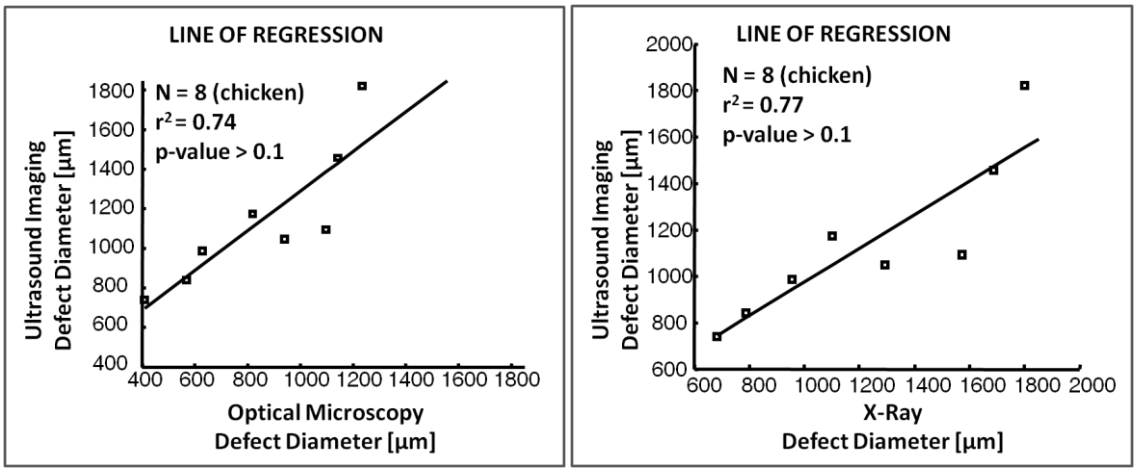

(a) (b)

Figure 9. (a) Comparison of defect measurements in chicken bones as obtained using B-mode imaging and defect measurements as obtained using optical microscopy. (b) Comparison of defect measurements in chicken bones as obtained using B-mode imaging and defect measurements as obtained using x-ray imaging.

Figure 9 shows the results of the statistical comparison between ultrasound findings and optical microscopy findings (figure 9(a)) and the results of the statistical comparison between ultrasound findings and x-ray findings (figure 9(b)) for the chicken bone samples. In each scatter diagram in figure 9, the data points are represented with

'squares' and the solid line represents the linear regression fit. In each graph, we also report the determination coefficient (r^2) and the p-value for the data shown.

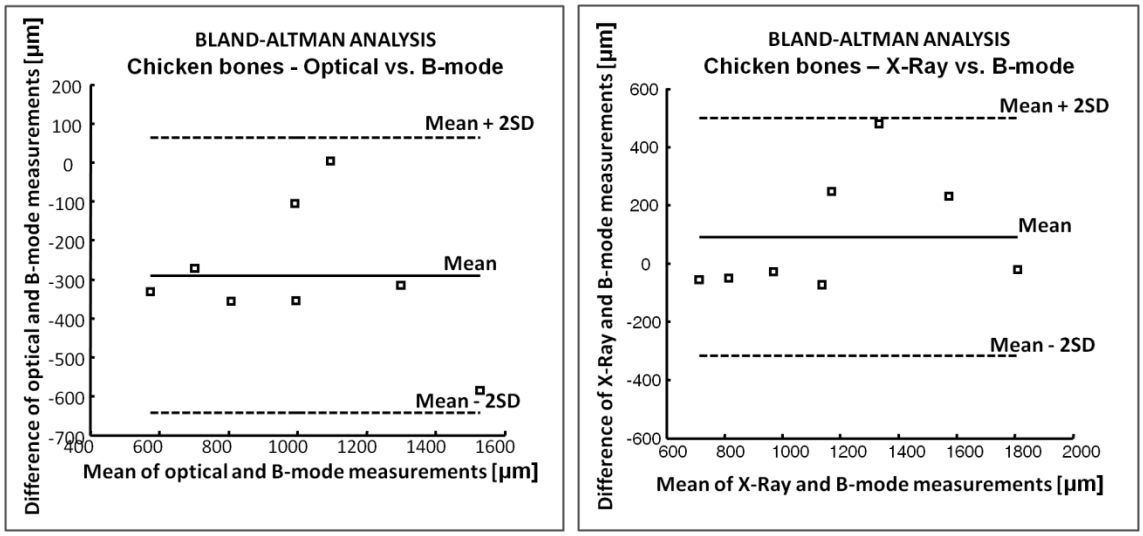

(a) (b)

Figure 10. Bland–Altman plot of difference of measurements of defect sizes in chicken bones as obtained using B-mode imaging and those using (a) optical microscopy and (b) x-ray imaging.

The Bland–Altman analysis technique to test for agreement of the obtained values returned a 95% confidence interval of ±353 µm for the ultrasound–optical microscopy comparison case, and ±408 µm for the ultrasound–x-ray comparison case. These intervals are indicated as the dashed lines corresponding to MEAN ± 2SD (standard deviation) on figures 10(a) and (b). Figures 11 and 12 show the results of a similar statistical analysis carried out on the defects induced in the rabbit bones.

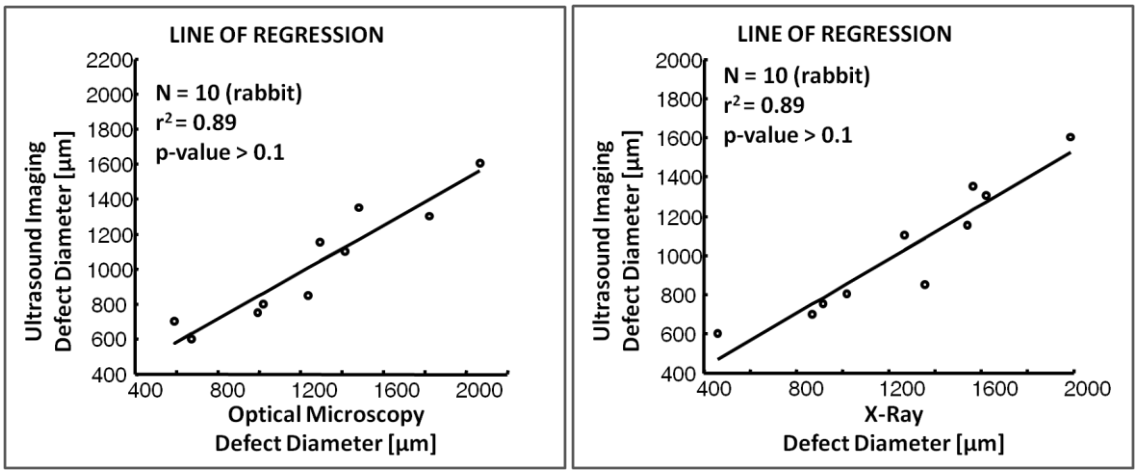

(a) (b)

Figure 11. (a) Comparison of defect measurements in rabbit bones as obtained using B-mode imaging and defect measurements as obtained using optical microscopy. (b) Comparison of defect measurements in rabbit bones as obtained using B-mode imaging and defect measurements as obtained using x-ray imaging.

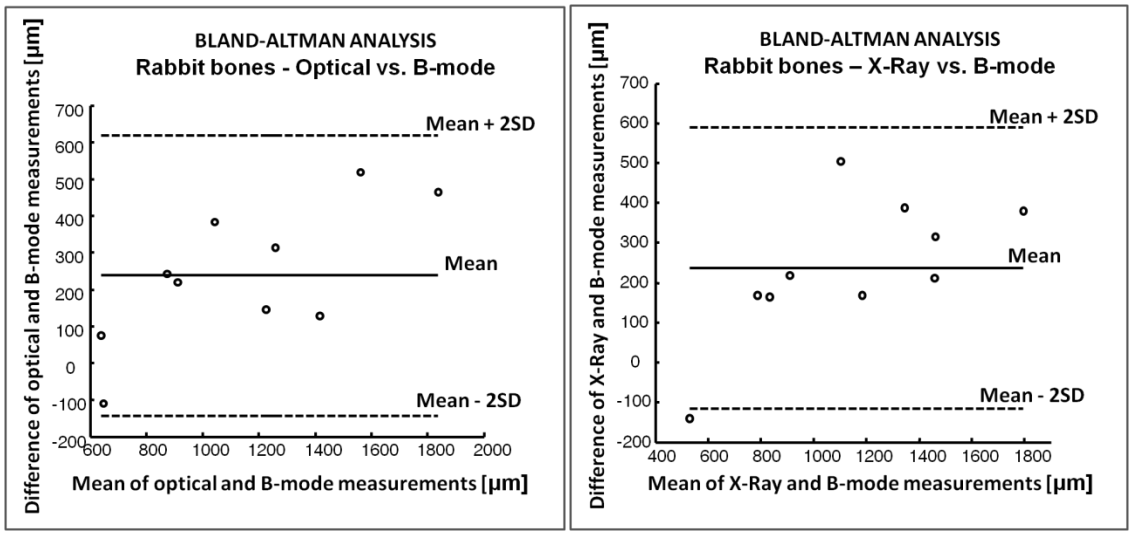

(a) (b)

Figure 12. Bland–Altman plot of difference of measurements of defect sizes in rabbit bones as obtained using B-mode imaging and those using (a) optical microscopy and (b) x-ray imaging.

For the rabbit data, the test for agreement shows that the ultrasound results agree with the optical microscopy values to within ±380 μm (at a 95% confidence level) and to within ±353 μm with the x-ray values (at a 95% confidence level). These intervals are indicated in figures 12(a) and (b), respectively.

According to our statistical analysis, ultrasound results are not just highly correlated with corresponding x-ray and optical microscopy results, but they also show a high degree of agreement at a 95% confidence level with these alternate imaging modalities, as demonstrated using the Bland–Altman analysis. This statistical analysis demonstrates that image quality of diagnostic ultrasound techniques for assessing controlled bone defects is comparable with the image quality of x-ray and optical imaging methods both in mammalian and non-mammalian bones. These preliminary results also suggest that ultrasound imaging methods can be used to estimate a wide range of controlled bone defects with high accuracy and sensitivity and at diagnostic resolutions.

Discussion

We have reported preliminary results of a controlled experimental study aimed at understanding performance limitations of ultrasound imaging techniques for the characterization of bone surface defects both in mammalian and non-mammalian animal samples *in vitro*. To our knowledge, this work represents the first systematic study to date that analyzes the performance of standard, clinical grade, diagnostic ultrasound methods to image bone defects of controlled size and shape and statistically compares

the findings with those obtained using commonly employed x-ray and optical imaging techniques.

Statistical analysis of the ultrasound imaging results obtained from the experimental controlled study reported in this paper demonstrates the ability of ultrasound imaging methods to visualize a wide range of defect sizes with high accuracy and precision. These results may have several important implications in the evaluation of ultrasound techniques as a new diagnostic tool for bone imaging applications. First, the ultrasound imaging measurements were found to agree well with those obtained using x-ray and optical microscopy techniques (at a 95% confidence level). The size of the defects as measured from the ultrasound images was found to correlate well with the actual size of the defects as estimated from the x-ray and optical images. The ultrasound imaging results were found to be accurate within approximately ± two ultrasonic avelengths (at a 95% confidence level) both in the chicken and rabbit samples. Second, at the diagnostic frequencies used for this study, it may be possible to detect *in vitro* bone defects as small as 400 μm. This information might prove important for the diagnosis of complete and incomplete fractures (such as hairline fractures in the elbow and leg), for monitoring bone healing and to image implants and scaffolds for orthopedic applications. For this study, we did not consider bone defects with size below 400 μm, due to technical limitations of our laser system used to create the bone defects. It may be expected that, as the defect size becomes comparable with the ultrasonic wavelength, physical imaging limitations may deteriorate image quality, resulting in a reduction of the corresponding contrast-to-noise ratio, thus compromising the ability to accurately

measure the defect. Third, accuracy and precision of ultrasound imaging methods to assess bone surface defects appears to be independent of the type of bone or the species of vertebrates. Statistically equivalent results were observed both in mammalian and non-mammalian bone samples. Thus, similar performance might be feasible in applications that involve imaging of bones in other animal species or in human bone pathology.

To our knowledge, the study reported in this paper is also the first work that demonstrates the feasibility of 3D ultrasound imaging of sub-millimeter bone surface defects. Our results demonstrate that it is technically feasible to generate 3D reconstructions of bone surfaces and fractural defects using diagnostic ultrasound techniques with high accuracy and contrast-to-noise ratio both in mammalian and non-mammalian bones. The application of 3D ultrasound imaging techniques helped in the visualization of the bone surfaces and allowed easier interpretation of the ultrasound results. In general, the ability to rotate the reconstructed volume in order to optimize visualization is a great advantage over any 2D imaging modality. As for CT techniques, 3D ultrasound reconstruction techniques could be particularly useful for bone alignment and in applications where 2D images may provide insufficient information for bone assessment. No statistical analysis has been performed on the 3D imaging results yet since these techniques are still under development and a fair assessment of their performance would require the use of CT 3D reconstruction methods, which are slow, costly and not readily available. Such statistical study is left for future work. However, all bone defects analyzed in this study could be visualized in the corresponding 3D

ultrasound reconstructions. Such an ability to reliably detect sub-millimeter defects in real time, non-invasively and without radiation could have a significant impact in the management of bone fractures and other bone abnormalities. Furthermore, the ability to reliably detect small fracture displacements of the order of 1–2 mm could lead to preclusion of operative procedures. These imaging methods could also be used to monitor physiological changes associated with primary and metastatic tumors in the bone, which can have a significant impact on the long-term treatment. However, due to the limitations of the planar scanning, the 3D reconstruction technique employed in this study did not allow visualization of the entire bone surface. In addition, the generation of good quality 3D reconstructions required skilled operators and, in some cases, multiple attempts especially when imaging small and 'curved' bones (such as rabbit bones). Alternate 3D ultrasound reconstruction techniques for complete visualization of bone surface properties are currently under investigation.

Based on these preliminary results, the major advantages of ultrasound techniques with respect to x-ray for bone imaging applications include visualization of multiple scanning planes and 3D information in real time; availability of structural information regarding both soft tissue and bone and soft tissue–bone interaction; no patient exposure to radiation; better compliance with sensitive tissues surrounding bone fractures (Banal et al 2006, Bodner et al 2005). As opposed to x-ray, however, the ultrasound techniques used for this study, in their present form, do not allow visualization of complete bone surface, require skilled operators and, in some cases, appear to overestimate the defect sizes. In our study, the ability to visualize sub-

millimeter defects using B-mode or x-ray imaging was found to be sensitive to the orientation of the sound or light source with respect to the defect axis. This was found to be more prominent in the case of rabbit bone defects, since these bones are more regular in shape than chicken bones. In such cases, the use of 3D imaging techniques appeared to partially overcome this limitation and improved the visualization of the defects. In general, the lateral relative spacing between the defects appeared to be preserved in the ultrasound images as compared to the corresponding x-ray images (figures 4–8). However, the axial location of the defects inside the sample, the actual bone thickness, and the location of the bones inside the tissues could be misrepresented in the ultrasound images due to refraction effects. Previous studies have reported up to 5% errors due to the mismatch of the speed of sound between tissues and bones, which, however, can be corrected through the application of appropriate registration techniques (von Berg et al 2004). We did not apply any correction technique as this factor did not affect our statistical results.

Based on these results, ultrasound imaging techniques may have significant potential as a new, cost-effective and real-time modality for bone imaging applications. With respect to the ability of successfully applying these techniques to image human bone pathology, it is important to note that the results reported in this study represent an optimistic scenario due to the nature of the *in vitro* experiments. It may be expected that the bone size, location inside the tissue and the scattering generated by the surrounding soft tissue could compromise the quality of the resulting ultrasound images. In the future, however, it may be possible to further improve the accuracy of these methods by

applying advanced signal and image processing techniques that might allow enhancing bone surface information and improving image quality. In this regard, we are currently investigating the use of edge detection and intensity slicing image processing methods to improve visualization of bones embedded in soft tissues (Parmar et al 2009, Gonzalez and Woods 2008).

Conclusions

This study demonstrates that 2D and 3D ultrasound imaging techniques can be used to assess bone defects such as non-unions, fractures, and controlled defects in real-time and with high accuracy, contrast-to-noise ratio and resolution. Ultrasound imaging results were found to be in good agreement with corresponding x-ray imaging and optical imaging results. The availability of 3D ultrasound reconstructions of bone surfaces allowed improved visualization and easier interpretation of the ultrasound images of bones and bone defects. Based on this study, it is concluded that, in the future, ultrasound imaging techniques might provide a cost-effective and safe diagnostic tool alternative to standard imaging methods currently used in bone applications.

3. 3D ULTRASOUND IMAGING OF COMPLEX SKELETAL DEFECTS AND FRACTURES. PRELIMINARY RESULTS

Introduction

X-rays and Computerized Tomography (CT) are currently the gold standards for two-dimensional (2D) and three-dimensional (3D) imaging of skeletal tissues. The strength of these modalities lies in their superior sensitivity and specificity in the detection of skeletal pathologies and the associated skeletal response to the underlying etiology. These imaging methods are used in a number of musculoskeletal applications, such as the characterization of fractures and the temporal monitoring of subsequent healing, diagnostic patterns of involvement and bony response, tumors, measurement of deformity and surgical planning for their correction (Greenfield 2008, DeLee et al 2009, Abdel-Dayem 1997, Krishnamurthy et al 1977, Kalpakcioglu et al 2008, Dijkman et al 2010). The weaknesses of these modalities, however, rest in their reliance upon radiation for image generation, the requirement of large, often structurally fixed, machinery, and the high costs. In particular, radiation exposure for the radiographic diagnosis, treatment (operative or non-operative), and follow-up of fractures can approach levels of 10 mSv, which may increase cancer risk (Sodickson et al 2009, Smith-Blindman et al 2009, Berrington de Gonzalez et al 2009, Redberg 2009, Richards et al 2010, Redberg and Smith-Bindman 2014), especially in children. Radiation of axial structures (shoulder, pelvis, hip, or spine), often coupled with CT, poses a significantly greater risk (Redberg 2009, Richards et al 2010).

While ultrasound imaging techniques have historically been less sensitive and specific for the diagnosis of skeletal disorders, some of their distinctive characteristics have long made them an attractive alternative imaging modality to standard x-ray and CT methods for bone assessment (Banal et al 2006, Bodner et al 2005, Wakefield et al 2000, Hirai et al 1996, Williamson et al 2000, Hübner et al 2000). Potential advantages of these techniques include safety (no radiation), real-time imaging, portability, cost-effectiveness, and musculoskeletal physician operability. While 3D ultrasound imaging methods are widely deployed for surface structural and functional imaging in several medical areas including obstetrics, gynecology and cardiology, their utility for musculoskeletal imaging applications remains largely unexplored. Re-exploration of these methods is warranted, in light of the emergence of novel ultrasound technologies and systems with superior 3D and 4D ultrasound imaging capabilities and automated features.

The majority of the work retrievable in the literature on ultrasound bone imaging refers to the use of quantitative low-frequency, 2D ultrasound methods to assess bone density or detect bone abnormalities (Njeh et al 1997, Prins et al 1998, Gluer 1997, Protopappas et al 2008). Recent progress made in the field has also enabled 3D tomographic reconstruction of bones using a combination of reflection, transmission and refraction mode (Lasaygues and Lefebvre 2001, Lasaygues et al 2005). However, these techniques are in general not suitable for clinical applications since they require elaborate experimental setups and for the samples to be placed in water, operate at non-diagnostic frequencies (500kHz) implying limited special resolutions and are

computationally intense. A similar tomographic reconstruction of bones using B-mode imaging has also been demonstrated (Sehgal et al 2008). There is still a paucity of work that focuses on the use of ultrasound bone imaging using clinically available ultrasound scanners despite data showing promising results in children and military applications (Hacihaliloglu et al 2009, Karjalainen et al 2009, Hacihaliloglu et al 2008, Hübner et al 2000, Cho et al 2010, Brooks et al 2004). Only a few studies have been reported to date that investigate the use of 3D ultrasound techniques for bone applications (Ross et al 2009, Parmar et al 2009). 3D ultrasound imaging methods can potentially be very informative and particularly suitable for the visualization of bones and the accurate detection of bone surface defects due to the large mismatch of acoustic impedance between soft tissues and bones (Parmar et al 2009). They could serve as complementary methods to X-Rays and CT, particularly in intra-operative and emergency medicine scenarios. The availability of these methods could enable fast diagnosis of fractures and monitoring of bone healing in a radiation-free environment, hence significantly impacting the management of a wide range of bone abnormalities.

We have recently reported a study, which has demonstrated that ultrasound imaging techniques can be used to assess bone defects with accuracy and resolution comparable to that of optical and X-ray methods in ex-vivo bone samples (Parmar et al 2010). The study was performed using excised bones with induced controlled defects ranging from a fraction of a millimeter to several millimeters. While important and unique in its assessments, the study did not investigate the use of ultrasound imaging

techniques for more complex and realistic defects such as fractures or shattered bones with intact soft tissue.

In this paper, we primarily focus on the assessment of bones in intact tissue samples. More specifically, we aim at investigating the feasibility of using standard 3D ultrasound methodologies for imaging of appendicular skeletal defects and complex bone fractures in a variety of tissue samples. A statistical analysis of the imaging contrast obtained when using these 3D methods for bone imaging is reported. Given the limited availability of literature on 3D ultrasound bone imaging, the results of this study can serve as a foundation for new and more complex studies involving the use of ultrasound imaging techniques for orthopedic applications.

Materials and Methods

Ultrasound imaging experiments were performed on bone samples of tibiae obtained from both mammalian (rabbit, sheep and dog) and non-mammalian (chicken) animal samples. Unless otherwise specified, the reported results refer to specimens with intact soft tissue.

Table 3 summarizes the number of samples, animal type, bone status (intact or fractured) and number of experiments performed in this study. All data reported in this table refer to samples with intact soft tissue. The number of samples/animals largely depended on their availability at the time of the experiments (for example, chicken drumsticks were easily retrievable from local markets, while rabbit, sheep and dog samples were provided by independent ongoing studies).

Table 3. Summary of the number of cases of intact and fractured tibias analyzed in various species (chicken, rabbit, sheep and canine) using ultrasound imaging.

Species	Bone	Integrity	# cases
Chicken	Tibia	Intact	12
		Fractured	10
Rabbit	Tibia	Intact	5
		Fractured	1
Sheep	Tibia	Intact	2
		Fractured	1
Canine	Tibia	Intact	4
		Fractured	4

While the majority of the samples used in the current study involved bones within intact soft tissue samples, we also carried out some tests on excised bones (i.e., without the soft tissue). This was done so as to aid comparison of the results obtained from samples containing intact soft tissue with "ideal" imaging results obtained from the same bones without the soft tissue interfering with the modality. These specimens were embedded within clear gelatin phantoms so as to generate good quality 3D scans. The phantoms were created by mixing 5% by weight of gelatin in boiling water, as described in Kallel et al (Kallel et al 2001).

All samples were scanned using a Sonix RP diagnostic ultrasound system (Ultrasonix Medical Corp., Richmond, BC, Canada). This system uses a 38 mm real-time linear array transducer with 128 channels, 5-14 MHz bandwidth, 50% fractional

bandwidth at -6 dB, sampling frequency of 40 MHz, and 1 mm beamwidth at the focus. Acquisitions were performed using a transmission frequency of 10 MHz. No significant attenuation was observed in the visualization of the soft tissue-bone interface when using ultrasonic signals in this frequency band. The focal spot was set at the location of the soft tissue-bone interface.

For each sample, sets of 128 equidistant and parallel B-mode images (2D ultrasound images) were acquired from the sample in the freehand acquisition mode both in a direction parallel to the bone axis as well as in a direction perpendicular to the bone axis (Gee et al 2003). The time taken to perform a 3D scan was in the typical range of a sonographic test (5-15 minutes). Once the bone was located in the B-mode image (typically within a few minutes), performing the 3D scan typically required less than a minute. In some cases, more than one 3D scan was performed but, in any cases, no more than four 3D scans were executed from the same area of interest. From each set of parallel B-mode images, a 3D volume was reconstructed by combining the images into a regular voxel grid using the scan length information (measured using a ruler) and by displaying a volume rendering of the data (Nelson and Elvins 2003). A simplified schematic of the 3D reconstruction procedure used in study is shown in figure 13.

In the Sonix RP system used for this study, the volume visualization is implemented using a commercially available 3D graphics toolkit (Open Inventor by Mercury with the VolumeViz extension, VSG, USA), which offers features such as volume rendering and slicing. Following the reconstruction process, customized intensity-level post-processing imaging techniques were applied to qualitatively enhance

image quality of the resulting 3D reconstructions (Parmar et al 2010, Gonzalez and Woods 2008). These post-processing techniques were applied only to the 3D reconstructions with the sole purpose of visually improving bone surface localization.

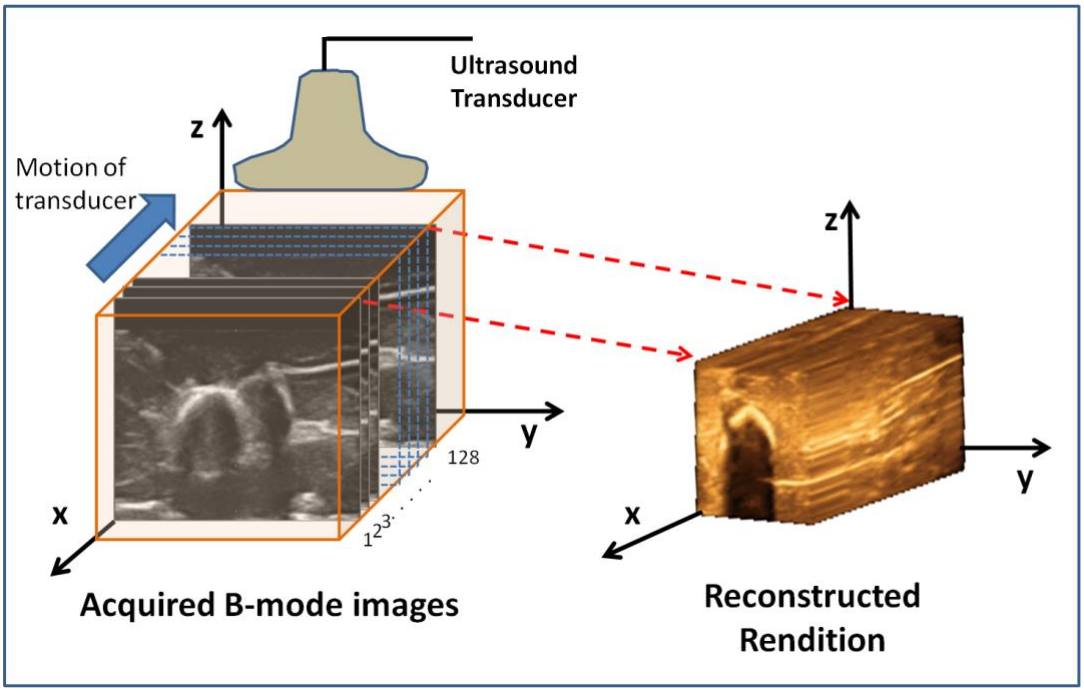

Figure 13. Schematic of the 3D reconstruction technique employed for this study.

A statistical analysis of the performance of the post-processing images was carried out to obtain a measure of the contrast between bone tissue and soft tissue in the 3D renditions. This was done by identifying and quantifying the proportion of pixels in the 3D renditions that corresponded to bone tissue. To simplify the analysis, an assumption was made that the anatomical features demonstrating the highest echogenicity in the region were part of the bone. As a result, a semi-automated approach

was taken for identifying these pixels: a user first manually selected a ROI that definitively corresponded to the bone in each image; a threshold was computed as the mean intensities of the pixels in this region; a 2D median filtering was applied to the entire image; a thresholding operation was applied to eliminate pixels corresponding to lower intensities (soft tissue); the number of non-zero pixels in the thresholded image was counted and normalized with respect to the non-zero pixels in the original image. For the remaining of the study, we will refer to this number as the "ratio number". Higher ratio numbers should correspond to qualitatively better bone segmentations. Table 4 summarizes the various cases used for the statistical analysis.

Table 4. Summary of the number of images of intact and fractured tibias in various species (chicken, rabbit, sheep and canine) used for statistical analysis.

Species	Integrity	# images
Chicken	Intact	8
Chicken	Fractured	8
Rabbit	Intact	6
Sheep	Intact	9
Canine	Intact	5
Canine	Fractured	6

Results

The first set of images shown in figures 14 and 15 were obtained from excised bones. Additionally, the ultrasound bone imaging results obtained from these samples were also validated against X-rays and CT, which are the methods traditionally used to assess bone defects.

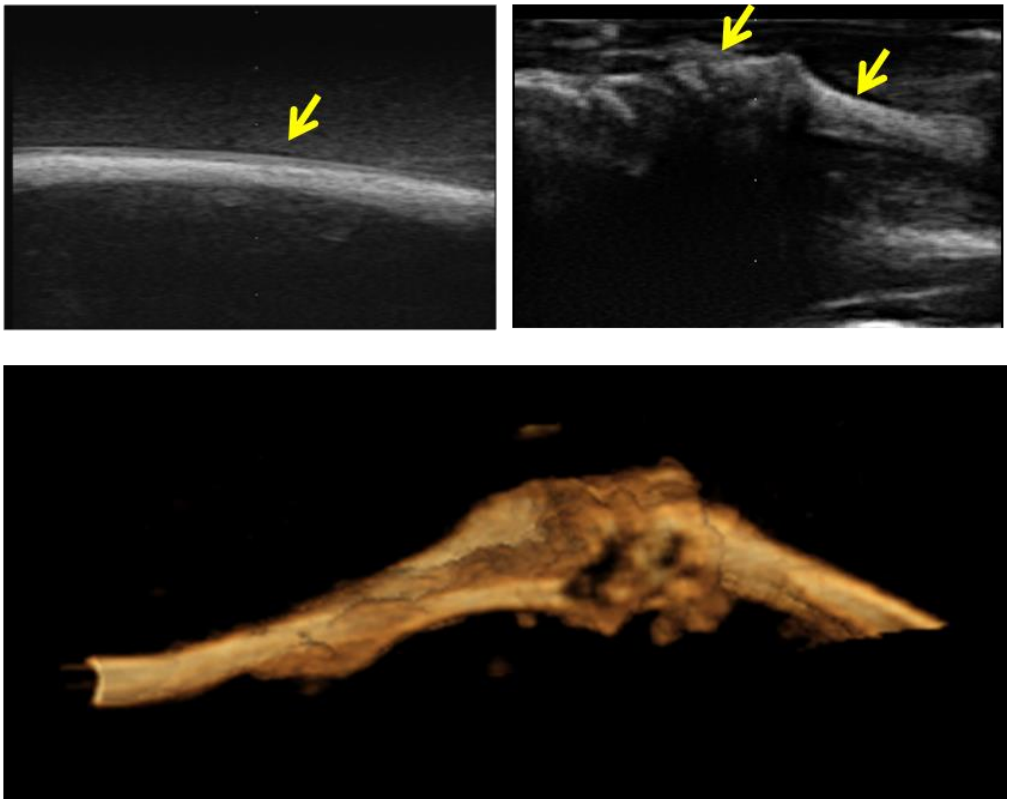

Figure 14. Typical results obtained from a rabbit specimen embedded in gelatin. Arrows indicate the bone surface (a) B-mode image of the rabbit tibia taken parallel to the bone axis (ROI = 2.5 x 3.8 cm2); (b) B-mode image of the rabbit knee joint (ROI = 2.5 x 3.8 cm2); (c) 3D rendition of the rabbit bone specimen.

Figure 14 shows a typical set of results obtained from an intact rabbit specimen. Scans were performed to visualize the femur along with a portion of the tibia and the knee joint. Figure 14 (top row) shows B-mode images visualizing the bone surface in two selected Region(s) Of Interest (ROI). Figure 14 (bottom row) shows an image of the 3D volume rendition of the rabbit bone specimen obtained by performing a freehand scan.

Figure 15 shows selected results that help comparing the 2D and 3D ultrasound imaging results with conventional orthopedic imaging modalities. Specifically, these are results obtained from a chicken bone specimen with two sub-millimeter laser-induced controlled circular defects. Details of the process used to induce the defects are described in our earlier paper (Parmar et al 2010). The figure shows the co-registered imaging results obtained from two independent 2D modalities - B-mode (top, left) and X-rays (bottom, left) applied to the specimen with the two defects. Figure 15 also shows two co-registered 3D renditions of the sample obtained using ultrasound (top, right) and micro-CT (bottom, right).

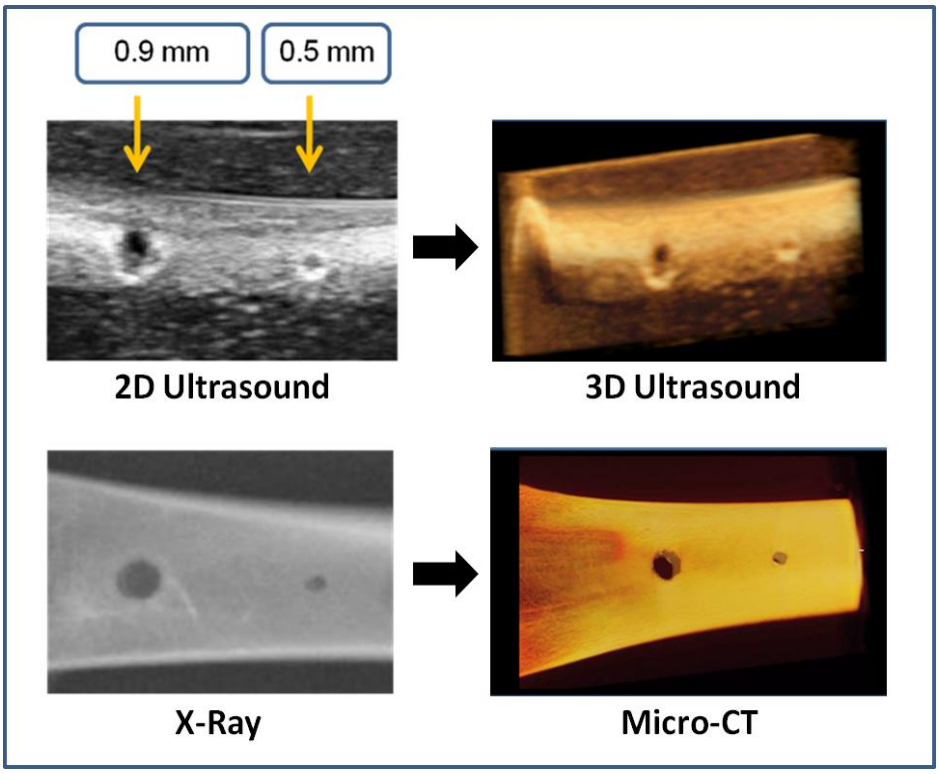

Figure 15. Typical results obtained from a bone sample (chicken) with two laser-induced controlled defects. The figure shows the multi-modality imaging approach used to validate the ultrasound imaging findings. (top, left) B-mode image of a bone specimen with two induced controlled defects (ROI = 2.5 x 3.8 cm^2); (bottom, left) X-ray image of the (same) bone specimen (ROI = 2.5 x 3.8 cm^2); (top, right) 3D ultrasound rendition of the bone specimen; (bottom, right) micro-CT image of the bone specimen.

As it can be seen from these results, at the diagnostic frequencies used for this study, ultrasound imaging techniques allow depiction of sub-millimeter controlled bone defects with high contrast-to-noise ratio and resolution. These preliminary results also show that the image quality obtainable using standard ultrasound imaging methods, when compared to that obtainable using established X-rays and micro-CT methods, may be adequate for deriving clinically relevant information. It is noteworthy that the time

required for the generation of the 3D ultrasound rendition shown in figure 15 was approximately a second, while the time required for the generation of the micro-CT image shown in figure 15 was of the order of hours.

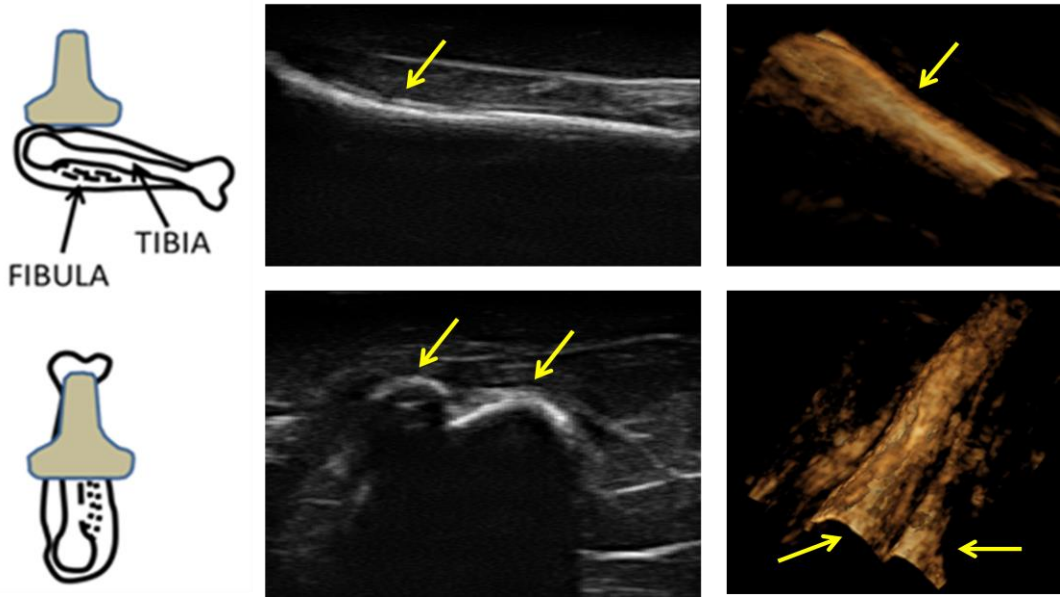

Figure 16. Typical results obtained from an intact bone specimen (chicken) with the soft tissue left intact. (a) B-mode image of the chicken specimen (ROI = 2.5 x 3.8 cm^2). The tibia is highlighted with an arrow. This B-mode image is taken with the transducer parallel to the bone surface; (b) B-mode image of the same specimen taken with the transducer perpendicular to the bone surface; (c) and (d) 3D renditions of the chicken tibia. Arrows indicate the bone-soft tissue interface.

The remaining results pertain to images obtained from samples where the soft tissue was left intact (not in gelatin). Figures 16-17 show typical examples of 2D and 3D ultrasonic bone assessment in a chicken drumstick with intact tibia (figure 16) and fractured tibia (figure 17). Figure 16 (top row) shows 2D and 3D images of an intact tibia taken with the transducer parallel to the bone axis. Figure 16 (bottom row) shows

2D and 3D images of an intact tibia taken with the transducer perpendicular to the bone axis as also evident from the schematics on the left of the figure. In the B-mode images, the soft tissue bone-interface is visualized as a hyperechoic area with respect to the surrounding tissue. In all images, the tibia is clearly distinguishable from the surrounding tissue. However, in the 3D renditions, it is possible to clearly visualize both the tibia and the fibula.

Figure 17, on the other hand, shows the results of 2D and 3D ultrasound imaging performed on a fractured tibia using a layout similar to that used in figure 16. In the B-mode images, the fracture is visible as a step-like discontinuity in the bone surface outline (highlighted by the arrows). The location of the fracture (indicated by the yellow arrow) can be accurately visualized in all images. However, the 3D renditions may be used for a more complete assessment of the fracture as they appear to provide additional information related to the relative displacement and orientation between the two bone segments. This degree of image quality might prove valuable for the diagnosis of minimally displaced (‘hairline’) fractures, bony defects of various sizes, and for monitoring bony healing.

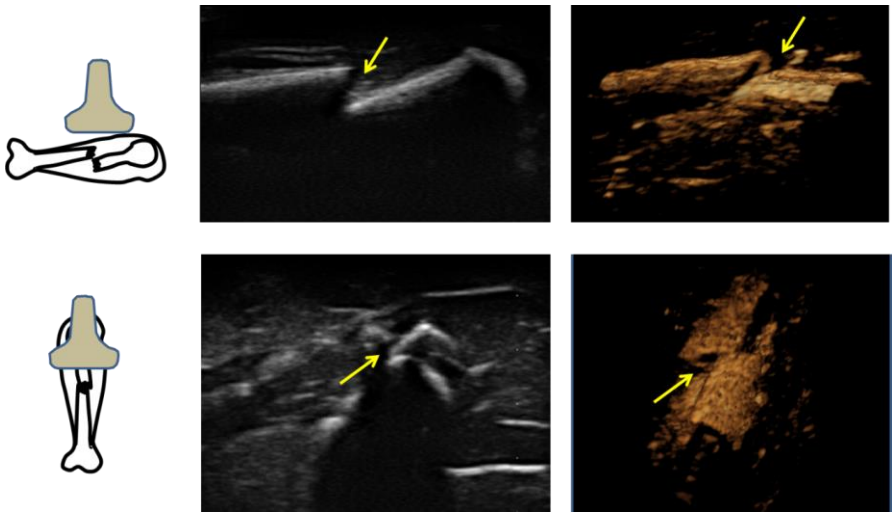

Figure 17. Typical results obtained from broken bone specimen (chicken) with minimal damage to the soft tissue. (a) B-mode image of the specimen (ROI = 2.5 x 3.8 cm^2). The fracture is visible as a discontinuity in the hyperechoic feature, as indicated with an arrow. This B-mode image is taken with the transducer parallel to the bone surface; (b) B-mode image of the same specimen taken with the transducer perpendicular to the bone surface; (c) and (d) 3D renditions of the sample containing the broken tibia. Arrows indicate the location of fracture.

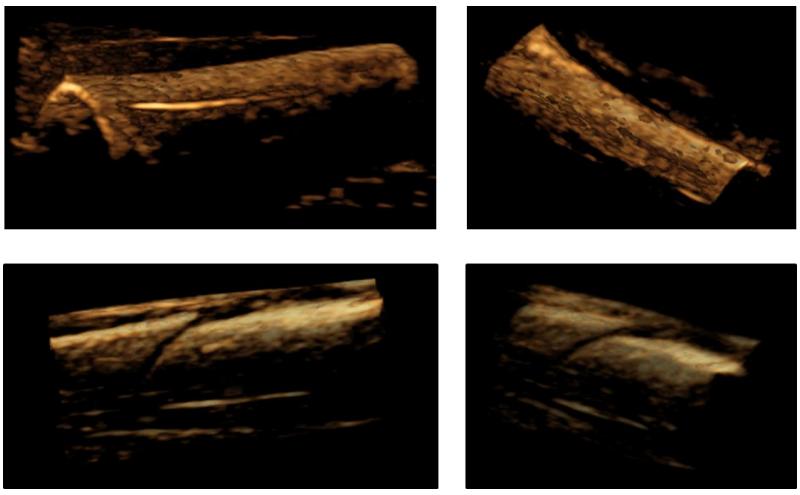

Figure 18. Typical results of ultrasound scans of intact and fractured rabbit tibias. Figure shows 3D renderings of ultrasound imaging results performed on (a) and (b) intact rabbit tibias, and (c) and (d) fractured rabbit tibias. In the latter cases, the fracture is clearly indicated by the arrows.

Figure 18 shows examples of 3D images obtained from mammalian (rabbit) specimens with an intact tibia (top row) and with a tibial fracture (bottom row).

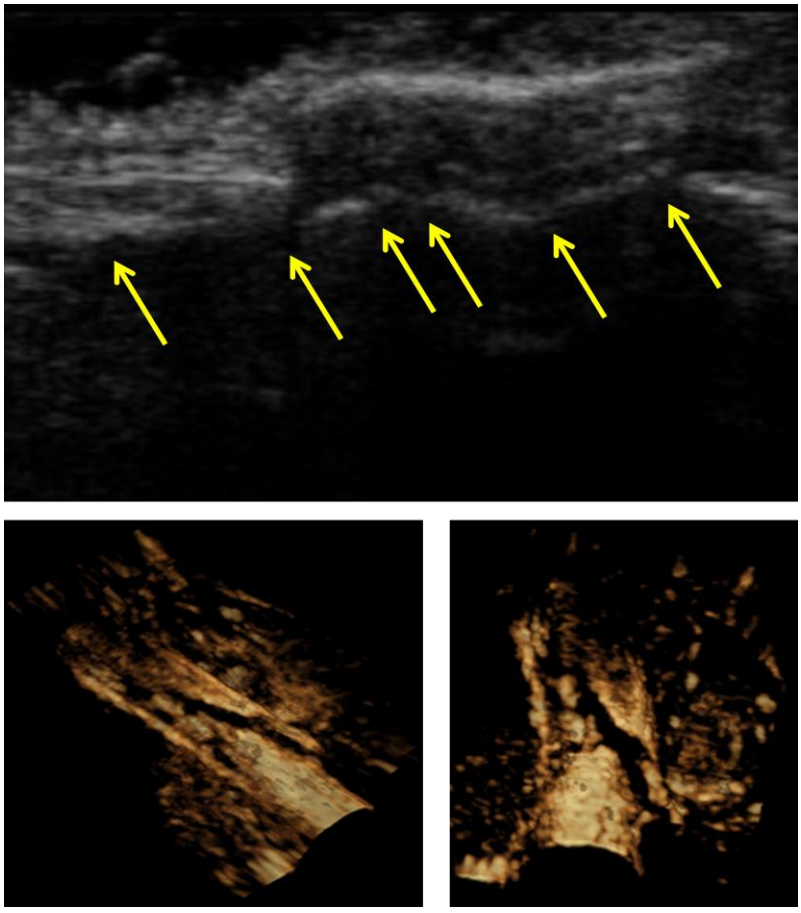

Figure 19. Results obtained from a chicken bone sample shattered in multiple fragments (inside the tissue). (top row) B-mode image (the arrows indicate bone fractures); (bottom row) 3D renditions visualizing the fragmented bone from different perspectives.

Figure 19 shows an example of ultrasonic imaging of a comminuted fracture in a chicken tibia. This type of fracture was induced in an intact tissue specimen by rapid application of a high external pressure. The figure shows a B-mode image of the

specimen (top row), where several fractures are visible (indicated by the arrows). The 3D renditions provide a more comprehensive view of the various bone fragments and their relative positions inside the soft tissue.

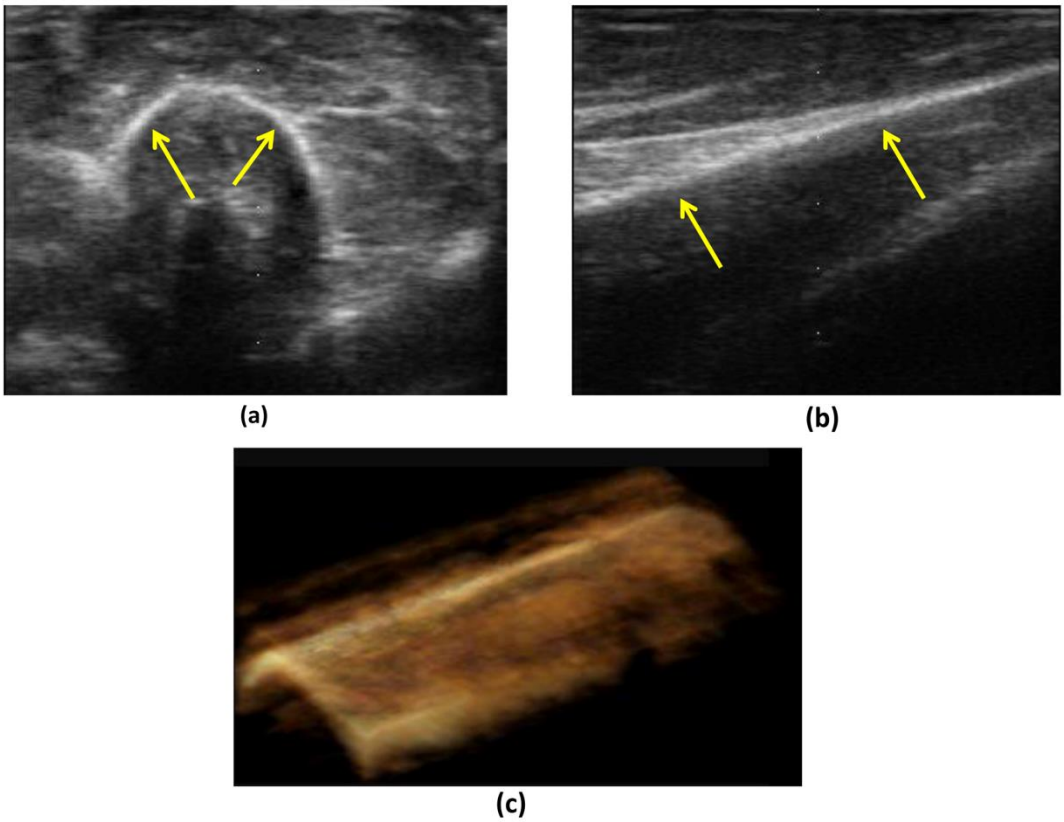

Figure 20. Typical ultrasound imaging results obtained from intact sheep tibia. Results include B-modes obtained with the transducer held (a) perpendicular and (b) parallel to the bone axis. (ROI = 4.0 x 3.8 cm^2). Arrows indicate the bone-soft tissue interface. (c) 3D rendition of the intact sheep tibia.

Figures 20 and 21 refer to data obtained from long bones in large animal specimens. Figure 20 shows two 2D views and a 3D rendition obtained from an intact sheep tibia. Figure 21, instead, shows 2D and 3D renditions obtained from canine tibias

before (left) and after (right) fracture. While the presence of skin and connective tissue surrounding the bone may make bone localization more complicated and reduce contrast, it is still possible to clearly visualize the bone surface and detect the eventual presence of a bone defect even with minimal image post-processing methods such as those used in this study.

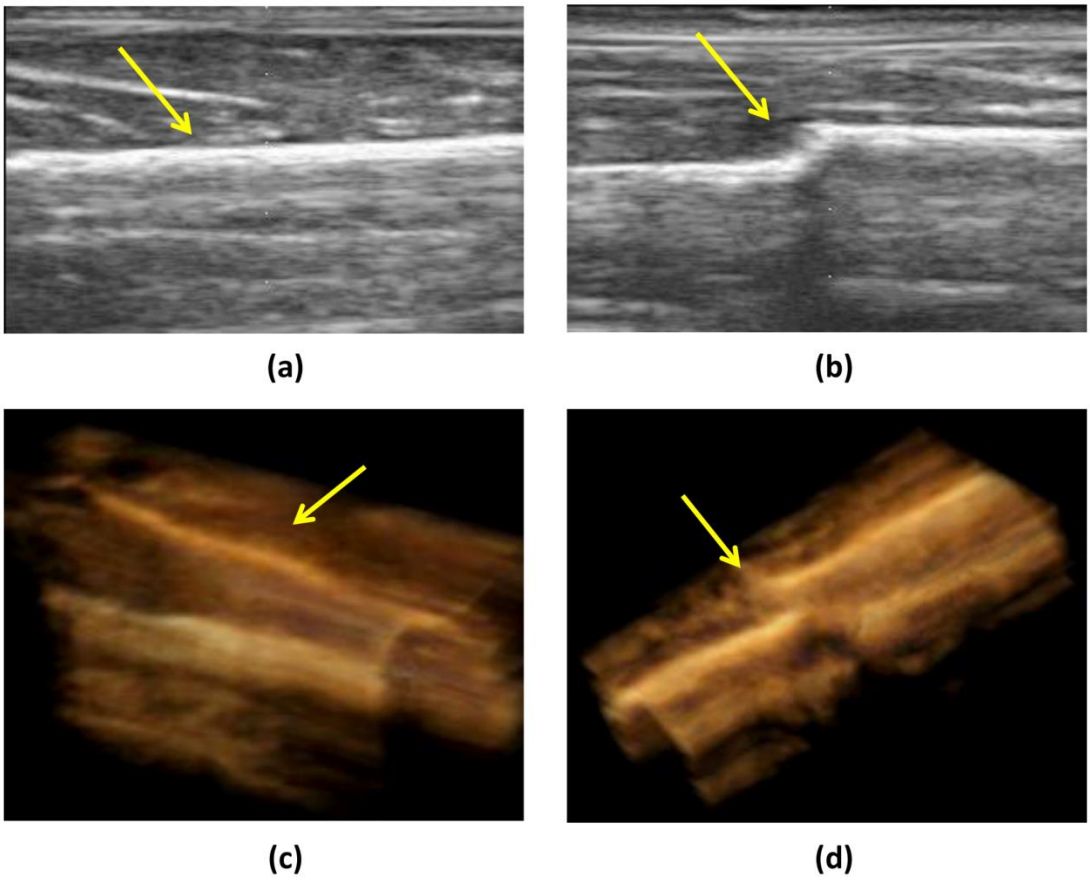

Figure 21. Typical 2D and 3D ultrasound imaging results of tibia specimens obtained from canine samples. Figure shows B-mode images of (a) intact and (b) fractured canine tibia samples. Figure (c) shows a 3D rendition of the intact tibia sample, whereas (d) shows the 3D rendition of a tibia sample containing a fracture. Note in figures (a) and (c) the presence of bright areas corresponding to the connective tissue surrounding the bone (the latter is highlighted by arrows). In figures (b) and (d), the location, size and shape of fracture can be clearly visualized (as indicated by the arrows).

While more complicated post-processing methods may be needed in these generally more complicated tissues, the ability to interact with the 3D volume and visualize the scans from different orientations and different cross sections can provide a better insight into the fracture and easier interpretation of the ultrasound findings.

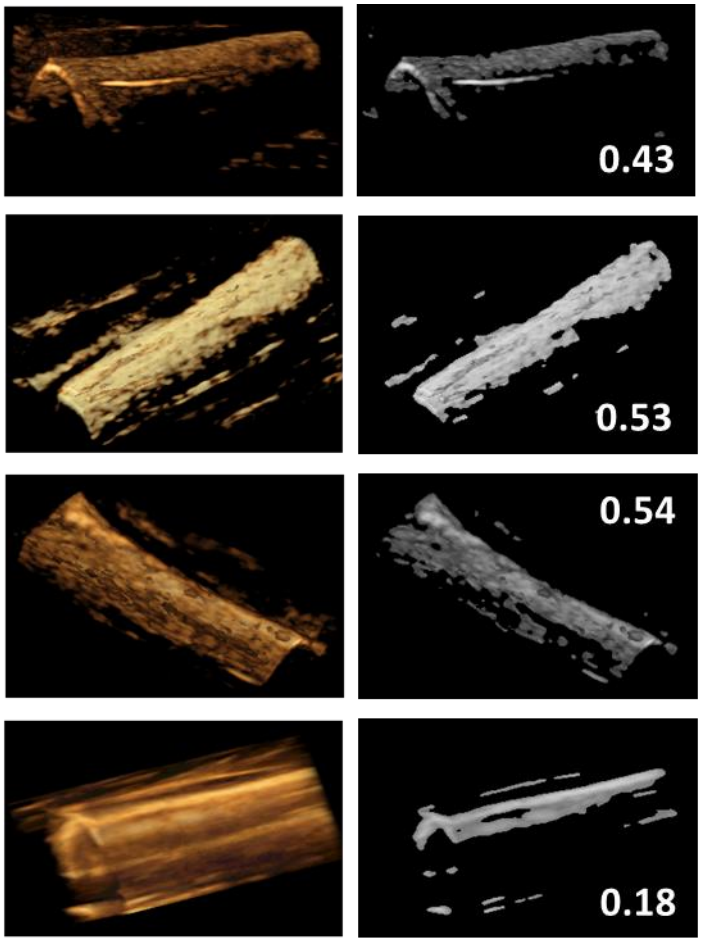

Figure 22. Post processing results of 3D ultrasounds of intact chicken and rabbit tibias. Selected results showing the effect of filtering and thresholding on 3D renditions of intact tibias obtained from chicken and rabbit samples. First column shows snapshots of the 3D renditions. Second column shows the corresponding images after filtering and thresholding. The number superimposed on these images show the ratio between the non-zero pixels in the thresholded image and the non-zero pixels in the original image.

Figures 22-26 show selected results of the statistical analysis carried out on the 3D ultrasound imaging results applied to various bones. Figures 22 and 23 refer to chicken/rabbit data - intact (figure 22) and fractured (figure 23) - while figures 24 and 25 refer to sheep/canine data - intact (figure 24) and fractured (figure 25). In each of these figures, the first column shows snapshots of the 3D renditions used for the analysis. The second column shows the same images after filtering and thresholding. The number superimposed in each of these images is the proportion of the non-zero pixels in the thresholded image with respect to the non-zero pixels in the original image (ratio number).

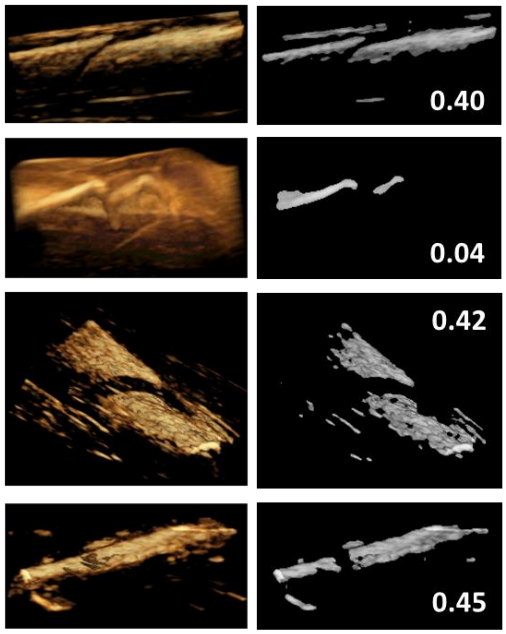

Figure 23. Post processing results of 3D ultrasounds of fractured chicken and rabbit tibias. Selected results showing the effect of filtering and thresholding on 3D renditions of fractured tibias obtained from chicken and rabbit samples. First column shows snapshots of the 3D renditions. Second column shows the corresponding images after filtering and thresholding.

We observe that, in the case of chicken and rabbit bones, the ratio number is typically above 0.4. In these cases, most of the soft tissue has been effectively eliminated by the post-processing on the 3D rendition. The bottom case in figure 22 and second one from the top in figure 23 show lower ratio numbers since a large amount of soft tissue is still present in these 3D renditions with intensity comparable to that of the bone, and the thresholding eliminates most of the soft tissue pixels but also most of the bone pixels. In the case of sheep/canine data (figures 24 and 25) the ratio numbers are typically lower than the chicken/rabbit because these bones are positioned deep into the tissue and their echogenicity is in many cases not significantly different than that of soft tissue.

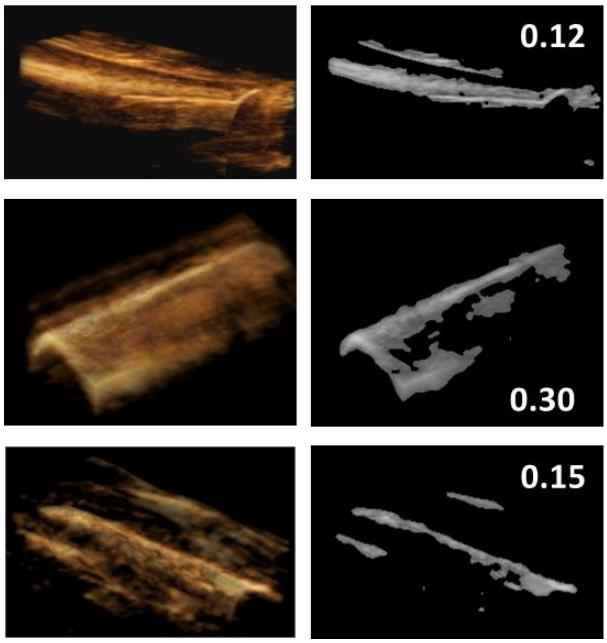

Figure 24. Post processing results of 3D ultrasounds of intact ovine and canine tibias. Selected results showing the effect of filtering and thresholding on 3D renditions of intact tibias obtained from sheep and canine samples. First column shows snapshots of the 3D renditions. Second column shows the corresponding images after filtering and thresholding.

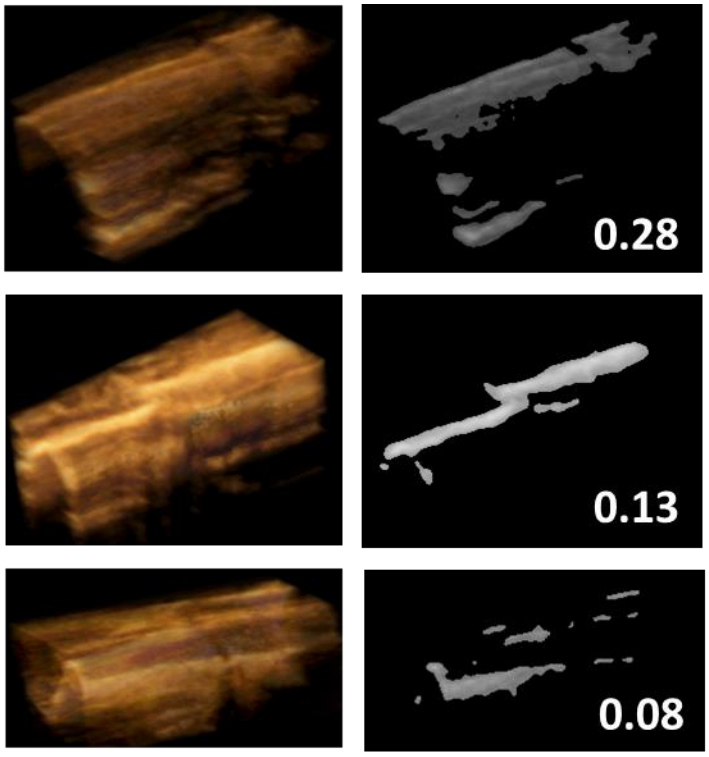

Figure 25. Post processing results of 3D ultrasounds of fractured ovine and canine tibias. Selected results showing the effect of filtering and thresholding on 3D renditions of fractured tibias obtained from sheep and canine samples. First column shows snapshots of the 3D renditions. Second column shows the corresponding images after filtering and thresholding.

In figure 26, we summarize all statistical results, by reporting the means and standard deviations of the ratio values in all analyzed cases for the various groups of tibias, based on species and integrity of the bone. As per this graph, the intact chicken and rabbit cases have the highest ratio numbers.

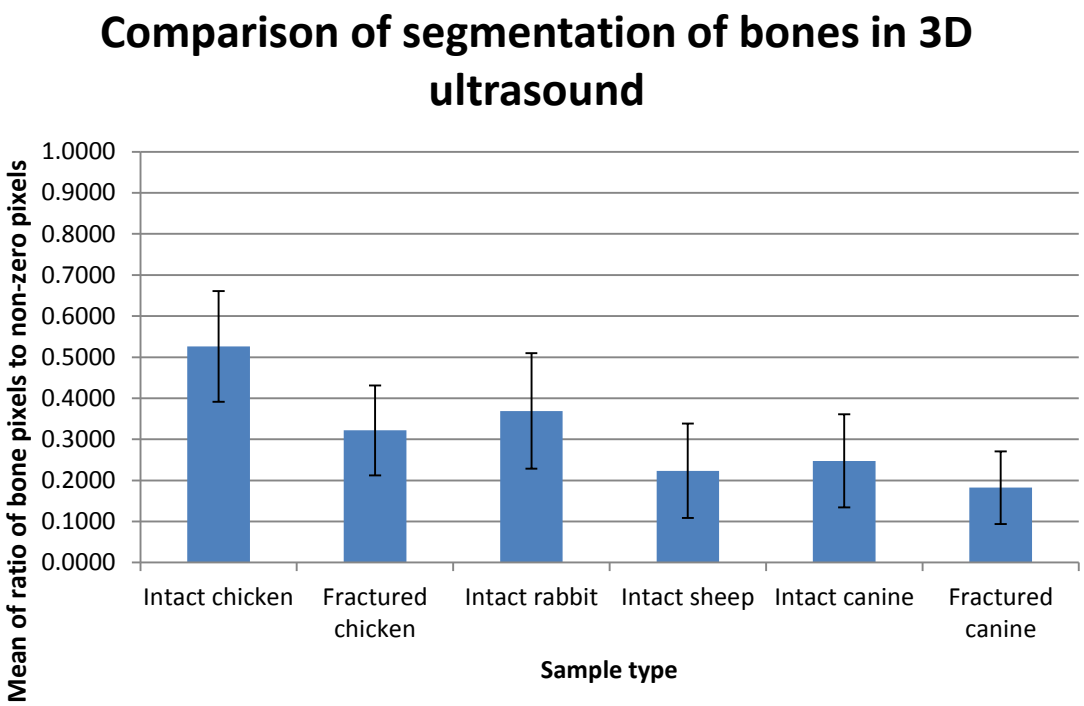

Figure 26. Statistical analysis of 3D ultrasound imaging results. Figure shows a comparison of means and standard deviations of the relative numbers of pixels pertaining to bone tissue in 3D ultrasound renditions obtained from intact and fractured tibias from various species of animals.

Discussion

The use of ultrasound imaging techniques for bone and fracture assessment is becoming an attractive complementary technique with respect to X-rays and CT imaging methods, particularly in light of the risks associated with radiation exposure (Smith-Blindman et al 2009, Berrington de Gonzalez et al 2009, Redberg 2009, Richards et al 2010, Redberg and Smith-Bindman 2014).

In this paper, we report preliminary results obtained using 3D ultrasound imaging techniques for characterizing different types of fractures and bony defects. From an

imaging point of view, the animal bones and soft-tissues provide significant insight into human bony pathology. Since this study focused on the visualization of bone surfaces using ultrasound and did not deal with the estimation of internal bone properties, the use of animal specimens was found to be appropriate and convenient due to their abundant availability.

The results reported in this paper suggest that ultrasound imaging techniques may have significant potential as a new, safe, cost-effective and real-time modality for bone imaging applications. Defects and fractures (and their characteristics) were demonstrated in the corresponding B-mode and 3D images. In general terms, it took about as much time to analyze the 3D ultrasound data as it takes to generate and analyze B-mode images in standard sonographic exams. While the exact number of scans performed in each case was not recorded, it took about 1-4 scans to generate acceptable 3D ultrasound renditions for each sample. In some cases, qualitatively "good" 3D renditions were obtained in the very first scan. Based on this preliminary study, the frequency requirements for ultrasound bone imaging techniques are the same as for any sonographic test. If the bone to be imaged is placed deep into the tissue, a lower frequency may be preferable. Ultimately, the success of the proposed methods depends on how clearly the bone surface is identifiable in the B-mode images used for the 3D reconstructions.

To our knowledge, the study reported in this paper is the first work that demonstrates the feasibility of 3D ultrasound imaging of bone surfaces given a wide variety of bone defects and fractures and spanning a wide range of surface constitutions.

These results demonstrate that it is technically feasible to generate 3D renditions of bone surfaces, fractures, and defects using standard diagnostic ultrasound scanners. In the presence of scattering or noise sources caused by the surrounding tissue, our study suggests that the use of post-processing imaging methods may be critical for proper 3D visualizations of bone surface and fractures. As for any medical imaging modality, caution should be exercised when applying post-processing imaging methods since use of these methods can considerably affect quality and performance of the resulting images. For this simple study, we applied modified intensity-slicing techniques that generalize thresholding methods, can be easily implemented and are computationally efficient and easy-to-use. We specifically avoided the use of very complex and computationally intense post-processing methods because we believe that these would be outside of the scope of a basic feasibility study. The fact that we were able to obtain high quality 3D renditions despite the noise caused by the presence of the surrounding tissue and the relative simplistic post-processing methods is a demonstration of the significant potentials that these imaging techniques may have to be easily and widely adopted. This is especially relevant considering that most modern clinical scanners are equipped to perform 3D and post-processing techniques similar to the ones used in our study. The statistical analysis carried out in this paper indicates that the intensity-slicing technique worked well in the case of chicken and rabbit tibias, whereas this simple post-processing approach alone was not sufficient to produce high quality results in the case of sheep and dog tibias. It should be noted that, even in the case of sheep and dog tibias, the bones and fractures were still generally identifiable in the corresponding 3D

renditions. However, the overall quality of these renditions was found to be lower than chicken/rabbit cases due to the presence of a relatively large amount of non-bone pixels in the 3D renditions (also reflected in the ratio numbers). We are, however, currently investigating the development of more advanced edge-enhancement optimization techniques that specifically target 3D ultrasound bone imaging applications and provide robust and automated 3D bone renditions at high frame rates. This would have significant implications, should these techniques be eventually applicable to humans.

The application of 3D ultrasound imaging techniques helped in the visualization of bone surfaces and allowed easier interpretation of the ultrasound results with respect to the case where 2D ultrasound imaging techniques alone are used. In general, the ability to interact with the reconstructed volume (such as rotating it around the various degrees of freedom) in order to optimize visualization is a great advantage over any 2D imaging modality (including plain x-rays). The high resolution and contrast of the 3D ultrasound renditions may allow for the retrieval of useful information (maximum point of displacement, translation and rotation between bone fragments), which may prove clinically useful for fracture alignment during closed reduction and for the monitoring of bony healing. Based on these preliminary results, the major advantages of ultrasound techniques with respect to x-rays for bone imaging applications may include: visualization of multiple scanning planes; 3D information in real-time; availability of structural information regarding both soft tissue, bone and soft tissue-bone interface; no radiation; and greater sensitivity to soft-tissue trauma.

Conclusions

This study suggests that ultrasound imaging techniques can be used to assess bone defects including a wide variety of fractures and controlled defects in real-time and with high contrast-to-noise ratio and resolution. Simple post-processing techniques available in most standard diagnostic ultrasound scanners are adequate to enhance the visualization of the bone surfaces, making it a versatile tool for use intra-operatively as well as in the field. In the future, ultrasound imaging techniques might provide a cost-effective and safe diagnostic complement to standard imaging methods currently used in bone applications.

4. ULTRASOUND ELASTOGRAPHY ASSESSMENT OF BONE/SOFT TISSUE INTERFACE

Introduction

Fractures of long bones make up a preponderance of orthopedic clinical cases and are the object of extensive clinical and laboratory investigations (Anonymous 2012; Chaar-Alvarez et al. 2011; Barata et al. 2011). In children, the most common fractures involve the long bones of the forearm shaft and of the tibial shaft (Cheng and Shen 1993). These injuries constitute a significant proportion of all non-fatal injuries reported on a global scale (Mock and Cherian 2008). Traditionally, the most common way to diagnose a fracture and to monitor bone regrowth is X-Ray imaging, and in some cases, computed tomography (CT) and magnetic resonance imaging (MRI) (Genant et al. 2008; Lang et al. 1998). However, ultrasound-based modalities have recently gained momentum by virtue of their ability to provide real-time diagnosis using portable and radiation-free imaging equipment. Recent studies suggest that it is possible to use 2D and 3D ultrasound techniques, which rely on the high acoustic impedance between bone and surrounding soft tissue, to assess controlled bone defects *in vitro* with high accuracy and contrast-to-noise ratio (Parmar et al. 2010). However, bone tissue differs from soft tissue not only in its acoustic properties (speed of sound, density, acoustic impedance and ultrasonic attenuation), but also with respect to the elastic properties.

The elastic modulus of intact bones can be up to 5-6 orders of magnitude higher than that of the surrounding soft tissue (Spatz et al. 1996). Furthermore, when long bones undergo fractures, the bone fragments might require realignment to aid the process of bone healing. In complicated closed fractures, parameters such as inter-fragmentary motion, bone alignment and rotation are optimized as a part of the process of anatomic reduction to produce stable fixation (Schatzker and Tile 2005). Once adequately stabilized, the process of bone regrowth is characterized by a progression of changes in the tissue at the fracture location through inflammation (reactive phase), followed by soft callus formation, progressive mineralization (reparative phase), and finally remodeling (Cruess and Dumont 1985). The soft tissue at the interface of the bone in the vicinity of the fracture becomes highly active and rich with nutrients to aid the healing process. The ability to monitor bone regrowth based on the changing stiffness of the soft tissue around the healing bone would provide valuable information regarding delayed unions and the need for further orthopedic intervention (Perren and Boitzy 1978; Protopappas et al. 2008). Unfortunately, the standard of care imaging techniques (radiographs) employed to assess fracture gaps and bone alignment as well as bone healing are either incapable of measuring tissue stiffness or are unreliable because of the significant inter-observer variability (Lovisetti and Bettella 2008). Ultrasound imaging represents an appealing alternative to X-Ray based imaging due to its sensitivity to variations in soft tissue elasticity.

The most commonly used ultrasound based approaches for the prediction of fracture risk in osteoporotic patients and for the monitoring of fracture healing are based

on quantitative ultrasound (QUS) techniques (Laugier and Haïat 2010). Recently, a through-transmission system was used to assess the early stages of bone regeneration in small-animal models of bone injury by generating 2D attenuation maps of the callus region (Rohrbach et al. 2013). However, these techniques are subjected to a number of challenges, including the lack of spatial and temporal specificity, the need for a water bath acquisition setup, limited resolution and lack of standardization among manufacturers (Laugier and Haïat 2010).

Ultrasound elastography provides an assessment of soft tissue abnormalities based on the presence of an underlying mechanical contrast between normal and abnormal tissues (Garra et al. 1997; Qiu et al. 2008). This technique involves acquiring ultrasound RF frames while applying an external quasi-static compression (0.5-5% strains) over the region of interest (ROI). Cross-correlation based algorithms are applied to compute tissue motion from the acquired frames, which is then presented in the form of "elastograms", i.e., maps of the distribution of strains in the ROI (Ophir et al. 1999). Using current state-of-the-art systems, it is possible to generate elastograms of diagnostic value with high signal-to-noise ratio and contrast-to-noise ratio as well as high spatial and temporal resolutions (Konofagou et al. 2002) thus providing real time information about the tissue of interest (Drakonaki et al. 2012). Various types of elastograms can be generated from the tissue under study, depending on the component of the tissue motion being estimated (Figure 27).

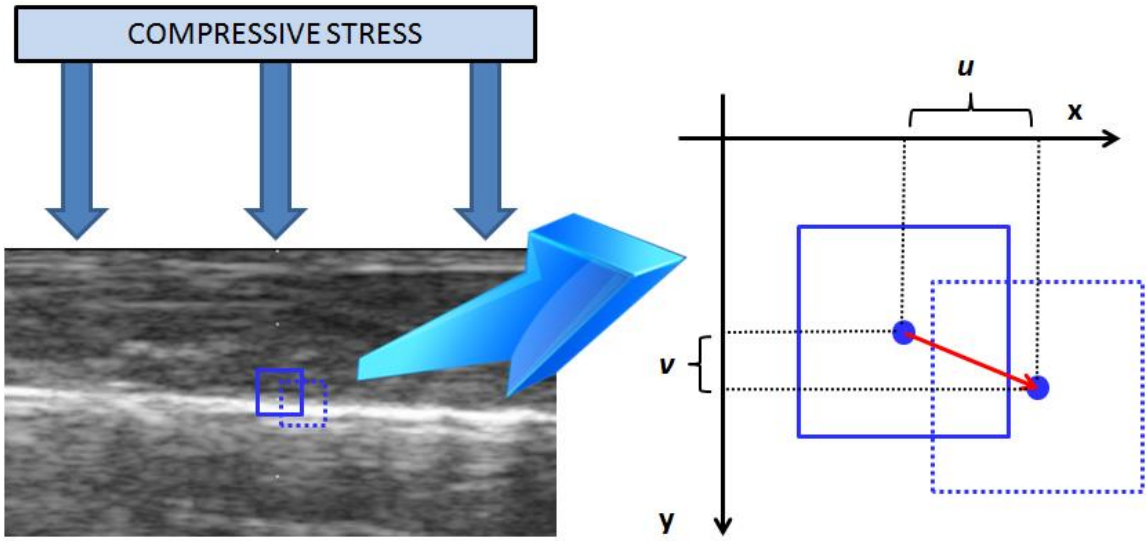

$$Axial\ strain = \frac{\partial u}{\partial x}, Lateral\ strain = \frac{\partial v}{\partial y}, Axial\ shear\ strain = \frac{\partial u}{\partial y}$$

Figure 27. Illustration depicting the result of applying a compressive stress on a tissue sample comprising of an intact bone. The displacement experienced by a segment of the tissue at the bone/soft tissue interface can be separated into an axial component and a lateral component. These respective displacements are used for computing various strain components.

Figure 27 shows the B-mode image of a tissue sample including a long bone (hyperechoic line) along with soft tissue (above the hyperechoic line) and subjected to compressive force. The solid and hatched boxes indicate the possible in-frame locations of a tissue sample at the bone/soft tissue interface before and after the compression is applied, respectively. The local axial and lateral displacements experienced by the tissue sample are computed, and expressions for axial strain, lateral strain and axial shear strain based on these displacement components are estimated. In practice, lateral strain estimation is known to be significantly noisier than axial strain estimation (Righetti et al.

2007) and hence is not used in the present study. Axial strain elastography has been clinically applied to monitor inflammation in tendons and muscles, malignant lesions and liver fibrosis (Pallwein et al. 2007; Konofagou et al. 2002; Cochlin et al. 2002; Garra et al. 1997; Kim et al. 2012; Ying et al. 2012; Thomas et al. 2006; Friedrich-Rust et al. 2007; Morikawa et al.; Drakonaki et al. 2012). Axial shear strain elastography (ASSE), on the other hand, helps with assessing the degree of connectedness between various tissues (Konofagou and Ophir 1998; Konofagou et al. 2000; Thitaikumar et al. 2007a). ASSE has been used to classify benign and malignant lesions in the breast (Thittai et al. 2011b; Thittai et al. 2011a; Xu et al. 2010) and may have potential application in the diagnosis of brain tumors (Chakraborty et al. 2012). Furthermore, it has been shown that the conditions for obtaining optimal axial strain elastograms (with respect to the axial strain signal-to-noise ratio (SNR_e) and axial strain contrast-to-noise (CNR_e) are also applicable to axial shear strain elastograms (with respect to axial shear strain (SNR_{asse}) and axial shear strain (CNR_{asse}) (Thitaikumar et al. 2007b).

When a compressive strain is applied to a region comprising soft tissue and bone, the soft tissue undergoes higher strains than the bone since the bone is significantly stiffer than the soft tissue. There is also experimental evidence suggesting that high shear strains are generated in the muscle adjacent to the bone when the body is exposed to localized compressive stress (Oomens et al. 2003). Consequently, depending on the degree and orientation of the applied compressive force with respect to the bone surface, on the morphology of the underlying musculoskeletal anatomy and on the biomechanics of the bone/soft tissue physical interaction, a variation on the sliding motion at the

bone/soft tissue interface may occur. The axial strain elastograms and axial shear strain elastograms have the potential to provide tools to monitor the changes in these mechanical properties, hence providing information regarding the presence of fractures, their severity as well as progress in the subsequent healing process.

In our preliminary work, we showed that, in principle, ultrasound elastography techniques can be used to detect changes in the axial strain and axial shear strain distributions at the bone/soft tissue interface before and after a non-union fracture of a chicken tibia (Parmar et al. 2009). This work, however, was very preliminary, was performed on a very limited data set and did not include any statistical analysis. In this paper, we report the results of a comprehensive *in vitro* ultrasound elastography experimental study performed on intact and fractured canine and ovine tibias with supporting statistical analysis. Elastograms of the local axial strain and axial shear strain at the bone/soft tissue interface were generated and analyzed in the case of intact and fractured bones. Statistical analyses of the image quality factors of the generated elastographic images in intact and fractured bones are then presented. The results indicate that the relative strength of the axial strain at the bone/soft tissue interface with respect to that in the background soft tissue reduce in the presence of a bone fracture. Additionally, the distribution of the normalized axial strain and axial shear strain at the interface tissue and the fracture fragments depends on the degree of misalignment, which might be indicative of the severity of the fracture.

Methods

Elastography experiments were performed on intact as well as fractured tibias *in vitro*. For this study, we used 2 samples of ovine tibias and 4 samples of canine tibias (multiple experiments were performed on each sample). These animal samples were provided to us by the Texas A&M Institute of Preclinical Studies (TIPS), where they were used for different studies. No animals were sacrificed specifically for the purpose of the present work.

The acquisitions were performed in a wide range of experimental conditions. The sheep samples procured for this study had the overlaying skin removed. This allowed for a surgical chisel to be used to induce a complete fracture in the sheep tibial shaft. The canine samples, instead, were provided to us with the skin intact. Hence, in order to maintain the integrity of the overlying skin and soft tissue over the bone and also to mimic real closed fracture scenarios as closely as possible, a commercially available variation of a Gigli saw was used to induce controlled fractures in these samples (Wardak and Wardak 2010). Since the same samples could be used for multiple experiments, the experiments on the canine samples resulted in 26 cases of intact tibia and 24 cases of fractured tibia. Similarly, the experiments on the sheep samples resulted in 8 cases of intact tibia and 2 cases of fractured tibia. However, statistical analysis could not be performed on the sheep samples due to an insufficient number of samples for significance. Therefore, the reported statistical analysis refers to the canine samples only. A summary of the experiments conducted in this study is presented in Table 5.

Ultrasound data were acquired using a 38-mm linear array transducer (Sonix RP, Ultrasonix, Richmond, BC, Canada) with a center frequency of 6.6MHz, bandwidth 5-14MHz and 1mm beamwidth at focus. RF data were acquired with the transducer held parallel to the axis of the bone mounted on a linear actuator that allowed for application of strains in a very controlled manner (up to 10% strains). A compressor plate was attached to the transducer face to guarantee uniform distribution of applied strain over a 40mm x 40mm area. Commercially available ultrasound gel was used as the coupling medium. For each experiment, 150 to 1200 RF frames were acquired from the area of interest.

Table 5. Summary of experiments conducted on canine and ovine tibias for this study.

Tibia type	Skin integrity	Fracture technique	Bone integrity	Number of cases
Canine	Intact	Gigli saw	Intact	24
			Fractured	30
Ovine	No skin	Surgical chisel	Intact	8
			Fractured	2

A cross-correlation based algorithm implemented via general-purpose computing on a graphical processing unit (GPGPU) was used to determine the displacements between pairs of pre- and post-compression frames (Yang et al. 2011). The window length was set to 1.5 mm and the overlap between consecutive windows was set to 80%. The least squares technique was then used to obtain axial strain and axial shear strain

elastograms from the corresponding displacement maps (Sambasubramanian 2011). The axial strain elastograms are computed as the gradient of the axial displacements in the axial direction, whereas the axial shear strain elastograms are computed as the gradient of the axial displacements along the lateral direction. Additionally, a multicompression technique (Konofagou et al. 1997) was used to optimize the SNR in the final elastograms. According to this technique, the SNR_e is improved when the compressive force is applied in stages and a number of elastograms are averaged. For the current study, this technique was modified to compensate for variations in applied strain rates by dynamically choosing pre- and post-compression frames separated apart by a constant value of applied strain. This technique allows us to be in the region of the strain filter corresponding to high SNR_e while maintaining high correlation values between pre- and post-compression frames (Varghese and Ophir 1997). The mean correlation map, axial elastograms and axial shear strain elastograms were then computed as a mean of the individual frames obtained in the previous step.

Next, statistical analysis was carried out to quantify the signal strength parameters in the resulting axial strain and axial shear strain elastograms in order to assess the quality of the elastography results. The image quality parameters analyzed were the signal-to-noise ratio (SNR) and contrast-to-noise ratio (CNR) as determined using the following equations, which are applicable to both axial strain elastograms and axial shear strain elastograms (Thitaikumar et al. 2007b; Varghese and Ophir 1998):

$$SNR = \frac{\hat{s}_t}{\hat{\sigma}_t} \text{ and } CNR = \frac{2(\hat{s}_t - \hat{s}_b)^2}{\hat{\sigma}_t^2 + \hat{\sigma}_b^2}$$

Here, $\hat{s}_t$ and $\hat{\sigma}_t$ refer to the mean strain and standard deviation of the strain in the "target" region. In addition to these parameters, the CNR depends on $\hat{s}_b$ and $\hat{\sigma}_b$, the mean and standard deviations of the strains in the "background". In the case of the axial strain data, the soft tissue/bone interface was designated as the target region of analysis, and the soft tissue far away from the bone as the background. Regions comprising of relatively uniform axial strains were manually selected from two areas in each axial strain elastogram – within the background soft tissue above the bone and at the bone/soft tissue interface. In order to compare results across different experiments, the strains were normalized with respect to the applied strain. The applied strain was estimated by applying cross correlation to each pair of A-lines in the first and last frames for each experiment, and tabulating the displacements corresponding to the maximum correlation coefficient for each pair of A-lines. The median displacement value was automatically selected and divided by the depth of acquisition for the experiment to determine the applied axial strain.

In the case of axial shear strain elastograms, however, the designation of target and background regions was not as straightforward as in the axial strain case. In (Thitaikumar et al. 2007b), the authors empirically chose the background to be a uniform strain region deep within the lesion. In our case, we could not choose a similar region below the bone surface as the background since the ultrasound signal is quickly attenuated below the bone surface, and the signal obtained from a region deep beneath the bone (> ~10 wavelengths) might not be reliable. On the other hand, a region in the soft tissue above the bone surface undergoes lower axial shear strains as compared to a

region close to the bone. Hence, this region was chosen as the background for the present study. In order to be able to compare the above signal strength parameters across different experiments, the axial shear strain elastogram obtained in each experiment was first normalized with respect to the mean axial strain in the background soft tissue (as defined in the previous paragraph). This allowed for minimization of the variation in the axial shear strain patterns due to variations in magnitude of applied strain. Next, the axial shear strain elastograms were cropped so that the strain patterns originating due to anatomical features other than the bone/soft tissue interface (such as connective tissue, fat/muscle interfaces etc.) were eliminated from the analysis. To ensure this, areas at a distance greater than two wavelengths from the bone surface were masked out so that the analysis was restricted to the bone/soft tissue interface. Care was also taken to see that the ROI did not overlap with the near field region of the transducer, especially in the cases of shallow depths of acquisition. Finally, a threshold was applied so as to demarcate the regions close to the bone surface (to within about ±0.5 cm), and all pixels with absolute value of axial shear strains below this threshold were masked out. The selection criteria for the threshold involved eliminating features in the elastogram that did not belong to the bone/soft tissue interface, while retaining as many pixels that were spatially distributed across the complete bone surface as possible for an unbiased statistical analysis. Formally, a threshold value of about 35±5% of the maximum axial shear strain value in the bone/soft tissue interface region was found to retain a minimum of about 50 pixels in the elastogram, hence ensuring statistical significance. This process was applied separately to regions of positive and negative axial shear strains in the case

of experiments involving a fractured bone. The statistical parameters were then computed from each of the regions defined by the threcshold (in the positive and negative directions), and used to obtain values for the SNR_{asse} and the CNR_{asse}.

Results

The results section is divided as follows. First, we report correlation maps, axial strain elastograms and axial shear strain elastograms of bone/soft tissue interfaces in tissue samples containing intact tibiae and subjected to a compressive axial strain. Next, we show the changes observed in these elastograms in the presence of a fracture. Finally, the quality of these elastograms (intact and fractured) is statistically analyzed.

The number of frames averaged to generate the elastograms for the present study ranged between 27 and 250. Figures 28 and 3 show typical elastographic images obtained from the experiments conducted on an intact canine tibia and an intact ovine tibia, respectively. Figures 28(a) and 29(a) are the B-mode images corresponding to the pre-compressed state of the elastography experiments. Also shown are the typical mean correlation maps (figures 28(b) and 29(b)), mean axial strain (figures 28(c) and 29(c)) and mean axial shear strain elastograms (figures 28(d) and 29(d)) from the same plane. The bone surface is clearly visible in the B-mode image as a hyperechoic line (Parmar et al. 2010), due to the large impedance mismatch seen by the ultrasound beam at the bone/soft tissue interface. The various elastographic images are explained in the following sections.

Correlation maps

Figures 28(b) and 29(b) show the mean correlation maps for the planes of observation visualized in the corresponding B-mode images in figures 28(a) and 3(a) respectively. The dynamic range of correlation coefficients has been adjusted to enhance visualization of the high correlation regions (generally in the range 0.8-1) and suppress the correlation regions below 0.8.

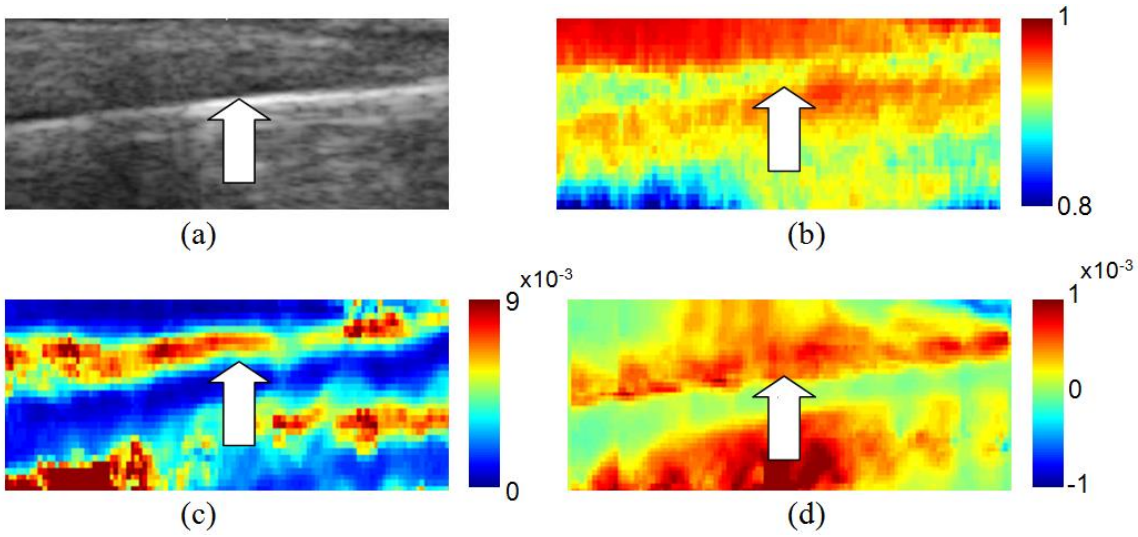

Figure 28. Ultrasound images obtained from an intact canine tibia. (a) B-mode image (b) Correlation map (c) Axial strain elastogram (d) Axial shear strain elastogram. The image depth is about 1.5 cm. The arrows indicate the location of the bone/soft tissue interface in each of the images.

From the results obtained on all experiments performed in this study, the mean correlation maps appear to consistently show the following noticeable features. First, the regions corresponding to soft tissue above the surface of the bone show relatively high correlation (corr. coeff. > 0.8). As expected, deeper regions below the bone surface

(distance from bone surface > ~10 wavelengths) show consistently low correlation due to the reflection of most of the ultrasound beam at the bone/soft tissue interface.

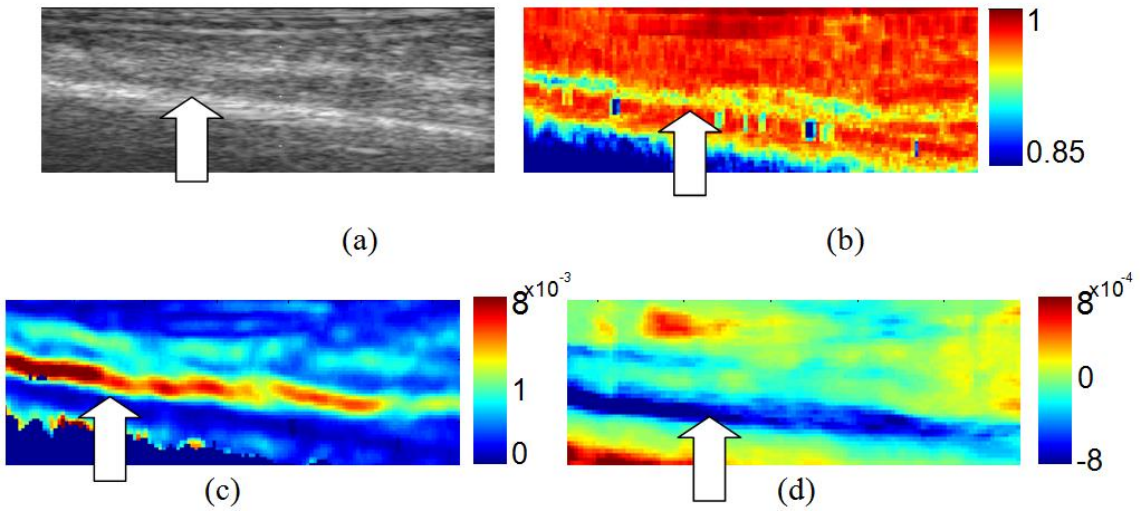

Figure 29. Ultrasound images obtained from an intact sheep tibia. (a) B-mode image (b) Correlation map (c) Axial strain elastogram (d) Axial shear strain elastogram. The image depth is about 1.5 cm. The arrows indicate the location of the bone/soft tissue interface in each of the images.

Second, the bone/soft tissue interface is generally observed to be associated with correlation values higher than those of the surrounding soft tissues (light arrows in the correlation maps of figure 28(b)). Similarly, connective tissue can also show up as a high correlation feature in the correlation maps. In some cases (9/24 cases of intact tibia and 16/30 cases of fractured tibia), patches of significantly decorrelated pixels were also observed immediately below the bone/soft tissue interface (visible in figure 28(b)) as well as in the connective tissue. In such cases, the patch was at least 5 pixels in the axial direction, which correspond to one cross-correlation window length used in processing

the data in this study. Overall, out of the 54 cases analyzed, the soft tissue/bone interface was clearly distinguishable in 51 cases (23/24 intact and 28/30 fractured) in the correlation coefficient maps on the basis of these features, thus indicating that these maps might contain usable structural information.

Axial strain elastograms

Figures 28(c) and 29(c) show the mean axial strain elastograms of samples containing intact tibias. The blue areas in the elastograms correspond to regions experiencing lower strains, whereas red areas correspond to regions experiencing higher strains. Only the pixels having a correlation above 0.8 are shown in the axial strain elastograms. A visual comparison of the B-mode image and the axial strain elastogram indicates that the regions of low strains correspond well with the bone surface, and the higher strains above correspond well with the soft tissue above the bone. In our experiments, we observed high axial strain concentrations in the region immediately above the bone surface, which probably occur as a consequence of boundary conditions. Such strain concentrations are typically observed at the interface between two media with a relative large difference in elastic moduli (Chaudhry 2012; Thitaikumar and Ophir 2007). Based on our experiments, the axial strain elastograms of intact bone samples consistently showed the following characteristics: very low strains immediately below the bone surface, very high strains at the bone/soft tissue interface and high strains in the background soft tissue (but typically lower than at the interface).

Axial shear strain elastograms

Figures 28(d) and 29(d) show the distribution of the mean axial shear strains experienced in the ROI. In these elastograms, the blue and red regions correspond to areas undergoing relative motion in laterally opposite directions within the plane of observation, whereas the green regions correspond to areas that undergo minimal (or close to zero) motion. Based on our experimental results, the areas of zero axial shear strains found just below areas that undergo high axial shear strain identify the bone/soft tissue interface. The high strain regions just above the bone surface indicate unidirectional sliding motion of the soft tissue over the bone surface upon application of a compressive force which has a non-zero shearing component with respect to the bone axis. Another important observation is that such distinct sliding motion is not expected between layers of soft tissue separated by connective tissue due to the fact that the axial shear strain contrast is related to the underlying stiffness contrast and there is a much larger difference in the stiffness of the bone and surrounding soft tissue than between different soft tissues layers. This is clearly represented in figure 29(d) wherein the visibility of connective tissues is largely reduced.

The series of images in figures 30(a)-(f) show the results of superimposing axial shear strain data over corresponding B-mode images obtained from ovine (30a, c and e) and canine tibias (30b, d, and f). Figures 30(a) and 30(b) show the binary mask obtained upon applying a threshold to the axial shear strain elastograms, and figures 30(c) and 30(d) respectively show the corresponding axial shear strain pattern within the thresholded areas.

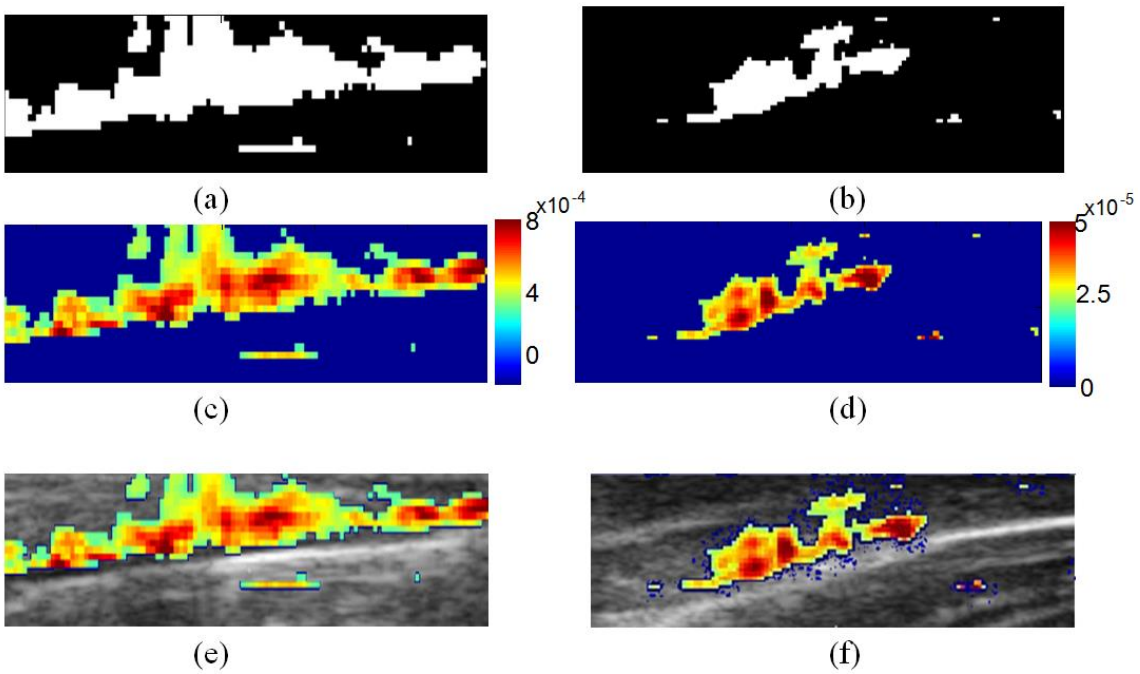

Figure 30. Results of thresholding analysis applied axial shear strain elastograms of intact tibias. The left column corresponds to the canine case shown in figure 28. The right column corresponds to an ovine case. (a) Binary mask obtained by applying a threshold on a cropped version of the axial shear strain elastogram shown in figure 28(d) (c) Distribution of the axial shear strain in the region demarcated by the mask in (a). (e) Composite image obtained by superimposing the axial shear strain elastogram in figure (c) over corresponding B-mode image in figure 28(a). Figures 30(b), (d) and (f) are the corresponding results obtained from a sheep case.

In most of the cases analyzed, the bone/soft tissue interface served as a "natural" landmark for the thresholding process, with the axial shear strain values falling off below the threshold as we go further from the interface in the axial direction. Figures 30(e) and 30(f) are composite images obtained by overlaying registered axial shear strain images over the corresponding B-mode images. As for the axial strain case, the highest values of axial shear strains were found at the bone/soft tissue interfaces, showing that

these elastograms may provide structural and possibly functional information about the bone/soft tissue interface.

Intact vs. fractured bone samples

Figure 31 shows a typical set of results obtained from a fractured canine bone. Figure 31(a) shows the B-mode image. The corresponding correlation map is shown in figure 31(b). The arrows indicate the location of the fracture in each of the images. The potential of correlation maps to represent bone structural information was clearly demonstrated by this experiment in which the two segments of the bone were separated by a gap representing a fracture. The region beneath the bone surface was characterized by consistently low correlation values compared to the surrounding soft tissue. Additionally, in each of the 30 fractured cases analyzed here, the region immediately below the fracture was observed to have an increase in the signal decorrelation relative to the regions beneath the bone fragments. It was possible to locate this region by plotting the correlation map using an appropriate dynamic range (0.8-1 in all cases for this paper). This information could one day be incorporated into bone surface segmentation algorithms to facilitate the automatic detection of the bone surface in ultrasound images.

Figures 31(c) and 31(d) represent the corresponding axial strain elastogram and the axial shear strain elastogram. The bone fragments manifest as two distinct regions of low axial strains. As in the intact case, higher strain concentrations are observable immediately above the bone/soft tissue interface.

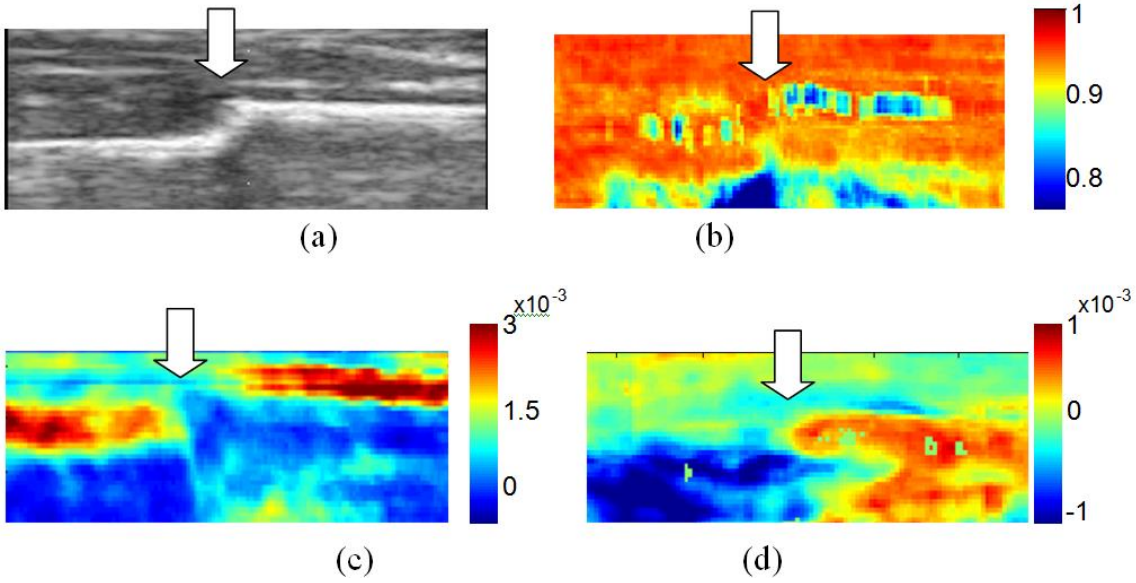

Figure 31. Ultrasound images obtained from a fractured canine tibia. (a) B-mode image (b) Correlation map (c) Axial strain elastogram (d) Axial shear strain elastogram. The arrow indicates the location of the fracture.

Among the images analyzed, the axial shear strain elastogram was the one that displayed the most noticeable changes before and after the fracture. While in the intact bone cases, the distribution of the axial shear strains in proximity of the bone indicated unidirectional sliding of the soft tissue over the bone surface when the tissue is subjected to an external compressive strain, in the fractured bone case, there were distinct regions experiencing opposing axial shear strains. This would indicate that these regions in the soft tissue on either side of the fracture location experienced sliding motion in laterally opposite directions.

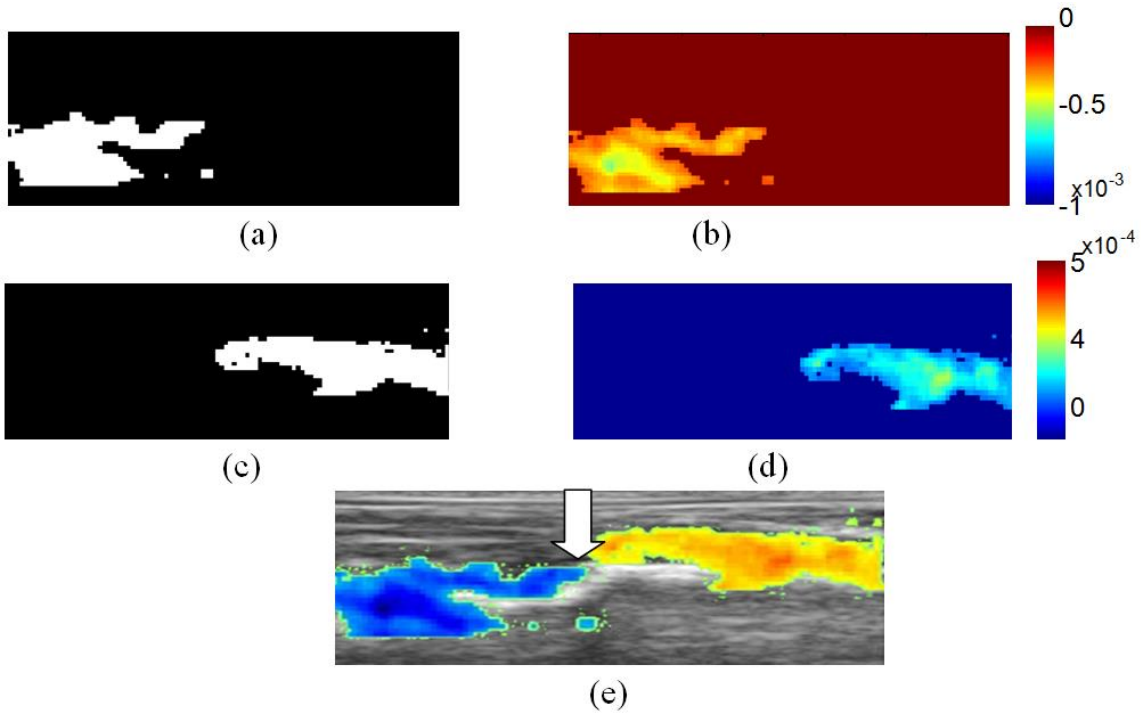

Figure 32. Results of thresholding analysis applied axial shear strain elastograms of fractured tibias (a) Binary mask obtained by applying a threshold to the negative strain region in the axial shear strain elastogram shown in figure 31(d). (b) Distribution of the axial shear strain in the region demarcated in the mask shown in (a). (c) Binary mask obtained by applying a threshold to the positive strain region in the axial shear strain elastogram shown in figure 31(d). (d) Distribution of the axial shear strain in the region demarcated in the mask shown in (c). (e) Composite image formed by superimposing the axial shear strain elastogram in figures (b) and (d) over the corresponding B-mode image in figure 31(a).

As in the case of the intact bones, we created masks to perform statistical analyses on the ASSEs. For each case analyzed, two masks were created - one for the positive and one for the negative strain regions. Figure 32(a) corresponds to the mask obtained from the region near the bone surface experiencing negative strains, whereas figure 32(b) shows the distribution of the axial shear strain within the masked region.

Similarly, figure 32(c) shows the mask obtained from the region near the bone surface experiencing positive axial shear strain, with the actual distribution of the strain itself shown in figure 32(d). Finally, figure 32(e) shows a composite image created by superimposing the axial shear strain data over the corresponding B-mode image.

From an analysis of the binary mask results, it appears that the physical separation between the positive and negative regions of axial shear strain might be indicative of the degree of separation between the bone fragments and their relative mobility. Fractures in which the fragments were significantly dislocated (such as in complete fractures, for example) were observed to have the positive and negative axial shear strain regions separated by a narrow region of zero sliding motion. On the other hand, samples mimicking incomplete fractures (where only a portion of the cortical bone was fractured) displayed a wider gap between the two regions in the ASSE, indicative of the low displacement between the two fragments (Hosalkar et al. 2009). Figure 33 shows two examples demonstrating this phenomenon. The top row shows an incomplete fracture while the bottom row shows a complete fracture. Each row displays (from L to R) the B-mode image of the region, the corresponding ASSE, a binary mask of the region containing the fracture and pixels from the neighboring area containing non-zero axial shear strain on either side of the fracture and the results of a region filling algorithm applied to the binary mask (Gonzalez 2008). A mean separation value between the bone fragments was obtained from the filled region by dividing the number of filled pixels with the height of the cropped image.

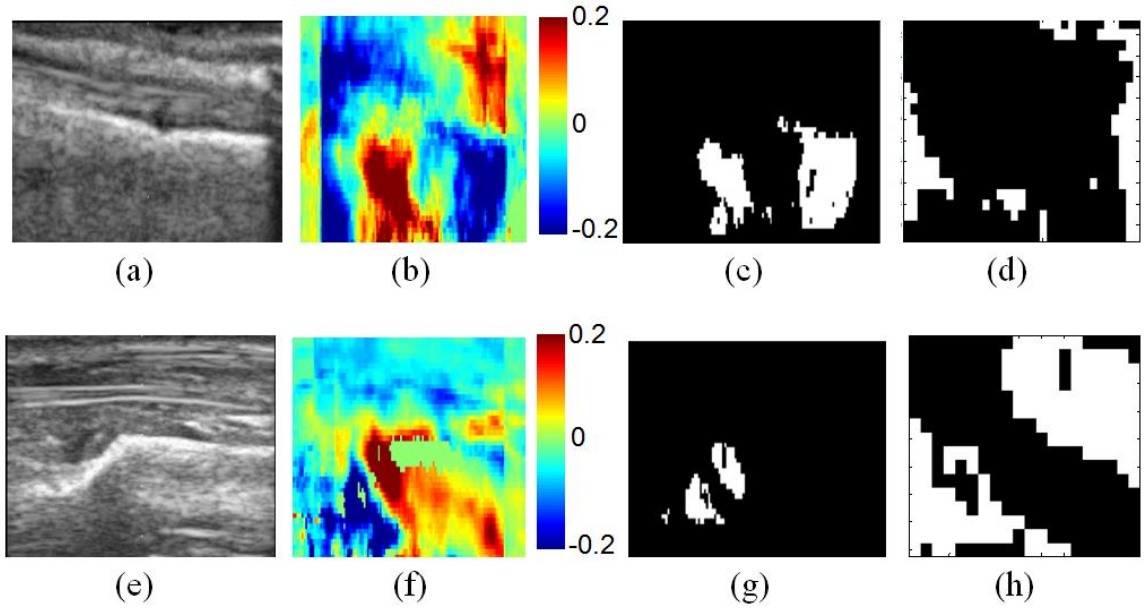

Figure 33. Ultrasound images obtained from separation analysis of axial shear strain elastograms obtained from fractured canine tibia samples (a) B-mode image. (b) corresponding axial shear strain elastogram. (c) Binary mask obtained from (b). (d) Results of region growing algorithm applied on a cropped region around the fracture in (c). Similarly, (e), (f), (g) and (h) show the same sequence of images as the first row just applied to a different sample.

It appears evident from these two examples that as the separation between the bone fragments increased, the corresponding axial shear strain distribution was more localized at the fracture's site. Six cases each from complete and incomplete fractures were analyzed for this purpose, and the result of this analysis is shown in figure 34. The mean separation (in pixels) between the positive and negative regions was plotted against the physical separation of the fragments (in mm), as measured from the corresponding B-mode images. The graph shows a clustering of the data points from the incomplete fractures and a clear separation from the data obtained from the complete fractures. This suggested an inverse correlation between the separation of the fracture

fragments and that of the ASSE regions undergoing strains in opposite directions. The results seem to be consistent with the findings in Thitaikumar et al. where lesions that are loosely bonded with the background tissue have lesser separation between regions of opposite axial shear strain compared to those where the lesion is more firmly bonded (Thitaikumar et al. 2007a). The loosely bonded lesions may be considered 'similar' to a fracture case where the fragments are dislocated to a higher degree in our analysis.

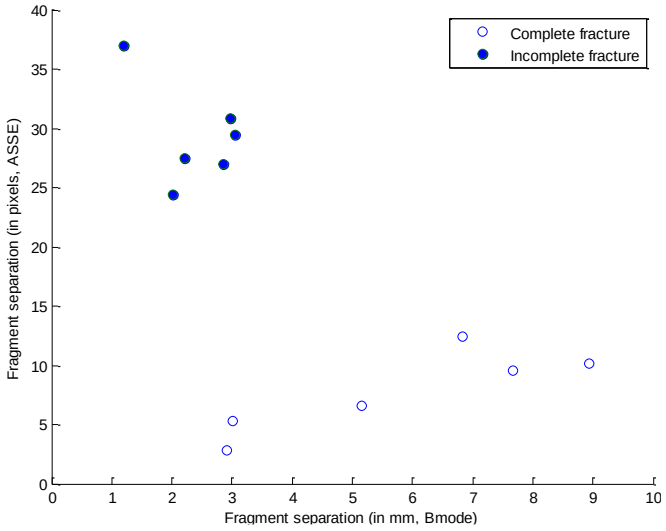

Figure 34. Distribution of the mean separation distance between the positive and negative axial shear strain regions (Y-axis) in fractured canine tibias compared to the corresponding distances measured using the B-mode images (X-axis). The measurements are marked as coming from samples containing a complete fracture or from an incomplete fractured sample.

Quality analysis of the elastograms

Axial strain elastograms

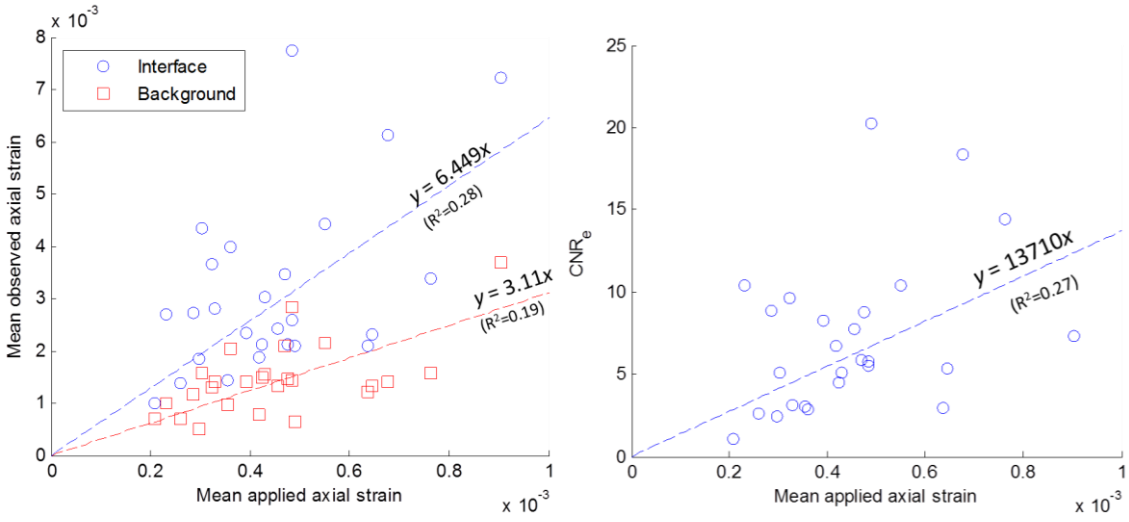

(a) (b)

Figure 35. Results of statistical analysis of axial strain elastograms obtained from intact tibias. (a) Distribution of mean axial strain values as a function of the applied strain in two regions in samples with intact tibias: at the bone/soft tissue interface (red line) and in the background soft tissue (blue line) for a total of 26 cases. Note the significantly higher axial strain values at the soft tissue/bone interface due to the strain concentrations created by the boundary conditions. Dashed lines indicate the corresponding linear curve fits. (b) Distribution of CNR_es of axial strains at the bone/soft tissue interface with respect to applied strain. Dashed line indicates the corresponding linear curve fit.

A statistical analysis of the axial strain elastograms was carried out using the data acquired before and after inducing a fracture in the canine limbs. The variation in the distribution of the mean axial strains at the bone/soft tissue interface and in the background in the intact cases with respect to applied strain in 26 cases is shown in Figure 35(a). Typically, the observed axial strains in these two regions are higher than

the applied strains (since the bone undergoes very low strains). Furthermore, the mean axial strains at the bone/soft tissue interface are higher than those in the background, and also increase linearly at a higher rate than the mean axial strains in the background with respect to increase in mean applied strain. The CNR_e between the axial strains in the two regions show fairly large values and slightly increases with respect to applied axial strain (Figure 35(b)).

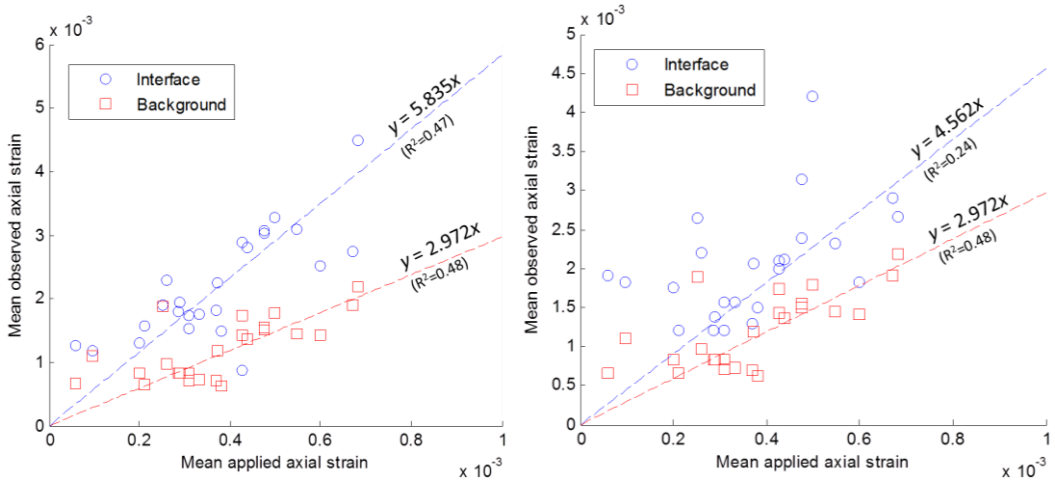

(a) (b)

Figure 36. Results of statistical analysis of axial strain elastograms obtained from fractured tibias. Distribution of mean axial strain values in two regions in samples containing fractured tibias: at the bone/soft tissue interface and in the background soft tissue (24 cases). Dashed lines indicate the corresponding linear curve fits in (a) the high fragments and (b) corresponding low fragment. Refer text for definition of "high fragments" and "low fragments".

For the analysis of the fractured samples, the fragments in each case were classified as being either higher within the frame (shallow depth from transducer face) or lower (deeper with respect to the transducer face). Interface regions were defined

separately for the two fragments, whereas the background was defined as the common area in the soft tissue further away from the two interface regions. An analysis of the axial strains in the interface regions and the background in 24 cases involving fractured bones indicate increasing trends with respect to increasing applied strain, as in the case of intact bones (Figures 36(a) and (b)). However, the CNR_es in the fractured case did not show a definite trend with respect to the applied strain. A comparison of the axial strains at the interfaces above the higher of the two fragments with respect to those above the lower fragment, the ratio of which is shown in Figure 37, shows that the mean axial strains in the former case are typically higher than the latter (18 out of 24 cases). This indicates that the applied strain may be unevenly distributed over the two fragments, with the interface tissue above the higher fragment typically demonstrating higher strains than that over the lower fragment. This is also evident from the variations in the slopes of the linear curve fits in Figures 36(a) and (b) (5.8 in the higher fragments vs. 4.6 in the lower fragments).

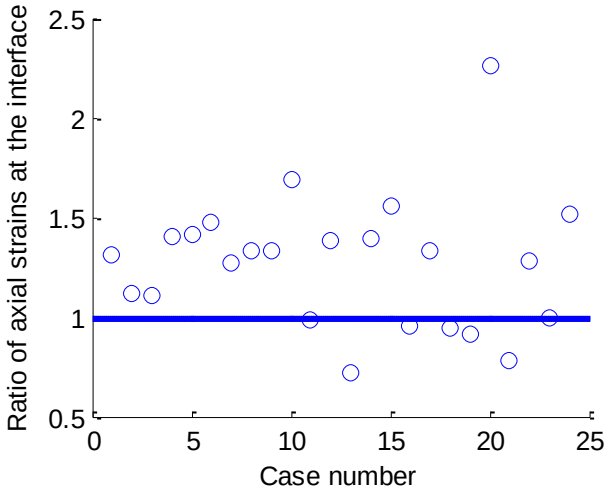

Figure 37. Distribution of the ratio between mean axial strains at the bone/soft tissue interfaces of high fragments and low fragments.

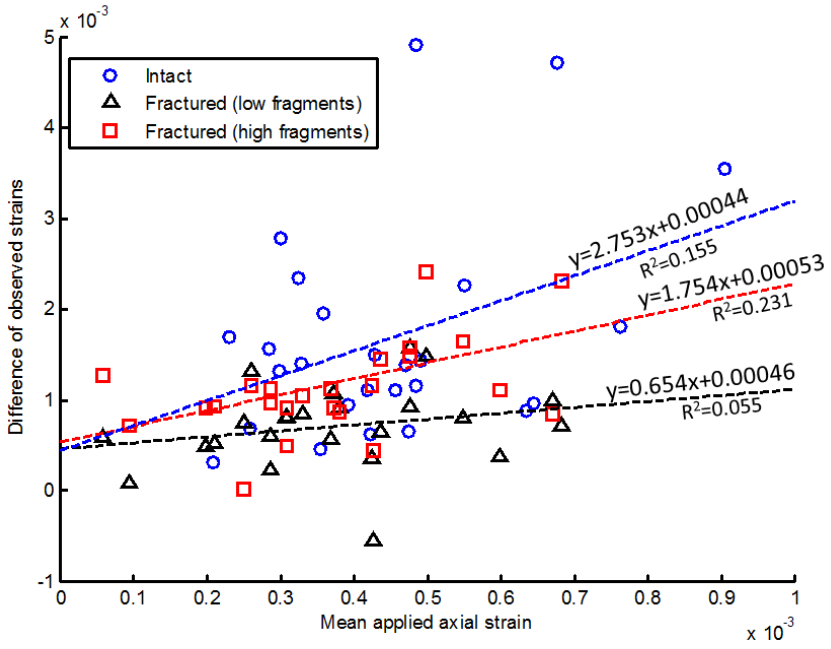

Figure 38. Comparison of the distribution of difference in axial strains at the bone/soft tissue interface and those in the background soft tissue in 3 cases: intact bones, fractured bones (high fragments) and fractured bones (low fragments). Also indicated are the linear curve fits for these distributions.

Figure 38 depicts the variation of the difference in the observed axial strains at the bone-soft tissue interface with respect to that in the background soft tissue in three different scenarios – intact, fractured (high fragment) and fractured (low fragment) – with respect to applied axial strain. The linear curve fits show a reduction in axial strains at the bone-soft tissue interface (of both fragments) when the bone is fractured. An ANCOVA test performed on the slopes of the three lines indicates a statistically significant difference in slopes in the intact case and the lower fractured fragments at a confidence level of 75%.

Axial shear strain elastograms

The computation of the statistical parameters to analyze the quality of the axial shear strain elastography data provided the following values. In the intact case, the mean SNR_{asse} computed from 24 cases was 3.42, with a standard deviation of 0.35. On the other hand, the SNR_{asse} values had mean absolute values of 4.07 (std. dev. 0.39) in the positive direction and 4.21 (std. dev. 0.43) in the negative direction, respectively. These results are graphically represented in figure 39(a). The distributions of mean SNR_{asse} obtained in the intact cases and absolute values of the mean SNR_{asse} obtained in the region containing positive axial shear strains and negative axial shear strains, taken separately, from the fractured cases were compared. An analysis of variance of these population means based on the Kruskal-Wallis test rejects the hypothesis that the mean values of the SNR_{asse} of the axial shear strain elastogram in the soft tissue region around the bone remains the same before and after inducing a fracture in the same with a p-value < 0.0001. Specifically, the SNR_{asse} increases with the presence of the fracture.

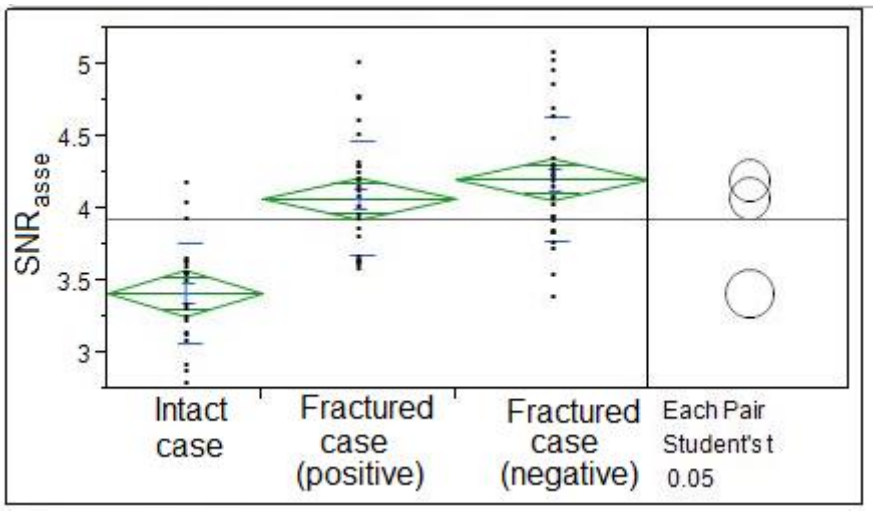

(a)

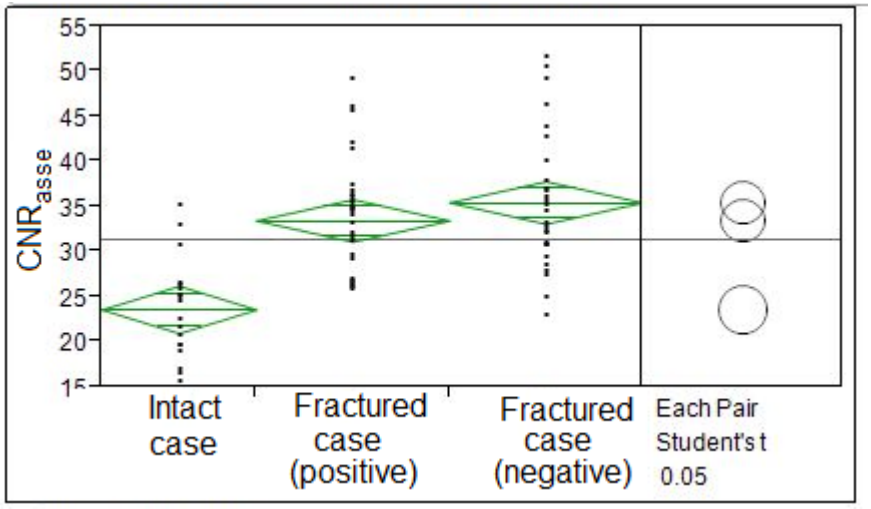

(b)

Figure 39. Results of statistical analysis of axial shear strain elastograms obtained from intact and fractured tibias. (a) Comparison of mean SNR_{asse} values of axial shear strain values obtained from intact cases, with respect to the absolute values of SNR_{asse} from positive and negative axial shear strain regions in the fractured cases. (b) Comparison of mean CNR_{asse} values of axial shear strain values obtained from intact cases, with respect to the absolute values of CNR_{asse} from positive and negative axial shear strain regions in the fractured cases.

A similar analysis was performed on the CNR_{asse} values of the axial shear strains before and after the fractures were induced. In the intact cases, the CNR_{asse} values had a mean value of 23.64 (std. dev. 4.94) which increased to 33.52 (std. dev. 6.54) in the positive axial shear strain region, and 35.52 (std. dev. 7.4) in the negative strain regions, respectively. Figure 39(b) compares the distribution of mean CNR_{asse} obtained in the intact cases, and the absolute values of the mean CNR_{asse} obtained in the region containing positive axial shear strains with the negative axial shear strains taken from the fractured cases. Kruskal-Wallis analysis performed on these values rejects the hypothesis of similarity of CNR_{asse} values before and after the fracture with a p-value < 0.0001. Specifically, CNR_{asse} values go up (as in the case of SNR_{asse}), suggesting an enhancement in the contrast between axial shear strain values at the bone/soft tissue interface as compared to those in the soft tissue background in the presence of a fracture.

Discussion

In this paper, we demonstrated the feasibility of using novel ultrasound elastography techniques to assess musculoskeletal tissues, intact and fractured long bones and obtain tissue mechanical information complementary to what standard ultrasound imaging methods provide. Elastography techniques are based on different contrast mechanisms. Axial strain contrast is related to the underlying variations in elastic moduli of the soft tissue and bones as well as the boundary conditions while the contrast in axial shear strain elastograms is related to the level of connectedness between different tissues layers.

In the cases analyzed here, the bone/soft tissue interface as well as connective tissues typically manifest as regions of high correlation. The most superficial bone layer likely undergoes rigid motion (or very low strains) when subjected to compression, which would explain the observed high correlations. The decorrelation areas immediately below the bone surface may be due to the acoustic impedance mismatch between bone and soft tissue as well as a loss of signal in the bone. The presence of this correlation contrast may help with locating the bone/soft tissue interface. When used along with other types of co-registered ultrasound images, correlation maps could potentially also provide structural information regarding the connective tissues in the fractured area, orientations of the bone fragments with respect to each other (within the plane of observation) and the separation between them – all of which might be clinically relevant.

The quality analysis performed on the axial strain elastograms indicates that the axial strains observed in the background soft tissue as well as at the bone/soft tissue interface increases linearly with respect to applied axial strain. These results were consisted across all cases analyzed in this study. This also translates to a gradual increase in CNR_e with respect to applied strain. Furthermore, the mean axial strains at the bone/soft tissue interface may reduce when the bone undergoes a fracture. The reduction in observed axial strains is unequal over fracture fragments that might be misaligned, with the interface above the deeper fragment experiencing lower strains than those above fragments that are relatively shallower. Furthermore, we have shown the difference in mean axial strains experienced at the bone/soft tissue interface and the background soft

tissue to be statistically different in intact bones when compared with the lower fragments in fractured bones. These observations are consistent with the notion that the boundary conditions at the bone/soft tissue interface likely undergo changes in the presence of a fracture. Hence, the axial strain at the bone/soft tissue interface might be used to infer information about the integrity of the underlying bone. This important observation is currently tested on a larger number of samples. Also, only limited information is derivable from *in vitro* tissues, and ultimately *in vivo* experiments may be required to fully elucidate the potentials of axial strain elastography for the assessment of the bone and surrounding soft tissue.

From the present study, a predominantly unidirectional axial shear strain pattern in the case of intact bones subjected to an oblique compressive force. Typically, it is not difficult to induce such shear strains in the soft tissue due to the uneven surface of the tissue above the bone. On the other hand, in the presence of a fracture, the axial shear strain patterns at the bone/soft tissue interface become bi-directional. The strength and extent of the shear strains might provide functional information regarding the motion of the bone fragments as well as the soft tissue.

As a reference, Thittaikumar et al reported a CNR_{asse} of about 36 in the ASSEs obtained in an earlier study involving experiments conducted on gelatin phantoms (Thitaikumar et al. 2007b). In our study, we have found comparable CNR_{asse} values of 24-35 in all cases. Moreover, both SNR_{asse} and CNR_{asse} increase after the fracture has been induced in the sample, hence implying an enhancement in the relative motion between the bone and surrounding soft tissue that undergoes physical trauma. Such

behavior could be anticipated in a real life scenario during the early stages of the bone healing process (Schindeler et al. 2008). In recent studies, the process of regrowth of bones has also been shown to be strongly dependent on the composition and structure of the surrounding soft tissue (Gonzalez 2008; Duda et al. 2008). Hence, the ability to image soft tissue as well as the regrowth of the fractured bone can prove to be valuable in a clinical scenario. Furthermore, an analysis of the separation between the two regions of opposite shear strains (figure 33) indicates that the more complete the fracture, i.e., the greater the relative motion between the bone fragments, the smaller the gap separating the corresponding regions of axial shear strain in the ASSE. Thus, the ASSE might provide information about the severity and stability of a fracture. This information is not obtainable using standard ultrasound imaging or x-rays.

Ultrasound elastography techniques targeting musculoskeletal applications may be useful in several medical areas, which range from military and sports medicine to pediatric orthopedics and orthopedic regenerative medicine (Cho et al. 2008). Additionally, automated 3D ultrasound reconstruction methods of bones could benefit from elastography information.

Here we now report a brief discussion of the challenges and limitations of the presented study. First, the analysis in the current study was carried out on canine and ovine tibias *in vitro*. While *in vitro* experiments can be designed to closely resemble *in vivo* scenarios, it is hard to fully control the induction of a fracture, displacement between fragments, angle of the cut induced and angle of insonication. Each of these parameters needs to be analyzed separately to see the influence it may have on the

elastographic images. Consequently, a simulation study that allows control on these parameters individually would provide important information on the potentials and limitations of the axial strain and axial shear strain elastograms. Such study would also allow analyzing the advantages and disadvantages of using the axial shear strain component alone versus the complete shear strain tensor. However, a comprehensive simulation tool that allows modeling bone soft tissue and their mechanical interaction is considered beyond the scope of this feasibility study and is left for future work. Furthermore, the development and use of 3D elastography techniques may be required to fully assess the bone/soft tissue mechanical interaction, especially *in vivo*. In a real life scenario, the fracture region is known to be physiologically very active as the body reacts to the fracture and starts the healing process. To fully understand the real behavior of the soft tissue in the fractured region may require the development of advanced 3D elastography techniques and elaborate comprehensive *in vivo* study.

Conclusions

We have successfully demonstrated the ability of ultrasound elastography to assess intact and fractured bones *in vitro* and provide information about the bone behavior that is not attainable using standard ultrasound methods. A comprehensive statistical analysis of the obtained elastographic results has been presented. Based on these results, ultrasound elastography modalities have the potential to significantly impact the clinical analysis of intact and fractured long bones and may be useful in studying healing.

5. STUDY ON THE APPLICABILITY OF ULTRASOUND ELASTOGRAPHY TECHNIQUES FOR ORTHOPEDIC APPLICATIONS USING *IN VIVO* SAMPLES

Introduction

In the previous section, we demonstrated the ability to generate high quality axial strain and axial shear strain elastograms of intact and fractured tibias *in vitro*. The results were obtained from experiments carried out on excised bone samples in controlled laboratory environments. In the present paper, we explore the applicability of the elastography techniques to bone samples obtained from *in vivo* sheep samples. The challenges associated with *in vivo* elastography have already been enlisted earlier (Chandrashekhar et al 2006). The primary concerns are loss of correlation due to tissue and/or user motion, loss of spatial resolution and reduced signal-to-noise ratios (SNR) and contrast-to-noise ratios (CNR).

To alleviate some of these problems, some compromises were made in the current study. Primarily, strain estimation was performed for every consecutive pair of frames, rather than applying a multi-compression technique that worked well *in vitro*. The direct consequence of this was reduced SNR due to low tissue displacement magnitude, hence making the strain computation sensitive to elastography noise. However, this technique helped maintaining high correlation coefficients due to the ability to track tissue motion with higher spatial resolution. Also, a manual analysis of acquired frames was performed to first select the usable range of consecutive frames for each experiment. This reduced the number of frames contributing to the aggregate axial

strain and axial shear strain elastograms, but no significant loss of correlation was observed.

The results of performing *in vivo* elastography experiments on sheep samples are presented here. Included are details on the optimization of elastography parameters and a statistical analysis of the quality of axial strain and axial shear strain elastograms obtained for the experiments. Finally, potential applications are discussed in light of the results obtained.

Methods

In vivo elastography experiments were carried out on intact tibias of 8 live sheep. In general, data acquisition was performed from the left tibia in each sample, except one sheep, where the right tibia was used. Also, in two cases, data were acquired from both tibias in the sheep, thus giving a total of 10 independent samples for the experiments.

Prior to performing the data acquisitions, the samples were prepared by first clipping the sheep hair at the designated scan location. Freehand elastography experiments were then carried out on the unanesthetized sheep using a Sonix RP (Ultrasonix, Richmond, BC, Canada) system. The acquisition protocol involved using a 38-mm linear array transducer operating at a center frequency of 6.6MHz. Other parameters of the transducer include 5-14MHz bandwidth and 1mm beamwidth at focus. A mild compressive force to generate applied strains of about 2-5% was applied to the transducer along with a 40mm x 40mm compressor attached to the face of the transducer. This compressor plate was used to ensure uniform distribution of the compression onto the surface of the soft tissue. Ultrasound gel was applied on the

surface of the tissue to ensure good coupling. Raw RF data were acquired during compression with the transducer held such that the axis of the bone was parallel to the acquisition plane. For each experiment, about 150 to 600 RF frames were acquired from the area of interest.

The acquired raw RF data were processed offline. Each experiment was manually analyzed to isolate frames where the applied strain increased monotonically and lateral motion was minimal. This was done by generating a B-mode image for each RF frame by applying the Hilbert transform, delineating the bone/soft tissue interface on the basis of the high echogenicity of the bone in each image and then tracking the interface for the duration of the experiment. The displacement of the interface between consecutive frames was computed by taking the point-wise difference in the position of the lines in the two frames and selecting the median value of the computed displacements. This operation was repeated for every consecutive pair of RF frames for the experiment. Finally, the displacement of this line over the duration of the experiment was plotted and a range of frames was selected such that the displacement within this range was either zero or consistently unidirectional, i.e., such that the bone/soft tissue interface always moved closer to the transducer face. The largest possible range of frames was selected for each experiment so as to maximize the signal-to-noise ratio (SNR) in the elastograms. Total displacement of the interface within the selected frames was computed using the same technique as above, except instead of using consecutive frames, the frames at the extremities were used in this case. The applied strain was then

computed as the ratio of the total displacement and the median value of the position of the bone/soft tissue interface within the B-mode image.

Next, for the selected frames, axial displacements between every consecutive pair of frames were computed using a cross-correlation algorithm with the following signal processing parameters: window length – 1.5mm, overlap between consecutive windows: 80%, lateral kernel size: 5 A-lines. A least squares approach was used to compute the axial strains and axial shear strains from the axial displacements. Mean correlation maps, axial strain elastograms and axial shear strain elastograms were generated for each experiment by adding together the results obtained for individual pairs of frames.

Quality analysis was then performed separately for the axial strain elastograms and the axial shear strain elastograms respectively. Cases where the bone/soft tissue interface underwent significant decorrelation or those in which the interface was not distinguishable from the bone or the background soft tissue due to insufficient contrast were eliminated from further consideration.

Axial strain elastography

To statistically analyze the quality of the axial strain elastography results, mean strains were computed for background soft tissue and the tissue at the bone/soft tissue interface. Background tissue was loosely defined as tissue that was far away from the transducer's face (so as to avoid the near field region) as well as from the bone/soft tissue interface (> 5mm). The region was also relatively uniform and devoid of structures such as connective tissue, skin etc. To analyze the strains at the bone/soft

tissue interface, an 8-12 pixel (2.5mm - 4.0mm) thick region of interest (ROI) was manually selected above the low strain region in the corresponding elastogram. Pixels corresponding to those having low values of correlation coefficients (<0.95 in most cases) were masked out of the ROI to ensure reliable results. Finally, a threshold, computed as a function of the mean applied axial strain, was applied to the region, i.e., pixels having mean axial strain values below the threshold value were masked out. Parameters such as mean, standard deviation, SNR_e and CNR_e were computed from the remaining pixels.

Axial shear strain elastography

An analysis of the axial shear strain elastography results was also carried out to study the quality of the elastograms. In order to do this, binary images of the axial shear strain elastograms were created to isolate the signal at the bone/soft tissue interface. This was done by first manually delineating the interface using structural information obtained from a combination of B-modes, correlation maps and axial strain elastograms. As in the case of axial strain elastograms, an ROI with thickness 8-12 pixels thick at the bone/soft tissue interface was separated out in order to eliminate connective tissue and other anatomical features that contributed with a non-zero axial shear strain signal. Next, the axial shear strain signals were normalized with respect to mean applied axial strain in order to be able to compare results across different experiments. An approximate estimate of the applied axial strain was obtained by computing the mean observed axial strain value in the background soft tissue - a region further away from the bone/soft tissue interface that was relatively uniform and devoid of interfering anatomical features.

A threshold was then applied to the ROI as a percentage of the mean axial strain so that all axial shear strain values below the threshold were zeroed out. Quality parameters such as mean, standard deviation, SNR_{asse} and CNR_{asse} were computed for the remaining pixels.

Results

Axial strain elastography

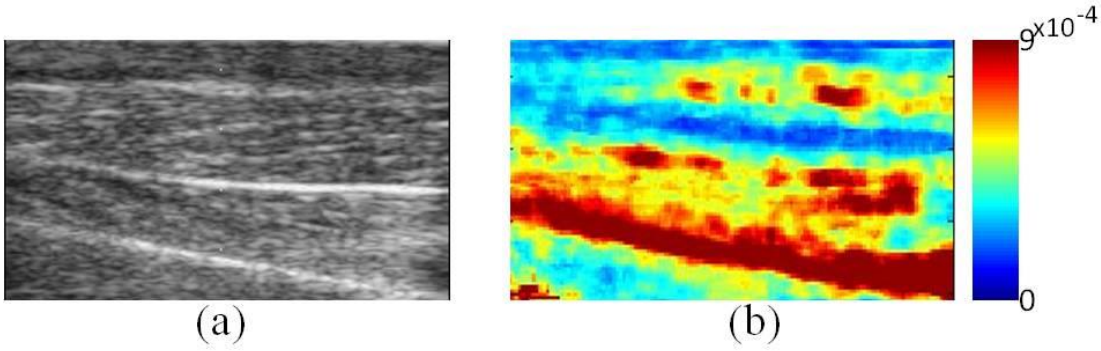

Figure 40. Ultrasound imaging results from elastography experiments performed on intact sheep tibia *in vivo*. (a) B-mode image and (b) the corresponding axial strain elastogram obtained from the same plane. The bone/soft tissue interface is visible as a hyperechoic line in the former, and as a high strain region in the latter. Also visible is a connective tissue in both the images.

Figure 40 above depicts a typical B-mode image of intact sheep tibia *in vivo*, along with the corresponding mean axial strain elastogram. The elastogram shown here was obtained by processing all frames within the experiment and then eliminating about 2-5% of the frames containing a significant number of pixels with low correlation coefficients. The dynamic range has been set so as to be able to visualize the bone/soft tissue interface, as well as the background soft tissue. As in the *in vitro* cases, the bone and connective tissues show up as low strain regions, whereas the bone/soft tissue

interface and other tissue structures like fatty tissue etc. show up as high strain regions. One observation peculiar to *in vivo* cases is that in some cases, the bone/soft tissue interface is saturated with high strains, as compared to *in vitro* cases.

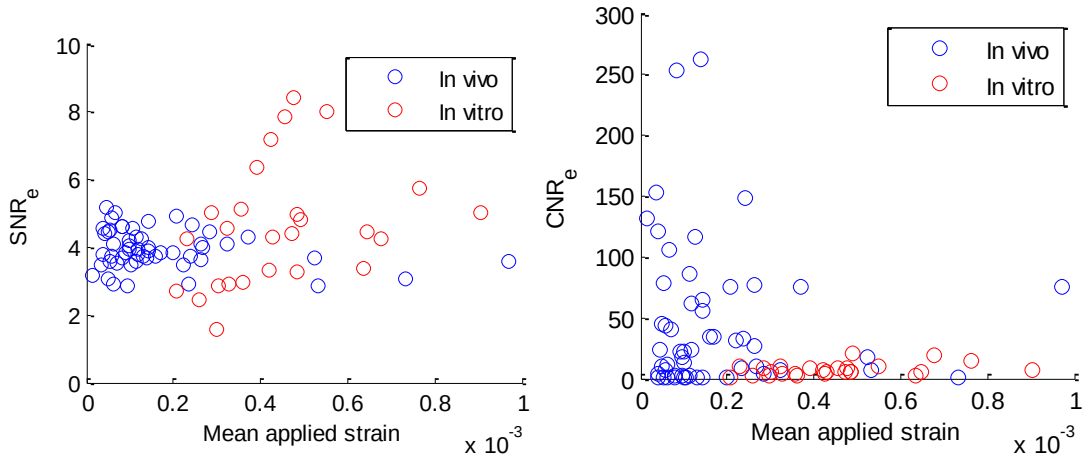

(a) (b)

Figure 41. Comparison of the distribution of SNR_e and CNR_e values of axial strain elastograms *in vitro* and *in vivo*. (a) Scatter plot of SNR_e values of the axial strain elastograms in the bone/soft tissue interface *in vitro* (blue) and *in vivo* (red). (b) Scatter plot CNR_e values of axial strain elastograms of the bone/soft tissue interface compared with background soft tissue *in vitro* (blue) and *in vivo* (red).

The statistical analysis on axial strains was carried out on results obtained from 54 cases. Figure 12 depicts the quality of image parameters obtained from the axial strain elastograms *in vivo*, and compared with similar parameters *in vitro*. Figure 41(a) depicts the variation of SNR_e of the mean axial strain elastograms in vivo with respect to applied strain (blue scatterers). Also depicted in the same plot are the corresponding SNR*e* values obtained *in vitro* (red scatterers). The distribution of SNR_es in vivo (2.8-5.2) can be observed to be relatively constrained as compared to the *in vitro* values (1.5-

8.5). Figure 12(b) depicts a similar variation of CNR_es *in vivo* (blue) and *in vitro* (red). The highest CNR_e observed *in vitro* is of the order of 20, whereas values as high as 265 are observed *in vivo*. About 50% of the *in vivo* CNR_e values are outside the *in vitro* range, with all of the outliers being on the higher side. The results are currently being investigated

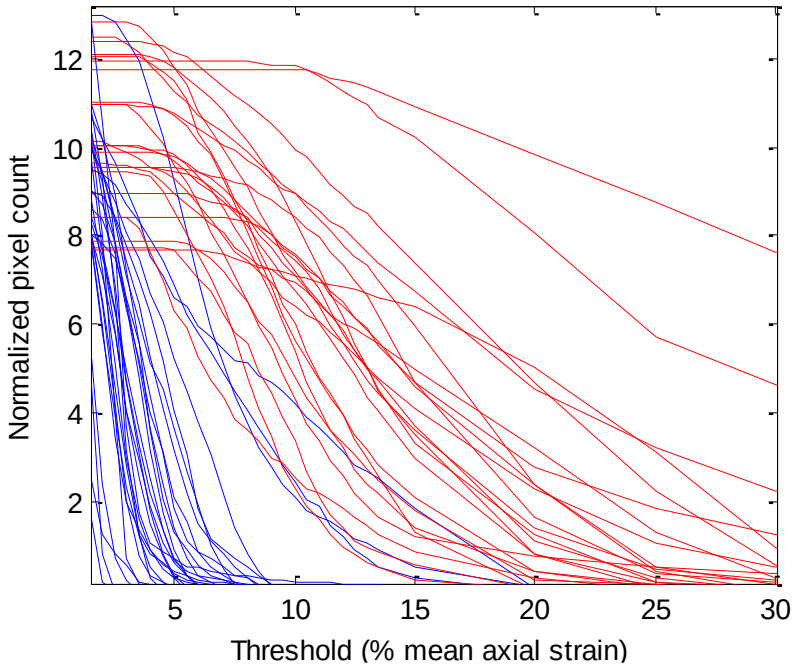

Figure 42. Plot showing variation of thickness of the bone/soft tissue interface with respect to applied threshold in the axial strain elastogram. The lines in red correspond to those cases where the thickness is constant at an applied threshold of 1.5 and 2 times mean applied axial strain.

An analysis was carried out to study the relationship between the strains in the bone/soft tissue interface with respect to applied strain. Figure 42 above shows the

variation in number of pixels remaining within the bone/soft tissue interface as a function of the applied threshold, which is a multiple of the mean applied strain. Along the Y-axis, the number of pixels is normalized with respect to the length of the ROI in the lateral direction, so the graph can be seen as a variation of mean thickness of the bone/soft tissue interface with respect to increasing threshold values. As anticipated, the mean thickness of the interface gradually reduces with increasing threshold values. In about 27 cases out of 54 (indicated by blue lines in the graph), the mean thickness of the interface diminishes to about 2% of the original value at a threshold that is 9 times the mean applied axial strain, whereas in 10 cases, the thickness remains above 20% of the applied strain at the same threshold. This indicates a wide range of axial strains generated at the bone/soft tissue interface *in vivo* when applied strain is the same.

Axial shear strain elastography

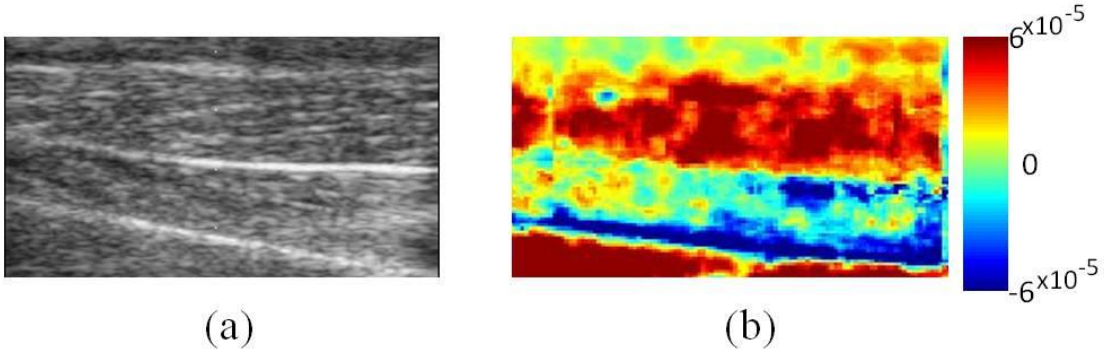

Figure 43. Ultrasound imaging results from elastography experiments performed on intact sheep tibia *in vivo*. (a) B-mode image (same as in figure 40(a)) and (b) the corresponding axial shear strain elastogram obtained from the same plane. The bone/soft tissue interface is visible as a hyperechoic line in the former, and as a low negative strain region in the latter.

Figure 43 depicts the axial shear strain elastogram obtained from an intact sheep tibia from the same position as that shown in the B-mode image in Figure 40. As in the axial strain elastography result, this axial shear strain elastogram was obtained by processing all the frames in the experiment, and eliminating about 2-5% of the frames containing a significant number of pixels with low correlation coefficients. As in the *in vitro* cases, the strongest portion of the signal is at the bone/soft tissue interface. The signal is also primarily unidirectional at the interface.

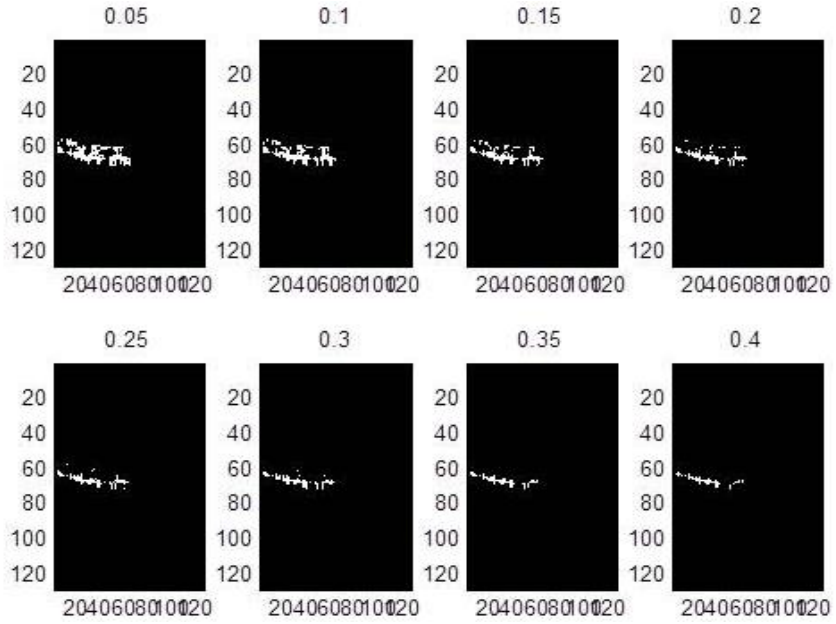

Figure 44. Series of binary images depicting variation in the number of pixels remaining at the bone/soft tissue interface in the axial shear strain elastograms with respect to applied threshold.

Figure 44 depicts a series of binary images obtained by applying a gradually increasing threshold of 5%-40% of applied mean axial strain to the axial shear strain

elastogram at the bone/soft tissue interface for one case. Figure 45 depicts the variation within the corresponding axial shear strain elastograms in the ROI.

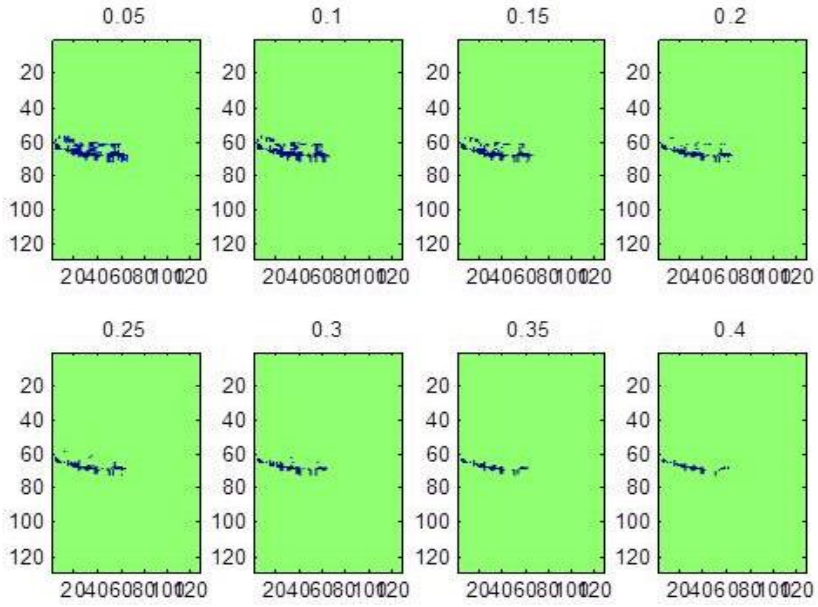

Figure 45. Series of images depicting the variation of the thresholded region in the bone/soft tissue interface with respect to applied threshold.

As can be seen from the two images, gradually increasing the threshold values leads to eliminating pixels that are not in the bone/soft tissue interface, indicating that the highest axial shear strain values are seen close to the interface. The reduction in the number of noisy pixels is also evident in figure 46, where the variation in the standard deviation of the axial shear strain values within the thresholded ROI is plotted against increasing values of threshold for 12 experiments.

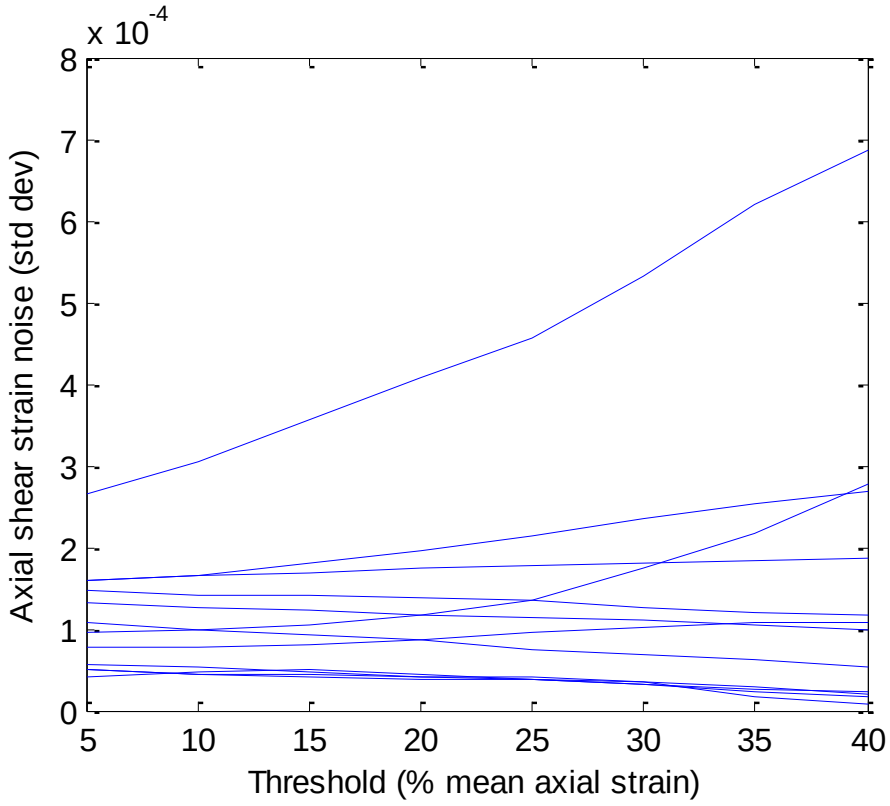

Figure 46. Plot depicting the variation in the standard deviation of the axial shear strain elastogram bone/soft tissue interface with respect to applied threshold.

From the figure, the noise in the image reduces with increasing threshold value in 9 cases out of 12, indicating that the thresholding process aids in eliminating pixels that do not belong to the bone/soft tissue interface of interest. An analysis of the 2 cases where the opposite trend is observed shows that there are not sufficient pixels in the thresholded region to generate reliable statistical estimates of the noise. In just one case, there is no explanation for the increasing trend.

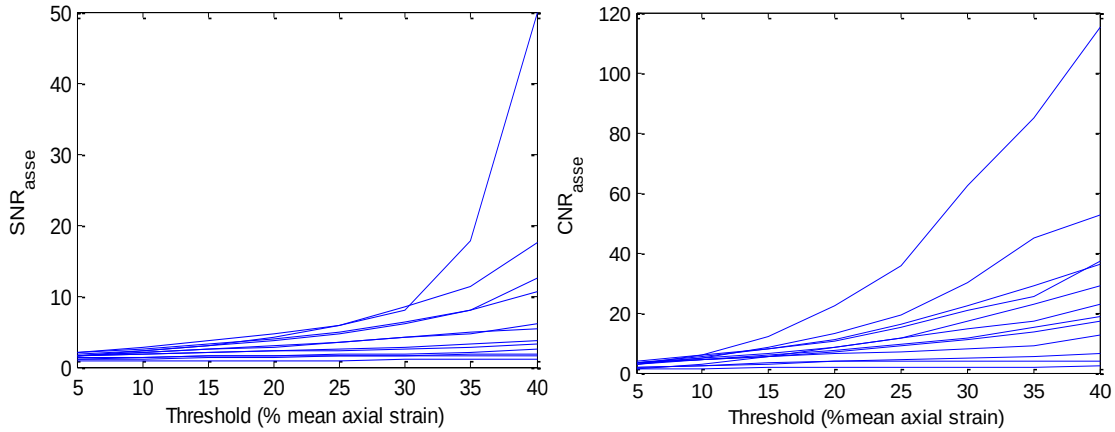

(a) (b)

Figure 47. Statistical analysis of image quality parameters in axial shear strain elastograms obtained from intact sheep tibia *in vivo.* (a) Plot depicting the variation of SNR_{asse} and (b) CNR_{asse} in the bone/soft tissue interface with respect to background soft tissue as a function of applied threshold.

Figures 47(a) and 47(b) above depict the variation of SNR_{asse} and CNR_{asse} with increasing threshold values for the 12 cases. Focusing on a 20% threshold, i.e., considering cases that have sufficient number of pixels (>50) to generate reliable statistics, we obtain a mean SNR_{asse} of 2.69±1.24 and CNR_{asse} of 8.61±5.38.

Discussion

The results obtained in this paper show that it is possible to generate high quality axial strain and axial shear strain elastograms of the bone/soft tissue interface of long bones, specifically tibias, from *in vivo* samples. The patterns observed from live sheep samples are qualitatively similar to those from *in vitro* samples of canine and ovine tibias, despite the challenges associated with data acquisition in the former case. While it is possible to perform quantitative analysis on the elastography results obtained, comparison of the statistical parameters with those obtained *in vitro* requires a definite

estimate of applied axial strain, which is difficult *in vivo* due to motion associated with freehand data acquisition. As a result, the results presented here are derived from elastograms pertinent to a subset of the acquired data in each experiment wherein applied strain is reliably estimated.

The statistics obtained in the paper are obtained by manually selecting the regions of interest (ROI) in axial strain elastograms and axial shear strain elastograms, which was based on strain contrast observed at the bone/soft tissue interface in the respective elastograms, as well as structural information in the B-modes and correlation maps. The application of the respective thresholds after the selection process ensures that most of the irrelevant pixels are masked out. As a consequence, the statistical parameters computed for further analysis are not significantly affected by minor variations in the manually selected ROI.

The analysis of 54 axial strain elastograms obtained *in vivo* reveals a diminished SNR_e compared to the values *ex vivo*. This is very likely due to significant motion, which brings in noise due to motion. Another contributing factor is the elastography noise introduced due to processing consecutive sets of frames, hence violating the rules at the lower end of the strain filter. However, the distribution of the SNR_es *in vivo* is well within the range observed *in vitro*. In comparison, the CNR_e plot in 41(b) indicates a wider range of induced axial strains at the bone/soft tissue interface. Significant variation in the statistical parameters derived from the axial strains at the interface is observed both intra-sample as well as inter-sample. This indicates that the axial strain elastogram depends not only on the sample from which data was acquired, but also the plane at

which the acquisition is performed. Hence, elastography for assessment of musculoskeletal tissues, particularly in the case of long bones, is inherently a 3D problem. Generation of 3D axial strain elastograms using data acquired tomographically around the bone axis may be required to obtain comprehensive information regarding the health of the bone. Furthermore, the significantly high values of CNR_es observed *in vivo* are indicative of a difference in tissue physiology. Consequently, the higher strain values might be indicative of the presence of soft tissue rich in fluids, such as due to blood vessels or edema. The ability to monitor these regions in fractured bones and compare them with control cases might be able to provide information regarding the bone healing process. Simple screening procedures that show presence of edema in seemingly intact cases might also help in detecting abnormalities in the bone and/or surrounding soft tissue. This is particularly important in scenarios where x-ray based techniques cannot be used due to lack of sensitivity to variations in soft tissue integrity.

The axial shear strain analysis carried out here is based on elastography results obtained from 12 cases. It is important to note that this a retrospective analysis carried out after all the data acquisition had already been performed. The majority of the experiments comprised of cases where the bone was horizontal or nearly horizontal. As a result, the axial shear strain signal obtained at the bone/soft tissue interface in these cases was unreliable due to low correlation coefficients or had a magnitude comparable to the background axial shear strain values, hence making the interface indistinguishable in the corresponding elastogram. For future experiments, it will be important to carry out elastography experiments where the bone is at an angle with respect to the applied strain.

The strain patterns in the axial shear strain elastograms *in vivo* are similar to what we expect to see *in vitro*. However, the SNR_{asse} and CNR_{asse} values obtained here are lower than those typically reported in literature, and also lower than typical values we see in *in vitro* studies. This is expected, considering *in vivo* experiments tend to be noisier due to motion experienced during freehand data acquisition. The number of frames used to compute the mean strain values are also significantly lower as a consequence, which leads to lower SNR_{asse} values. Nevertheless, the values are sufficient to be able to obtain information about the integrity of the bone/soft tissue interface. Aside from the interface, the axial shear strain elastograms can also provide information about the integrity of connective tissue, which was ignored for the present study on intact bones. However, in cases where the connective tissue is affected due to underlying pathologies or defects in the bone, the modality can provide clinically relevant information to aid proper diagnosis.

The results presented in this study opens up a number of new problems that are yet to be solved. One of the most important ones is that a number of cases had to be eliminated from statistical analysis due to significant decorrelation at the bone/soft tissue interface. An understanding of the physics of interaction of the ultrasound beam with tissues having high stiffness contrasts, such as that observed at the bone/soft tissue interface, via simulations will perhaps help correct for the decorrelation, and hence generate more reliable elastography results.

Also, the current analysis relies to a substantial degree on manual inspection of individual frames, and is hence prone to human error. An automated technique to

process frames to derive applied strains would be more effective and reliable. Another important problem is to study the quality of elastography results obtained *in vivo* on fractured samples, both in animals as well as in humans.

Conclusions

We have successfully demonstrated the ability to perform elastography experiments *in vivo* to derive information about the bone/soft tissue interface. While the quality of the elastograms are inferior to those derived *in vitro*, SNR and CNR values are sufficiently high as to be able to help with providing clinically relevant information that might be usable for diagnoses of defects in long bones.

6. CONCLUSIONS

Summary

Ultrasound imaging techniques are promising alternatives to other imaging modalities for application to orthopedics. This dissertation studies the feasibility of applying ultrasound based 2D, 3D and elastography imaging techniques to obtain structural as well as functional information about intact and fractured bones using *in vitro* and *in vivo* animal samples. These techniques have the potential to provide information about the structural stability of bones, location and severity of fractures and the ability to non-invasively monitor the progress of bone healing.

Section 2 highlights the performance analysis of standard 2D and 3D ultrasound techniques when imaging bone defects *in vitro*. The ultrasound imaging results obtained from controlled defects in both, mammalian as well as non-mammalian bones were found to agree well with corresponding results obtained from optical microscopy and x-ray imaging techniques. Furthermore, 3D reconstructions of bone surfaces obtained in real time and with high contrast-to-noise ratios helped with easier interpretation of location and severity of defects.

In section 3, the earlier analysis on the use of 3D ultrasound imaging techniques has been extended to intact and fractured bones *in vitro* wherein the surrounding soft tissue was left intact. From the quantitative study on the imaging contrast obtained through 3D ultrasound imaging, it is concluded that these methodologies can be used to

image appendicular skeletal defects and complex bone fractures within a variety of tissue samples.

Section 4 focuses on using ultrasound elastography techniques to assess intact and fractured bones *in vitro*. Using data obtained by performing elastography experiments on tibias *in vitro*, the axial strains in the bone/soft tissue interface were statistically shown to reduce when a fracture is induced in the bone. Furthermore, the axial shear strain values at the interface become bidirectional and also undergo an increase in magnitude in the presence of a fracture. As a result, it has been concluded that these techniques can be used to gather information regarding the integrity of the underlying bone, and about the severity of the fracture.

In section 5, the above analysis has been extended to intact tibias *in vivo*. The statistical analysis show that significant motion encountered during data acquisition lead to reduction in the quality of the axial strain and axial shear strain elastograms, but the SNR and CNR values allow for clinically relevant information that can help with diagnosis of bone defects.

In the following section in the present section, some results of the application of ultrasound elastography techniques to monitor bone healing and to image human bones *in vivo* are presented. These results bring up some suggestions on the potentials for future applicability of ultrasound elastography techniques to bone imaging.

Future Work

Based on the data reported in this dissertation, a number of future research projects have been envisioned. Some of these projects are briefly highlighted below.

Monitoring bone healing *in vivo*

In this dissertation, elastography has been applied *in vitro* as well as *in vivo* on intact tibias, and *in vitro* only in the case of fractured tibias. An analysis of the axial strain and axial shear strain elastograms obtained show that it is possible to obtain information regarding the integrity of the underlying bone. It was also hypothesized that it may be possible to obtain information about the healing bone based on the axial strain and axial shear strains observed at the bone/soft tissue interface.

As part of a larger study on the use of BioNanoScaffolds for post-traumatic osteoregeneration, the elastography technique was applied to a healing bone *in vivo* on a single sheep tibia. The results appear to show some elastography changes that could be related to various phases of bone formation. However, an elaborate analysis of the performance of elastography in the assessment of bone healing process requires a much larger and more standardized animal or human study. A greater sample set would provide information regarding scenarios involving misalignment of bone fragments, non-unions, variations in healing environments etc. that might affect the healing process. Furthermore, the presence of edema and hematoma at the fracture location indicate an accumulation of fluids, which influence the rate of bone regrowth.

The temporal variation of strains at the bone/soft tissue interface due to the presence of fluids may be better analyzed using poroelastography techniques (Righetti et al 2005). These techniques involve acquisition of axial strain or effective Poisson's ratio elastography data over extended periods of in the ROI. The resulting poroelastograms provide spatial information regarding the temporal mechanical behavior of the tissues,

ostensibly related to fluid. The use of poroelastography techniques to analyze the variation in fluid retention properties at the bone/soft tissue interface may help better characterizing bone regeneration.

In vivo elastography on human volunteers

The applicability of elastography techniques to musculoskeletal tissues has been demonstrated *in vivo*, although experiments have only been performed on sheep samples so far. The techniques might be better applicable to assess long bones in human volunteers, given that typically there is less motion involved and the bones are better accessible by the imaging transducer. As a proof of principle, *in vivo* data was acquired from the forearm of an adult human volunteer to image a human radius.

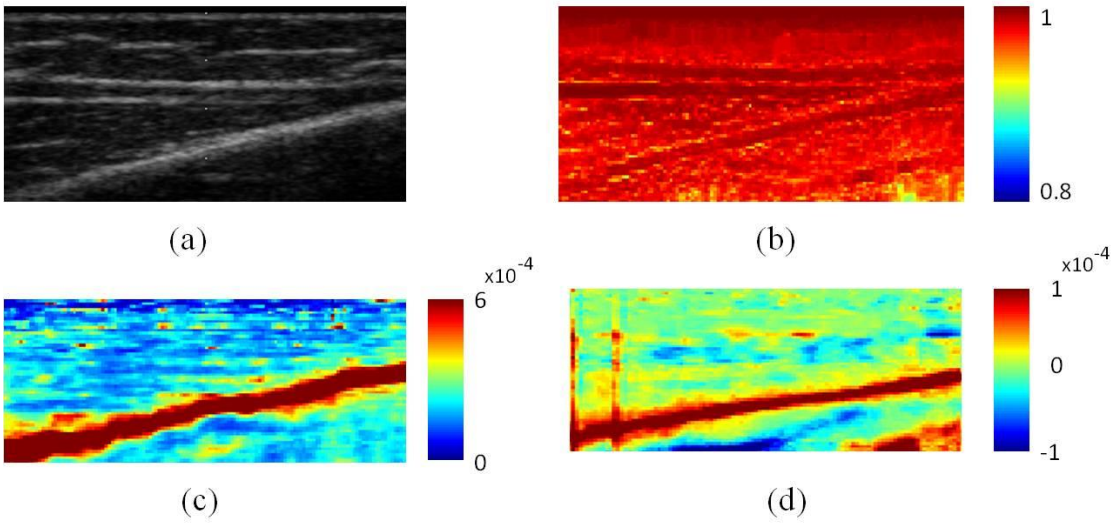

Figure 48. Ultrasound elastography results of experiment performed on an intact human radius *in vivo*. (a) B-mode image of the radius. The bone is clearly visible as the hyperechoic line oblique to the transducer face. (b) Corresponding correlation map (c) Axial strain elastogram (d) Axial shear strain elastogram. ROI: 20mm x 35 mm.

Figure 48 above depicts the mean correlation map, mean axial strain elastogram and mean axial shear strain elastogram and the corresponding B-mode obtained *in vivo*. The bone/soft tissue interface is clearly visible in all the images. As in the case of the *in vivo* sheep data, the axial strain elastograms indicate high strains at the interface, and the saturation levels are indicative of the probable presence of fluids in the region. The axial shear strain elastograms depict strain concentrations at the bone/soft tissue interface, indicative of the bonding between the soft tissue and the bone. While these results seem to be consistent with the *in vitro* as well as *in vivo* results shown in this dissertation, further experiments are required to statistically and comprehensively assess the feasibility of using elastography techniques in human applications.

3D elastography

The patterns seen *in vitro* as well as *in vivo* reflect underlying physiology of the bone/soft tissue interface, which might vary from acquisition plane to acquisition plane. This variability is particularly critical in the case of fractured bones. Consequently, in the future, the elastography modality needs to be extended in 3D wherein data is acquired from multiple parallel planes and a reconstruction of the volume data is performed so as to visualize elasticity data in 3D. This would help better localization of signature data that can lead to better diagnoses.

Simulation studies

The ability to truly control experimental conditions *in vivo* and *in vitro* is limited, particularly when complex tissues such as the bone/soft tissue interface are involved. Primarily, the physics of interaction of the ultrasound beam with the bone tissue is

understood only to a limited extent. For instance, a number of correlation maps are characterized with drastically low correlation coefficients at the bone surface. Currently, it is not clear why these low correlation coefficients show up only in a few cases – simulation studies will help explain this phenomenon and many others like this.

Furthermore, it is difficult to control the exact parameters such as inclination of the bone with respect to the transducer face, the bonding at the bone/soft tissue interface and separation between fracture fragments. These parameters seem to affect the quality of the axial strain elastograms and axial shear strain elastograms. A thorough characterization of the elastography modality to assist in clinical diagnosis can be accomplished by performing a detailed simulation analysis of the physical phenomena that affect the various strain patterns. Aside from being inexpensive, the studies allow for flexibility in being able to control experimental parameters in a manner, which is not possible *in vitro* or *in vivo*.

REFERENCES

Abdel-Dayem H M 1997 The role of nuclear medicine in primary bone and soft tissue tumors Semin. Nucl. Med. 27 355–63

Anonymous 2012 BET 2: Can ultrasound be used to diagnose clavicle fractures in children? Emergency Medicine Journal 29 7 599-600

Arni D, Lambert V, Delmi M and Bianchi S 2009 Insufficiency fracture of the calcaneum: sonographic finding J. Clin. Ultrasound 37 424–7

Banal F, Etchepare F, Rouhier B, Rosenberg C, Foltz V, Rozenberg S, Koeger A C, Fautrel B and Bourgeois P 2006 Ultrasound ability in early diagnosis of stress fracture of metatarsal bone Ann. Rheum. Dis. 65 977–8

Barata I, Spencer R, Raio C, Ward M and Sama A 2011 Ultrasound Detection of Long Bone Fractures in Pediatric Emergency Department Patients Ann. Emerg. Med. 58(4) S182-3

Berrington de Gonzalez A, Mahadevappa M, Kim KP, et al. 2009 Projected cancer risks from CT scans performed in the United States in 2007 JAMA Internal Medicine 169 2071-7

Bland J M and Altman D G 1986 Statistical methods for assessing agreement between two methods of clinical measurement Lancet 1 307–10

Bland J M and Altman D G 1999 Measuring agreement in method comparison studies Stat. Methods Med. Res. 8 135–60

Blake G M, Gluer C C and Fogelman I 1997 Bone densitometry: current status and future prospect Br. J. Radiol. 70 S177–86

Bodner G, Stockl B, Fierlinger A, Schocke M and Bernathova M 2005 Sonographic findings in stress fractures of the lower limb: preliminary findings Eur. Radiol. 15 356–9

Brooks A J, Price V, Simms M, Ward N and Hand C J 2004 Handheld ultrasound diagnosis of extremity fractures J. R. Army Med. Corps 150 78-80

Chaar-Alvarez F M, Warkentine F, Cross K, Herr S and Paul R I 2011 Bedside Ultrasound Diagnosis of Nonangulated Distal Forearm Fractures in the Pediatric Emergency Department Pediatr. Emerg. Care 27(11) 1027-32

Chakraborty A, Bamber J C and Dorward N L 2012 Slip elastography: A novel method for visualizing and characterizing adherence between two surfaces in contact Ultrasonics 52(3) 364-76

Chan W 2009 Emergency bedside ultrasound for the diagnosis of rib fractures Am. J. Emerg. Med. 27 617–20

Chandrasekhar R, Ophir J, Krouskop T and Ophir K 2006 Elastographic image quality vs. tissue motion *in vivo* Ultras. Med. Biol. 32(6) 847-55

Chaudhry, A 2012 Effect of Boundary Conditions on Performance of Poroelastographic Imaging Techniques in Non Homogenous Poroelastic Media (College Station, Tex.: Texas A&M University) online resource.

Cheng J C Y and Shen W Y 1993 Limb Fracture Pattern in Different Pediatric Age Groups: A Study of 3,350 Children J. Orthop. Trauma 7(1) 15-22

Cheng S L, Tylavsky F and Carbone L 1997 Utility of ultrasound to assess risk of fracture J. Am. Geriatr. Soc. 45 1382–94

Cho M H, Kim K S, Ahn H H, Kim M S, Kim S H, Khang G, Lee B and Lee H B 2008 Chitosan gel as an in situ-forming scaffold for rat bone marrow mesenchymal stem cells *in vivo* Tissue Eng. Part A. 14(6) 1099-108

Cho K H, Lee Y H, Lee S M, Shahid M U, Suh K J and Choi J H 2004 Sonography of bone and bone-related diseases of the extremities J. Clin. Ultrasound 32 511–21

Cho K H, Lee S M, Lee Y H and Suh K J 2010 Ultrasound diagnosis of either an occult or missed fracture of an extremity in pediatric-aged children Korean J. Radiol. 11(1) 84-94

Christensen C 1998 Ultrasonic Bioinstrumentation (New York: Wiley)

Cochlin D L, Ganatra R H and Griffiths D F R 2002 Elastography in the Detection of Prostatic Cancer Clin. Radiol. 57(11) 1014-20

Cruess, R Land Dumont, J 1985 Healing of Bone, Textbook of Small Animal Orthopaedics ed C D Newton and D M Nunamaker : Lippincott Williams & Wilkins

DeLee D and Miller S 2002 Orthopaedic Sports Medicine Principles and Practice (Philadelphia, PA: Elsevier)

DeLee J C, Drez Jr. D, Miller M D 2009 Orthopaedic Sports Medicine: Principles and Practice (Philadelphia, PA: WB Saunders Co.)

Diaz J F J, Rey G A, Matas R B, De La Rosa F J B, Padilla E L and Vicente J V C 2008 New technologies applied to ultrasound diagnosis of sports injuries Adv. Ther. 25 1315–30

Dijkman B G, Sprague S, Schemitsch E H and Bhandari M 2010 When is a fracture healed? Radiographic and clinical criteria J. Orth. Trauma 24(Suppl 1) S76-80

Drakonaki E E, Allen G M and Wilson D J 2012 Ultrasound elastography for musculoskeletal applications British Journal of Radiology 85(1019) 1435-45

Duda G N, Taylor W R, Winkler T, Matziolis G, Heller M O, Haas N P, Perka C and Schaser K D 2008 Biomechanical, microvascular, and cellular factors promote muscle and bone regeneration Exerc. Sport Sci. Rev. 36(2) 64-70

Durston W and Swartzentruber R 2000 Ultrasound guided reduction of pediatric forearm fractures in the ER Am. J. Emerg. Med. 18 72–7

Enns P, Pavlidis T, Stahl J P, Horas U and Schnettler R 2004 Sonographic detection of an isolated cuboid bone fracture not visualized on plain radiographs J. Clin. Ultrasound 32 154–57

Feldkamp L A, Goldstein S A, Parfitt A M, Jesion G and Kleerekoper M 1989 The direct examination of three dimensional bone architecture *in vitro* by computed tomography J. Bone Miner. Res. 4 3–11

Fenster A and Downey D B 2000 Three-dimensional ultrasound imaging Ann. Rev. Biomed. Eng. 2 457–75

Friedrich-Rust M, Ong M, Herrmann E, Dries V, Samaras P, Zeuzem S and Sarrazin C 2007 Real-Time Elastography for Noninvasive Assessment of Liver Fibrosis in Chronic Viral Hepatitis American Journal of Roentgenology 188(3) 758-64

Garra B S, Cespedes E I, Ophir J, Spratt S R, Zuurbier R A, Magnant C M and Pennanen M F 1997 Elastography of breast lesions: initial clinical results Radiology 202(1) 79-86

Gee A, Prager R, Treece G and Berman L 2003 Engineering a freehand 3D ultrasound system Pattern Recognit. Lett. 24 757–77

Genant H K, Engelke K and Prevrhal S 2008 Advanced CT bone imaging in osteoporosis Rheumatology (Oxford) 47 iv 9–16

Gluer C C 1997 Quantitative ultrasound techniques for the assessment of osteoporosis: Expert agreement on current status. J. Bone Min. Research 12(8) 1280-8

Gonzalez R C and Woods R E 2008 Digital Image Processing 3rd edn (Upper Saddle River, NJ: Prentice-Hall)

Greenfield G B 2008 Radiology of Bone Diseases (Philadelphia, PA: R. Health Professions)

Hacihaliloglu I, Abugharbieh R, Hodgson A and Rohling R 2008 Bone segmentation and fracture detection in ultrasound using 3D local phase features Medical Image Computing and Computer-Assisted Intervention: MICCAI Int. Conf. on Medical Image Computing and Computer-Assisted Intervention 11 287–95

Hacihaliloglu I, Abugharbieh R, Hodgson A J and Rohling R 2009 Bone Surface localization in ultrasound using image phase-based features. Ultras. Med. Biol. 35(9) 1475-87

Hakulinen M A, Day J S, Toyras J, Timonen M, Kroger H, Weinans H, Kiviranta I and Jurvelin J S 2005 Prediction of density and mechanical properties of human trabecular bone *in vitro* by using ultrasound transmission and backscattering measurements at 0.2–6.7 MHz frequency range Phys. Med. Biol. 50 1629–42

Han S M and Kim S H 2005 A comparison of ultrasonic and x-ray methods for imaging the growth plate Proc. Inst. Mech. Eng. H 219 285–92

Hans D and Krieg M A 2008 The clinical use of quantitative ultra-sound (QUS) in the detection and management of osteoporosis IEEE Trans. Ultrason. Ferroelectr. Freq. Control 55 1529–38

Hickman C P Jr, Keen S L, Roberts L S, Larson A L, Eisenhour D J and I'anson H 2005 Integrated Principles of Zoology (New York: McGraw-Hill)

Hirai T, Manders E K, Nagamoto K and Saggers G C 1996 Ultrasonic observation of facial bone fractures: Report of cases Journal of Oral and Maxillofacial Surgery 54 776-9

Hosalkar H S, Torbert J T, Goebel J and Khurana J S 2009 Skeletal Trauma and Common Orthopedic Problems, ed J S Khurana: Humana Press 159-77

Hübner U, Schlicht W, Outzen S, Barthel M and Halsband H 2000 Ultrasound in the diagnosis of fractures in children J. Bone Joint Surg. Br. 82 1170–3

Hughes C W, Williams R W, Bradley M and Irvine G H 2003 Ultrasound monitoring of distraction osteogenesis Br. J. Oral Maxillofac. Surg. 41 256–58

Insana M F, Pellot-Barakat C, Sridhar M and Lindfors K K 2004 Viscoelastic imaging of breast tumor microenvironment with ultrasound J. Mammary Gland Biol. Neoplasia 9 393–404

Kallel F, Prihoda C D and Ophir J 2001 Contrast-transfer efficiency for continuously varying tissuemoduli: simulation and phantom validation Ultras. Med. Biol. 27 1115–25

Kalpakcioglu B B, Morshed S, Engelke K and Genant, H K 2008 Advanced imaging of bone macrostructure and microstructure in bone fragility and fracture repair. J. Bone Joint Surg. – Am. 90A (Suppl 1) 68-78

Karjalainen J P, Toyras J, Riekkinen O, Hakulinen M and Jurveli J S 2009 Ultrasound backscatter imaging provides frequency-dependent information on structure, composition and mechanical properties of human trabecular bone Ultras. Med. Biol. 35(8) 1376-84

Kaufman J J, Luo G and Siffert R S 2007 A portable real-time ultrasonic bone densitometer Ultras. Med. Biol. 33 1445–52

Kim J K, Baek J H, Lee J H, Kim J L, Ha E J, Kim T Y, Kim W B and Shong Y K 2012 Ultrasound Elastography for Thyroid Nodules: A Reliable Study? Ultras. Med. Biol. 38(9) 1508-13

Kirkpatrick A W, Brown R, Diebel L N, Nicolaou S, Marshburn T and Dulchavsky S A 2003 Rapid diagnosis of an ulnar fracture with portable hand-held ultrasound Mil. Med. 168 312–3

Konofagou E, D'Hooge J and Ophir J 2002 Myocardial elastography - A feasibility study *in vivo* Ultras. Med. Biol. 28(4) 475-82

Konofagou E E, Harrigan T and Ophir J 2000 Shear strain estimation and lesion mobility assessment in elastography Ultrasonics 38(1–8) 400-4

Konofagou E E, Ophir J, Kallel F and Varghese T 1997 Elastographic Dynamic Range Expansion Using Variable Applied Strains Ultrasonic Imaging 19(2) 145-66

Konofagou E and Ophir J 1998 A new elastographic method for estimation and imaging of lateral displacements, lateral strains, corrected axial strains and poisson's ratios in tissues Ultras. Med. Biol. 24(8) 1183-99

Kramer M, Gerwing M, Hach V and Schimke E 1997 Sonography of the musculoskeletal system in dogs and cats Vet. Radiol. Ultrasound 38 139–49

Krishnamurthy G T, Tubis M, Hiss J and Blahd WH 1977 Distribution pattern of metastatic bone disease – A need for total body skeletal image. J. Am. Med. Ass. 237(23) 2504-6

Lang T, Augat P, Majumdar S, Ouyang X and Genant H K 1998 Noninvasive assessment of bone density and structure using computed tomography and magnetic resonance Bone 22 149S–53S

Lasaygues P and Lefebvre J P 2001 Cancellous and cortical bone imaging by reflected tomography Ultrason. Imaging 23 55-70

Lasaygues P, Ouedraogo E, Lefebvre J P, Gindre M, Talmant M and Laugier P 2005 Progress towards *in vitro* quantitative imaging fo human femur using compound quantitative ultrasonic tomography Phys. Med. Biol. 50 2633-49

Laugier P 2004 An overview of bone sonometry Int. Congr. Ser. 1274 23–32

Laugier P, Droin P, LavalJeantet A M and Berger G 1997 *In vitro* assessment of the relationship between acoustic properties and bone mass density of the calcaneus by comparison of ultrasound parametric imaging and quantitative computed tomography Bone 20 157–65

Laugier P and Haïat G 2010 Bone Quantitative Ultrasound, Quantitative Ultrasound Instrumentation for Bone *in vivo* Characterization : Springer 47

Lewis D and Logan P 2006 Sonographic diagnosis of toddler's fracture in the emergency department J. Clin. Ultrasound 34 190–4

Longo R, Grimal Q, Laugier P, Vanlanduit S and Guillaume P 2010 Simultaneous determination of acoustic velocity and density of a cortical bone slab: ultrasonic model-based approach IEEE Trans. Ultrason. Ferroelectr. Freq. Control 57 496–500

Lovisetti G and Bettella L 2008 A One-wire Method for Anatomic Reduction of Tibial Fractures with Ilizarov Frame Clin. Orthop. 466(12) 2940-6

Liu D and Ebbini E S 2008 Viscoelastic property measurement in thin tissue constructs using ultrasound IEEE Trans Ultrason. Ferroelectr. Freq. Control 55 368–83

Madsen E L, Frank G R, Hobson M A, Shi H, Jiang J, Varghese T and Hall T J 2005 Spherical lesion phantoms for testing the performance of elastography systems Phys. Med. Biol. 50 5983–95

Mariacher-Gehler S and Michel B A 1994 Sonography: a simple way to visualize rib fractures Am. J. Roentgenol. 163 1268

Marin F, Gonzalez-Macias J, Diez-Perez A, Palma S and Delgado-Rodriguez M 2006 Relationship between bone quantitative ultrasound and fractures: a meta-analysis J. Bone Miner. Res. 21 1126–35

McNeil C, McManus J and Mehta S 2009 The accuracy of portable ultrasonography to diagnose fractures in an austere environment Prehosp. Emerg. Care 13 50–2

Mock C and Cherian M 2008 The Global Burden of Musculoskeletal Injuries: Challenges and Solutions: Springer New York 2306-16

Morikawa H, Fukuda K, Kobayashi S, Fujii H, Iwai S, Enomoto M, Tamori A, Sakaguchi H and Kawada N 2011 Real-time tissue elastography as a tool for the noninvasive assessment of liver stiffness in patients with chronic hepatitis C Journal of Gastroenterology 46(3) 350-8

Mukai-Higashihori K, Baba Y, Tetsumura A, Tsuji M, Ishizaki T, Higashihori N, Ohbayashi N, Kurabayashi T, Suzuki S and Ohyama K 2008 Ultrasonographic assessment of new bone formation in maxillary distraction osteogenesis J. Oral Maxillofac. Surg. 66 1750–3

Muller M, Moilanen P, Bossy E, Nicholson P, Kilappa V, Timonen J, Talmant M, Cheng S and Laugier P 2005 Comparison of three ultrasonic axial transmission methods for bone assessment Ultras. Med. Biol. 31 633–42

Nelson T R and Elvins T T 1993 Visualization of 3D ultrasound data Comput. Graph. Appl. 13 50–7

Njeh C F, Boivin C M and Langton C M 1997 The role of ultrasound in the assessment of osteoporosis: a review Osteoporos. Int. 7 7–22

Nyland T G and Mattoon J S 2002 Small Animal Diagnostic Ultrasound (Philadelphia, PA: Saunders)

Oomens C W J, Bressers O F J T, Bosboom E M H, Bouten C V C and Bade, D L 2003 Can Loaded Interface Characteristics Influence Strain Distributions in Muscle Adjacent to Bony Prominences? Comput. Methods Biomech. Biomed. Engin. 6(3) 171-80

Ophir J, Alam S K, Garra B, Kallel F, Konofagou E, Krouskop T and Varghese T 1999 Elastography: Ultrasonic estimation and imaging of the elastic properties of tissues Proceedings of the Institution of Mechanical Engineers, Part H: Journal of Engineering in Medicine 213(3) 203-33

Pallwein L, Mitterberger M, Struve P, Pinggera G, Horninger W, Bartsch G, Aigner F, Lorenz A, Pedross F and Frauscher F 2007 Real-time elastography for detecting prostate cancer: preliminary experience BJU Int. 100(1) 42-6

Parmar B J, Longsine W, Sabonghy E P, Han A, Tasciotti E, Weiner B K, Ferrari M and Righetti R 2010 Characterization of controlled bone defects using 2D and 3D ultrasound imaging techniques Phys. Med. Biol. 55(16) 4839-60

Parmar B J, Righetti R, Tasciotti E and Ferrari M 2009 The Feasibility of using Ultrasound Elastography Techniques to Improve Visualization of Bone Structure Proceedings of the Eighth International Conference on the Ultrasonic Measurement and Imaging of Tissue Elasticity 49

Parmar B J, Tasciotti E, Ferrari M and Righetti R 2009 New ultrasound imaging techniques to visualize bone fractures Ann. Meeting Natl. Center for Human Performance (Houston, TX, 6 November 2009)

Perren S M and Boitzy A 1978 Cellular differentiation and bone biomechanics during the consolidation of a fracture Anat. Clin. 1(1) 13-28

Prins S H, Jorgensen H L, Jorgensen L V and Hassager C 1998 The role of quantitative ultrasound in the assessment of bone: a review. Clinical Physiology 18(1) 3-17

Protopappas V C, Vavva M G, Fotiadis D I and Malizos K N 2008 Ultrasonic monitoring of bone fracture healing. IEEE Trans. Ultrason. Ferroelectr. Freq. Control 55(6) 1243-55

Qiu Y, Sridhar M, Tsou J K, Lindfors K K and Insana M F 2008 Ultrasonic Viscoelasticity Imaging of Nonpalpable Breast Tumors: Preliminary Results Acad. Radiol. 15(12) 1526-33

Rathfelder F J and Paar O 1995 Ultrasound as an alternative diagnostic measure for fractures during the growth phase Unfallchirurg 98 645–49

Redberg R 2009 Cancer risks and radiation exposure from CT JAMA Internal Medicine 169 2049-50

Redberg R F and Smith-Bindman R 2014 We are giving ourselves cancer. The New York Times website. http://www.nytimes.com/2014/01/31/opinion/we-are-giving-ourselves-cancer.html Accessed January 30, 2014

Richards P J, George J, Metelko M and Brown M 2010 Spine CT doses and cancer induction Spine 35 430-3

Righetti R, Ophir J and Krouskop T A 2005 A method for generating permeability elastograms and Poisson's ratio time-constant elastograms Ultras. Med. Biol. 31 803–16

Righetti R, Srinivasan S, Thitaikumar A, Ophir J and Krouskop T A 2007 Assessing image quality in effective Poisson's ratio elastography and poroelastography: I Phys. Med. Biol. 52(5) 1303

Rohrbach D, Preininger B, Hesse B, Gerigk H, Perka C and Raum K 2013 The Early Phases of Bone Healing Can Be Differentiated in a Rat Osteotomy Model by Focused Transverse-Transmission Ultrasound Ultras. Med. Biol. 39(9) 1642-53

Ross E, MacGillivray T, Muir A and Simpson A 2009 Imaging of the musculoskeletal system using 3D ultrasound J. Bone Joint Surg. Br. 91-B 451–2

Roux C, Fournier B, Laugier P, Chappard C, Kolta S, Dougados M and Berger G 1996 Broadband ultrasound attenuation imaging: a new imaging method in osteoporosis J. Bone Miner. Res. 11 1112–8

Rus G and Garcia-Martinez J 2007 Ultrasonic tissue characterization for monitoring nanostructured TiO2-induced bone growth Phys. Med. Biol. 52 3531–47

Sakas G 2002 Trends in medical imaging: from 2D to 3D Comput. Graph. 26 577–87

Sehgal C M, Lewallen D G, Nicholson J A, Robb R A and Greenleaf J F 1988 Ultrasound transmission and reflection computerized tomography for imaging bones and adjoining soft tissues. Proc. IEEE Ultrason. Symp. 2 849-8

Sambasubramanian S 2011 Comparison of the Performance of Different Time Delay Estimation Techniques for Ultrasound Elastography (College Station, Tex.: Texas A&M University) online resource.

Schatzker J and Tile M 2005 The Rationale of Operative Fracture Care : Springer

Schindeler A, McDonald M M, Bokko P and Little D G 2008 Bone remodeling during fracture repair: The cellular picture Semin. Cell Dev. Biol. 19(5) 459-66

Smith-Blindman R, Lipson J, Marcus R, et al. 2009 Radiation dose associated with common CT examinations and the associated lifetime attributable risk of cancer. JAMA Internal Medicine 169 2078-86

Sodickson A, Baeyens P F, Andriole K P, Prevedello L M, Nawfel R D, Hanson R and Khorasani R 2009 Recurrent CT, cumulative radiation exposure, and associated radiation-induced cancer risks from CT of adults Radiology 251(1) 175-84

Spatz H -, O'Leary E J and Vincent J F V 1996 Young's Moduli and Shear Moduli in Cortical Bone Proceedings of the Royal Society of London. Series B: Biological Sciences 263(1368) 287-94

Thitaikumar A, Krouskop T A, Garra B S and Ophir J 2007 Visualization of bonding at an inclusion boundary using axial-shear strain elastography: a feasibility study Phys. Med. Biol. 52(9) 2615

Thitaikumar A, Krouskop T A and Ophir J 2007 Signal-to-noise ratio, contrast-to-noise ratio and their trade-offs with resolution in axial-shear strain elastography Phys. Med. Biol. 52(1) 13

Thitaikumar A and Ophir J 2007 Effect of Lesion Boundary Conditions on Axial Strain Elastograms: A Parametric Study Ultras. Med. Biol. 33 9 1463-7

Thittai A K, Galaz B and Ophir J 2011 Visualization of HIFU-Induced Lesion Boundaries by Axial-Shear Strain Elastography: A Feasibility Study Ultras. Med. Biol. 37 3 426-33

Thittai A K, Yamal J, Mobbs L M, Kraemer-Chant C M, Chekuri S, Garra B S and Ophir J 2011 Axial-Shear Strain Elastography for Breast Lesion Classification: Further Results From *In vivo* Data Ultras. Med. Biol. 37(2) 189-97

Thomas A et al 2006 Real-time elastography? An advanced method of ultrasound: first results in 108 patients with breast lesions Ultrasound in Obstetrics and Gynecology 28(3) 335-40

Turan S, Turan O M, Ty-Torredes K, Harman C R and Baschat A A 2009 Standardization of the first-trimester fetal cardiac examination using spatiotemporal image correlation with tomographic ultrasound and color Doppler imaging Ultrasound Obstet. Gynecol. 33 652–6

Varghese T and Ophir J 1997 A theoretical framework for performance characterization of elastography: The strain filter IEEE Trans. Ultrason. Ferroelectr. Freq. Control 44(1) 164-72

Varghese T and Ophir J 1998 An analysis of elastographic contrast-to-noise ratio Ultras. Med. Biol. 24(6) 915-24

von Berg J, Kruecker J, Schulz H, Meetz K and Sabczynski J 2004 A hybrid method for registration of interventional CT and ultrasound images Int. Congr. Ser. 1268 492–7

Wakefield R J, Gibbon W W, Conaghan P G, et al. 2000 The value of sonography in the detection of bone erosions in patients with rheumatoid arthritis - A comparison with conventional radiography. Arthritis and Rheumatism 43(12) 2762-70

Wardak M M and Wardak E 2010 Percutaneous Gigli saw osteotomy Oper Orthop Traumatol 22(4) 414-20

Wang C L, Shieh J Y, Wang T G and Hsieh F J 1999 Sonographic detection of occult fractures in the foot and ankle J. Clin. Ultrasound 27 421–5

Wang L V 2008 Prospects of photoacoustic tomography Med. Phys. 35 5758–67

Williamson D, Watura R and Cobby M 2000 Ultrasound imaging of forearm fractures in children: a viable alternative? J. Accid. Emerg. Med. 17 22-4

Xu H, Rao M, Varghese T, Sommer A, Baker S, Hall T J, Sisney G A and Burnside E S 2010 Axial-Shear Strain Imaging for Differentiating Benign and Malignant Breast Masses Ultras. Med. Biol. 36(11) 1813-24

Yang X, Deka S and Righetti R 2011 A hybrid CPU-GPGPU approach for real-time elastography Ultrasonics, Ferroelectrics and Frequency Control, IEEE Transactions on 58(12) 2631-45

Ying L, Hou Y, Zheng H, Lin X, Xie Z and Hu Y 2012 Real-time elastography for the differentiation of benign and malignant superficial lymph nodes: A meta-analysis Eur. J. Radiol. 81(10) 2576-84

Young J W, Kostrubiak I S, Resnik C S and Paley D 1990 Sonographic evaluation of bone production at the distraction site in Ilizarov limb-lengthening procedures Am. J. Roentgenol. 154(1) 125–8

Zhai L, Palmeri M L, Bouchard R R, Nightingale R W and Nightingale K R 2008 An integrated indenter-ARFI imaging system for tissue stiffness quantification Ultrason. Imaging 30 95–111